Refining simulated mineral dust composition through modified size distributions: dual validation with mineral-specific and elemental observations

Sofía Gómez Maqueo Anaya[1], Sudharaj Aryasree[2], Konrad Kandler[2], Eduardo José dos Santos Souza[1], Khanneh Wadinga Fomba[1], Dietrich Althausen[1], Maria Kezoudi[3], Matthias Faust[1], Bernd Heinold[1], Ina Tegen[1], Moritz Haarig[1], Holger Baars[1], and Kerstin Schepanski[1,4]

[1]Leibniz Institute for Tropospheric Research (TROPOS), Leipzig, Germany
[2]Institute of Applied Geosciences, Technical University of Darmstadt, Germany
[3]Climate and Atmosphere Research Centre (CARE-C), The Cyprus Institute, Nicosia, Cyprus
[4]Free University of Berlin, Berlin, Germany

Correspondence: Sofía Gómez Maqueo Anaya (maqueo@tropos.de)

Abstract. ~~The JATAC2022 campaign~~ Two 2022 measurement campaigns in Cape Verde provided a unique opportunity to collect mineral dust aerosols from multiple Saharan source regions and characterize their composition. Mineral dust aerosols comprise a complex assemblage of minerals with distinct physico-chemical properties, leading to differentiated climatic impacts through interactions with radiation, cloud microphysics, and atmospheric chemistry. A crucial physical property governing these interactions is the particle size distribution (PSD), which strongly influences aerosol optical properties, transport, and deposition. Although contemporary atmospheric models have begun integrating mineralogical data into their dust aerosol representations, implementation faces complications due to variations in dust emission parameterizations, making some models more compatible with existing soil mineralogical databases than others.

This work addresses the challenges encountered when incorporating mineralogical information into the COSMO5.05-MUSCAT atmospheric model, which employs a dust emission scheme based on Marticorena and Bergametti (1995). We present an improved approach that refines the translation of mineralogical soil PSDs into emitted aerosol PSDs. The revised implementation is evaluated using historical Saharan dust measurements and new mineralogical observations from the JATAC2022 and DUSTRISK2022 campaigns. Model performance is assessed using a dual validation framework considering both mineral-resolved and elemental composition. The elemental validation approach provides complementary constraints that expose discrepancies in internal mixing assumptions and reveal limitations invisible to mineral-only comparisons. Results indicate that the proposed modification substantially improves representation of phyllosilicates ~~,~~ (illite, kaolinite, and smectite), quartz, and feldspar, while biases in iron, calcium, and magnesium highlight fundamental challenges in representing the heterogeneous internal structure of natural dust particles.

1 Introduction

Mineral dust aerosol is the most abundant atmospheric aerosol type by mass (Kinne et al., 2006) and exerts widespread influence on the Earth system. By scattering and absorbing solar and terrestrial radiation, dust modifies atmospheric heating rates, alters cloud microphysical processes, and perturbs the surface energy balance (Stocker et al., 2013; Kok et al., 2023). Despite this recognized role, large uncertainties remain in quantifying the net radiative forcing by dust. These uncertainties arise from the complex variability of dust properties during emission and transport, including particle size distribution (PSD), morphology, mixing state, and mineralogical composition (Huneeus et al., 2011; Mahowald et al., 2014; Di Biagio et al., 2020).

Mineralogical composition has emerged as a key factor in constraining dust–climate interactions. Different minerals govern how dust interacts with radiation, clouds, and other atmospheric constituents. For instance, small variations in the abundance of iron ~~oxide bearing~~ oxide-bearing minerals can strongly amplify shortwave absorption and alter dust's radiative properties (Balkanski et al., 2007; Gómez Maqueo Anaya et al., 2025; Li et al., 2024; Miffre et al., 2023; Obiso et al., 2024; Sokolik and Toon, 1999; Zhang et al., 2024), while silicate minerals differ in their potential to act as ice-nucleating particles (INPs) or cloud condensation nuclei (CCN) under varying conditions (Chatziparaschos et al., 2023; Harrison et al., 2019; Kelly et al., 2007; Murray et al., 2012). Yet, most chemistry transport models treat dust as homogeneous with respect to its composition, neglecting the strong spatial and temporal variability of mineral fractions. This simplification introduces biases in estimates of dust absorption, cloud interactions, and downstream impacts such as nutrient deposition (Kok et al., 2023).

Incorporating mineralogical detail into models is therefore essential, but it depends critically on how the PSD of individual minerals in soils is represented. The PSD controls not only transport and deposition but also the mineral dust particles' interaction with radiation. A central challenge is that the PSD of airborne dust does not directly reflect the PSD of the parent soil: during emission, processes such as soil texture effects, interparticle cohesion, wind friction velocity, and fragmentation and saltation dynamics reshape the particle size distribution (Marticorena and Bergametti, 1995; Kok, 2011). These nonlinear processes lead to size-dependent shifts in mineralogical composition, making the link between soil and atmospheric mineralogy far from trivial.

The particle size distribution of mineral dust fundamentally governs its atmospheric residence time and transport dynamics. Coarse-grained minerals such as quartz, feldspars, and calcite tend to be removed quickly by gravitational settling, resulting in higher concentrations near source regions. In contrast, finer clay-sized phyllosilicates, defined herein as the group of illite, kaolinite, and smectite, remain suspended for longer periods and thus constitute a major fraction of the dust transported to remote areas (Lawrence and Neff, 2009). ~~The~~

Despite the importance of these size-dependent dynamics, the Soil Mineral Atlases (SMAs), a generic term for databases describing the mineralogical composition of soils that are currently employed in atmospheric models, ~~however, classify minerals~~ rely on a simplified classification of soil mineralogy into only two size fractions, clay (defined as particles with diameters up to 2.5 µm) and silt (particles with diameters between 2.5 to 50 µm) ~~, which introduces~~ (diameter size ranges follow the convention used by Nickovic et al. (2012)). This framework introduces structural uncertainties and subsequent biases in model simulations. ~~As a result, models tend to overestimate~~ A notable consequence of this resolution limit is the representation of quartz; by assuming a constant mineral proportion across broad size ranges, models fail to capture the size-dependent

distributions observed in empirical studies (Kandler et al., 2007, 2009; Panta et al., 2023). This often results in a systematic overestimation of quartz mass fractions in coarser ~~size bins and underestimate them~~ bins and a corresponding underestimation in finer fractions ~~. This discrepancy stems from the assumption of a constant quartz proportion across a wide size range, which does not reflect its reported measured distribution (Kandler et al., 2007, 2009, 2018; Panta et al., 2023).~~ (Perlwitz et al., 2015a, b).

To ~~address this, some models apply~~ mitigate these discrepancies, several models have moved toward mineral-specific PSD transformations based on the ~~brittle fragmentation theory~~ Brittle Fragmentation Theory (BFT) (Kok, 2011)~~, which offers~~ . This approach provides a semi-direct framework for predicting size-resolved emission fluxes ~~of mineral dust particles (e.g., Gonçalves Ageitos et al., 2023; Scanza et al., 2015; Perlwitz et al., 2015a, b)~~(e.g., Gonçalves Ageitos et al., 2023; Scanza et al., 201 . However, ~~many models still rely on emission parameterizations from the~~ a significant number of models continue to rely on the parameterization scheme developed by Marticorena and Bergametti (1995)~~, which is based on~~ . While robust for bulk soil properties~~and~~ , this scheme cannot directly provide mineral-specific fluxes, particularly ~~given~~ when constrained by the incomplete mineralogical information ~~in the SMAscommonly used for atmospheric modeling~~inherent in standard SMAs. Assessing the implications of these contrasting ~~approaches is critical for~~ emission strategies is essential for accurate mineral-resolved simulations, yet systematic evaluations of their impact remain limited.

In a previous study, Gómez Maqueo Anaya et al. (2024) implemented a mineralogical composition module ~~in~~ for Saharan dust simulations within COSMO5.05–MUSCAT (COnsortium for Small-scale MOdelling v5.05 - MUltiScale Chemistry Aerosol Transport). Building on that work, this article addresses a central methodological question: how should the transformation of the ~~particle size distribution (PSD)~~ PSD from soil to atmosphere be represented within the COSMO5.05–MUSCAT dust emission framework to ensure a realistic reproduction of mineralogy-based dust properties? To this end, we evaluate two PSD transformation approaches based on the Marticorena and Bergametti (1995) emission scheme, coupled with the mineralogical database ~~,~~ GMINER (Nickovic et al., 2012). ~~Model results are systematically compared with in-situ measurements of airborne Saharan dust mineralogical composition under different atmospheric transport conditions.~~

Specifically, we contrast two modeling schemes, hereafter referred to as the ‘original’ and ‘modified’ approaches. The ‘original’ scheme, following Gómez Maqueo Anaya et al. (2024), maps the mineral soil PSD directly onto the aerosol size distribution. While this method adequately represents clay-sized minerals, it shows marked discrepancies for silt-sized fractions when compared with observations. To improve this representation, the ‘modified’ scheme introduces refinements to the treatment of mineral soil PSD via a redistribution of mineral fractions informed by ~~applications~~ the application of the BFT~~, as~~ . The details of this modification, along with the specific model configurations and experimental runs, are described in Section ~~2.3~~2.

The performance of the two schemes is assessed against a multi-level observational dataset. We first utilized a compilation of regional North African ~~measurements and~~ mineralogical measurements of in-situ aerosol samples to evaluate broad mineralogical patterns and enable a direct comparison between the implemented schemes. This is followed by a high-resolution comparison with concurrent in-situ observations ~~at Cabo Verdefrom the DUSTRISK (January–February 2022) and~~ from two campaigns in Cabo Verde: the Joint Aeolus Tropical Atlantic Campaign (JATAC, June 2022) ~~. DUSTRISK~~ and DUSTRISK (January–February 2022). JATAC 2022 provides size-resolved ~~elemental composition, while JATAC offers mineral- and elemental-specific measurements . The observational datasets used for these evaluations are summarized in Section ??.~~

~~Through these multi-level comparisons, we evaluate both schemes at the mineral and elemental scales, quantify the impact of the proposed modifications, and explore how seasonal variability (Section ??) in dust source regions influences airborne mineral composition. Results are presented in Section 5.1.1 for the regional compilation, Section 5.2.2 for~~ measurements of both mineralogical composition and elemental mass concentrations. Similarly, DUSTRISK 2022 ~~campaign, and Section 5.1.1 for~~ offers size-resolved elemental mass concentrations, allowing for a consistent evaluation of the model's chemical tracers. The specific measurement methodologies, instrumentation for size-segregation, and associated uncertainties for these campaigns are detailed in Section 3.

The strategy for model evaluation, including the metrics used for validation and the procedure for comparing grid-cell results to point measurements, is outlined in Section 4. Following this, the validation results are presented through a tiered approach categorized by analytical scale. Section 5.1 focuses on mineralogical comparisons, beginning with the regional North African compilation and followed by a detailed assessment of the JATAC 2022 results. Section 5.2 then provides a focused analysis of elemental composition, evaluating the model against the 2022 campaigns, JATAC and DUSTRISK 2022. This tiered approach allows us to assess whether the BFT-informed redistribution effectively bridges the gap between soil mineralogy and airborne dust composition across different transport conditions and measurement methodologies.

2 ~~Meteorological drivers of dust seasonality~~

~~Seasonal variations in meteorological conditions not only control the vertical and horizontal transport of mineral dust but also influence its mineralogical composition by modulating source activation and emission pathways (Kumar et al., 2018). The shifting wind regimes, surface moisture conditions, and boundary-layer dynamics determine which soil types are mobilized and how mineral fractions are mixed during transport. These processes, in turn, shape the composition of dust sampled at different locations and altitudes. A key contrast in North African dust transport is the altitude of plumes: during the Northern Hemispheric (NH) winter, dust remains largely confined to the lower troposphere, whereas in summer it is frequently lofted into mid-tropospheric layers. These seasonal variations are primarily driven by large-scale shifts in atmospheric circulation patterns over the Sahel and western Sahara (Kalu, 1979; Schepanski et al., 2009).~~

~~In NH summer, the northward migration of the Hadley cell shifts the Intertropical Discontinuity (ITD) into the northern Sahel and southern Sahara. The ITD marks the boundary between hot, dry desert air and moist monsoonal inflow from the south. Strong solar heating over the Sahara deepens the planetary boundary layer (PBL), enhancing vertical mixing and dust uplift (Schepanski et al., 2009). At night, an elevated dust layer develops above the monsoonal flow, where geostrophic winds, driven by the pressure gradient between the Saharan Heat Low and the subtropical Atlantic, entrain dust and lift it into the free troposphere (Parker et al., 2005). These elevated plumes are transported westward within the African Easterly Jet and modulated by African Easterly Waves, enabling long-range transport across the Atlantic. Summer dust layers commonly reach altitudes of 5–7 km, facilitating efficient export toward the Caribbean and the Americas (Chiapello et al., 1997; Engelstaedter et al., 2006 ; Harr et al., 2024).~~

~~In contrast, NH winter is characterized by weaker solar heating, a shallower PBL, and a southward retreat of the ITD. Dust sources shift deeper into the southern Sahel, and transport occurs predominantly at lower altitudes (1.5–3 km), carried westward by northeasterly trade winds (Barkan et al., 2004; Chiapello et al., 1997; Kalu, 1979; Harr et al., 2024). This shallow transport regime reduces the vertical extent of plumes, limiting their detectability in satellite retrievals and reducing the likelihood of transatlantic export. This season also coincides with the Sahelian biomass-burning period, during which substantial amounts of anthropogenic aerosols are emitted and frequently mix with the dust layer which complicates remote sensing retrievals of pure dust particles (?Heinold et al., 2011; Tesche et al., 2011). Overall, seasonal circulation patterns not only control the altitude and transport pathways of dust but also shape the composition and representativeness of samples collected at receptor sites, such as the Cape Verde archipelago.~~

2 ~~Methodology~~

1.1 ~~Model description and parametrizations~~

2 Model description and parametrizations

2.1 COSMO5.05-MUSCAT

The chemistry transport model used in this study is the MUltiScale Chemistry Aerosol Transport (MUSCAT) coupled online with the COnsortium for Small-scale MOdelling (COSMO) v5.05 model. COSMO, developed by the German Weather Service (Deutscher Wetterdienst, DWD), is a non-hydrostatic regional weather prediction model that solves the fundamental equations of atmospheric dynamics on a terrain-following grid (Baldauf et al., 2011). MUSCAT is the online-coupled chemistry transport component, computing the atmospheric transport of aerosols through time-dependent mass balance equations driven by COSMO meteorological fields (Heinold et al., 2011; Wolke et al., 2012). In this work, mineral dust aerosols are represented as passive tracers, i.e., they are not subject to chemical aging or chemically reactive transformations.

The coupled atmosphere-aerosol model system, COSMO-MUSCAT, has been widely applied and evaluated for Saharan dust studies. Previous validation efforts have demonstrated its capability to reproduce dust source activation, transatlantic transport, and regional dust transport under different meteorological conditions (Heinold et al., 2011; Schepanski et al., 2009; Tegen et al., 2013; Schepanski et al., 2016, 2017). The specific configuration used here has been further evaluated against atmospheric dust loading observations in Gómez Maqueo Anaya et al. (2024) and Gómez Maqueo Anaya et al. (2025).

The atmospheric life cycle of dust aerosols in MUSCAT is represented through a set of physical parameterizations dynamically coupled to COSMO meteorology and updated at every advection step. The main processes include: (1) dust emission, parameterized following Tegen et al. (2002) with modifications to incorporate mineralogical soil fractions as described in Gómez Maqueo Anaya et al. (2024); (2) aerosol transport, solved using a third-order upwind advection scheme with time-splitting integration (Wolke and Knoth, 2000); and (3) aerosol deposition, accounting for both dry and wet removal processes. Dry deposition is parameterized following the formulations of Seinfeld and Pandis (2016) and Zhang et al. (2001), while wet

deposition (including in-cloud scavenging or rainout, and below-cloud scavenging or washout) follows the approaches of Berge (1997) and Jakobsen et al. (1997), with detailed implementation described in Heinold et al. (2011).

2.1.1 ~~Dust emission scheme~~

2.2 Dust emission scheme

Dust emission is a non-linear process initiated when near-surface wind velocity generate sufficient vertical shear stress at the soil surface to initiate particle mobilization. In COSMO-MUSCAT, threshold friction velocities are calculated following the parameterization of Marticorena and Bergametti (1995), which accounts for size-resolved soil particle mobilization and depends on soil texture, surface roughness, vegetation, and soil moisture.

Emission fluxes are then computed interactively using the scheme of Tegen et al. (2002), first implemented in COSMO-MUSCAT by Heinold et al. (2007). Fluxes scale with the cube of the wind friction velocity, derived from COSMO-simulated near-surface winds, and are further modulated by vegetation cover and soil moisture. Particle uplift occurs when the effective friction velocity exceeds the size-dependent threshold (U_t^*), which is controlled by the erodible particle diameter (D_p), the aerodynamic roughness length of the total surface (Z_0), and the smoother, erodible fraction roughness length (z_{0s}).

~~The effective friction velocity is obtained from a drag partitioning approach that reduces the wind's erosive potential by accounting~~ To account for the sheltering effect of roughness elements~~. The size-dependent threshold friction velocity is expressed as:~~

~~$$U_t^*(D_p, Z_0, z_{0s}) = \frac{U_{ts}^*(D_p)}{f_{eff}(Z_0, z_{0s})},$$~~

~~where U_{ts}^* represents the part of~~ , a drag partitioning approach is utilized. This method defines an effective friction velocity (U_t^*~~that is available to the erodible soil, called the smooth surface~~), representing the total friction velocity required to mobilize size-dependent particles on a rough surface. It is related to the smooth-surface threshold friction velocity ~~, and~~ (U_{ts}^*), which is the threshold required for mobilizing the same particles under idealized, flat, conditions, via:

$$U_t^*(D_p, Z_0, z_{0s}) = \frac{U_{ts}^*(D_p)}{f_{eff}(Z_0, z_{0s})}, \tag{1}$$

where f_{eff} is the effective drag partition factor (ranging from 0 to 1). This factor accounts for the reduction in wind erosive potential due to surface roughness and it is calculated following Marticorena and Bergametti (1995) as:

$$f_{eff}(Z_0, z_{0s}) = 1 - \left[\ln\left(\frac{Z_0}{z_{0s}}\right) / \ln\left(0.35\left(\frac{10}{z_{0s}}\right)^{0.8}\right)\right]. \tag{2}$$

For bare desert surfaces, the aerodynamic roughness length (Z_0) is prescribed as 0.001 cm, following the recommendation of Darmenova et al. (2009), while z_{0s} is obtained from global satellite-derived dataset (Prigent et al., 2005). The ~~smooth-surface threshold friction velocity (~~value of U_{ts}^* is calculated as a function of particle diameter (D_p), particle density, and air density (ρ_a), representing a balance between aerodynamic and gravitational forces.

The actual surface friction velocity exerted by the atmosphere (U^*) is estimated from COSMO's 10-meter wind speed ~~output, providing an approximation of the near-surface wind forcing relevant for dust emission~~components (u_{10}, v_{10}) and air density. These are combined to determine an effective wind speed at height Z, denoted as $U(Z)$. Assuming adiabatic conditions and a logarithmic wind profile within the boundary layer, U^* is calculated as:

$$U^* = \frac{U(Z)\kappa}{\ln\left(\frac{Z}{Z_0}\right)} \tag{3}$$

where $\kappa = 0.4$ is the Von Karman's constant, and Z represents the height of the first model layer.

Dust emission ~~occurs when the~~ is triggered when this surface friction velocity exceeds the size-dependent threshold ~~necessary to mobilize soil particles, provided that soil conditions (e. g., moisture, roughness) are favorable. Once this condition is met~~friction velocity ($U^* \geq U_t^*$). This process is further modulated by local soil conditions such as moisture, which is accounted by an additional coefficient in the threshold calculation, following Fécan et al. (1999).

Once the threshold is surpassed, the emitted flux is represented as the horizontal particle flux (G), which scales with the cube of the friction velocity and accounts for the soil particle size distribution:

$$G = \frac{\rho_a}{g} \cdot U^{*3} \cdot \sum_i \left[\left(1 + \frac{U_t^*(D_{pi}, Z_0, z_{0s})}{U^*}\right)\left(1 - \frac{U_t^{*2}(D_{pi}, Z_0, z_{0s})}{U^{*2}}\right) \cdot B_{rel\text{-}i}\right] \text{for } U^* \geq U_t^*, \tag{4}$$

where ~~ρ_a is air density,~~ g is gravitational acceleration, ~~U^* is the surface friction velocity, U_t^* is the threshold friction velocity for each particle diameter (D_{pi}),~~ and $B_{rel\text{-}i}$ represents the relative basal surface area of size fraction i. In MUSCAT, the soil is represented by 196 discrete size fractions~~($i = 196$)~~.

Because the threshold friction velocity does not scale linearly with particle diameter, an accurate representation of the soil size distribution is required. In the Marticorena and Bergametti (1995) parametrization, the soil particle mass size distribution (PSD) is modeled using a multi-modal log-normal distribution:

$$\frac{dm(D_{pi})}{d\ln(D_{pi})}\frac{dm(D_p)}{d\ln(D_p)} = \sum_{j=1}^{n} \frac{m_j}{\sqrt{2\pi}\ln(\sigma_j)} \exp\left(\frac{(\ln D_{pi} - \ln MMD_j)^2}{-2\ln^2\sigma}\frac{(\ln D_p - \ln MMD_j)^2}{-2\ln^2\sigma}\right). \tag{5}$$

where j denotes the size mode (clay, silt, sand in the present MUSCAT setup) m_j is the mass fraction of mode j, σ is the geometric standard deviation (set to 2.0 independent of the mode), and MMD_j are the mass median diameters, set to 2.0 µm (clay), 15.0 µm (silt), and 150.0 µm (sand), respectively.

To determine the basal (projected) surface area distribution, the PSD is transformed assuming spherical particles of uniform density:

$$dB_t(D_{pi}) = \frac{dm(D_{pi})}{\frac{2}{3}\rho D_{pi}}. \tag{6}$$

The total basal surface area (B_t) is obtained by integrating Eq. (6) across all particle sizes. Normalizing $dB_t(D_{pi})$ by B_t yields the relative basal surface area distribution $B_{rel\text{-}i}$, which is used in Eq. (4) to allocate the horizontal flux across particle sizes.

Table 1. Definition of MUSCAT five independent size classes for mineral dust aerosol transport. Their size limits are indicated.

Bin name	Diameter range
BIN 01	0.2 - 1 µm
BIN 03	1 - 3 µm
BIN 09	3 - 9 µm
BIN 26	9 - 26 µm
BIN 80	26 - 80 µm

Saltation and particle bombardment processes (Marticorena and Bergametti, 1995) are incorporated by iteratively adjusting $B_{\text{rel-i}}$ for each size class, accounting for the momentum transfer from saltating particles to finer dust grains. Following this adjustment, the total horizontal flux is computed.

The fraction of the horizontal flux that becomes airborne is parameterized as a vertical dust flux (F):

$$F = \omega \cdot A_{\text{eff}} \cdot G \cdot (1 - A_{\text{snow}}) \cdot I_\theta, \tag{7}$$

where ω is the sandblasting efficiency, prescribed per soil type based on the local clay, silt, and sand fractions (Tegen et al., 2002). A_{eff} denotes the erodible surface area, ~~modulated by vegetation cover and aerodynamic roughness, while~~ A_{snow} ~~accounts for the fraction of this area that is~~ is the snow-covered ~~. The factor~~ fraction, and I_θ represents a soil moisture correction following Fécan et al. (1999). The vertical flux is then partitioned into five transport-relevant size bins (Table 1) to generate size-resolved dust fluxes for atmospheric injection.

The ~~vertical flux is then partitioned into five transport-relevant size bins (Table 1) to generate size-resolved dust fluxes for atmospheric injection. The~~ overall magnitude and spatial variability of emissions are ~~further influenced by~~ determined by the interplay of these surface conditions. ~~Soil moisture reduces emissions linearly above a critical threshold (Fécan et al., 1999) , while vegetation cover suppresses fluxes beyond a biome-dependent threshold (~~The influence of vegetation cover on A_{eff} is threshold-dependent. In desert regions, dust emission is inhibited once fractional vegetation cover exceeds 0.5~~fractional cover in desert regions) and scales them linearly below it (Tegen et al., 2002). Snow~~ ; below this threshold, the erodible area is scaled linearly to account for the partial sheltering of the surface (Tegen et al., 2002). Similarly, I_θ reduces emissions linearly once soil moisture exceeds a critical threshold determined. While snow cover also inhibits dust emissions~~; however~~, its parametrization is deactivated in this model configuration ~~, as its~~ given its negligible influence over the Sahara Desert~~is considered negligible~~. Together with the particle size distribution and surface roughness, these factors control the efficiency and spatial heterogeneity of dust emissions in ~~COSMO-MUSCAT~~the model.

2.2.1 ~~Input files and simulation setup~~

~~The mineralogical composition simulations in this study were performed using the COSMO5.05-MUSCAT modelwith a consistent configuration. The only variations among the simulation experiments lie in the time periods considered, some~~

(DUSTRISK) focus on January–February 2022, while for the JATAC 2022 comparisons simulations from June–July 2022 are used. For each of these periods, simulations were performed using two different mineralogical composition approaches, which differences are detailed in the following section.

The COSMO5.05-MUSCAT model domain is set up to cover the majority of the Sahara Desert and extend westward over the Atlantic Ocean to include the Cape Verde archipelago. The domain is bounded by 30.75°W to 39.32°E and 38.49°N to 0.38°S. Simulations are conducted at a horizontal resolution of 0.25° (approximately 28 km), with a vertical discretization of 40 layers. The lowest, surface level, model layer has a thickness of 20 m.

Meteorological initial and boundary conditions for COSMO5.05-MUSCAT are provided by the DWD in the form of 3-hourly meteorological fields. To maintain realistic atmospheric conditions, the model is re-initialized every 48 hours using overlapping cycles. Each 48-hour cycle begins with a 24-hour spin-up phase, during which only the COSMO5.05 meteorological model is active. Following this spin-up, MUSCAT is coupled to COSMO5.05 for the remaining 24 hours to simulate aerosol transport and interactions. Only the output from these second-day simulations, when both COSMO5.05 and MUSCAT are fully coupled, is used for analysis. Continuity between cycles is ensured by starting each new COSMO5.05 run 24 hours prior to the end of the previous MUSCAT simulation, while MUSCAT continues using its own prognostic fields from the preceding cycle as initial conditions.

The MUSCAT dust emission scheme is controlled by external soil-related datasets. Vegetation cover is prescribed using the FCOVER product from the Copernicus Global Land Service (Fuster et al., 2020), which provides fractional green vegetation coverage. Soil moisture input is taken from ERA5-Land hourly reanalysis data (Muñoz Sabater and Copernicus Climate Change Service, 20 , specifically the volumetric soil water content of the uppermost soil layer. Soil texture, expressed in terms of clay, silt, and sand fractions, is provided by the SoilGrids database (Poggio et al., 2021). In addition, the aerodynamic roughness length is prescribed using the dataset by Prigent et al. (2005). Together with the spatial constraints of the model domain, these datasets ensure that only continental dust sources are activated. To evaluate the spatial distribution of active sources, we further use the MSG-SEVIRI dust source activation frequency map by Schepanski et al. (2007).

Mineralogical composition is represented by the GMINER SMA (Nickovic et al., 2012), which was first implemented in the model system by Gómez Maqueo Anaya et al. (2024). The mineralogical fields in GMINER are based on the procedure introduced by Claquin et al. (1999), which identifies dust-productive soils according to the FAO74 classification. Effective mineral fractions are derived by combining soil texture classes, establishing links between soil types and key minerals including quartz, feldspar, calcite, gypsum, illite, kaolinite, smectite, and hematite. Phosphorus, present in several minerals and of particular importance for ocean fertilization, is also included. Mineral and phosphorus fractions are distributed between clay (<2 m) and silt (2–50 m) size populations. However, this approach introduces several sources of uncertainty. The relationship between soil type and mineral content is derived from sparse measurements and does not account for regional variability within a soil class. In addition, the underlying measurements are based on wet sedimentation techniques that alter the natural soil composition by breaking aggregates, thereby biasing the mineral allocation toward clay-sized fractions (Perlwitz et al., 2015a) . This artifact particularly affects the modeled content of phyllosilicates (illite, kaolinite, and smectite), which observations

~~suggest are more abundant in coarser size ranges (e.g., Kandler et al., 2009). Such uncertainties can lead to large deviations in modeled soil size distributions at emission (Journet et al., 2014; Perlwitz et al., 2015a).~~

~~The choice of GMINER as the implemented SMA is motivated by its ability to more accurately reproduce the iron oxide content in the study region (Gonçalves Ageitos et al., 2023). Since the primary objective of this implementation was to assess the impact of iron oxides on lidar-retrieved optical properties (Gómez Maqueo Anaya et al., 2025), GMINER provided a suitable basis for the analysis. At the same time, the comparative study by Gonçalves Ageitos et al. (2023) showed that GMINER also better captures phyllosilicate distributions, particularly kaolinite for North Africa, than the Journet et al. (2014) SMA. Feldspar exhibited greater spatial variability, with lower errors when using GMINER, although feldspar size distributions remain poorly characterized due to their absence from the finer fractions in this dataset. By contrast, calcite concentrations were more accurately represented by Journet et al. (2014), while GMINER systematically underestimated calcite levels over the Sahara Desert. At the time of implementation, these two SMAs were the only datasets available for use.~~

2.3 Mineralogical composition modification~~in COSMO5.05-MUSCAT~~

~~This section introduces the methodological framework developed to improve and evaluate the representation of mineralogical composition in atmospheric dust simulations. The focus is on modifications to the mineralogical representation in the COSMO5.05-MUSCA model (Gómez Maqueo Anaya et al., 2024), designed to enhance how mineral size distributions are treated within simulated aerosol composition.~~

In the 'original' approach by Gómez Maqueo Anaya et al. (2024), mineralogical fractions are prescribed by directly mapping the mineral soil particle size distribution (PSD) from GMINER (Nickovic et al., 2012) onto the mineral-resolved aerosol PSD ~~(see~~ as represented by the upper panel of Fig. 1~~)~~. A key limitation of this approach is that the modifications to the bulk PSD caused by the emission process do not affect the mineral-resolved PSD. This overlooks the fact that the emission process explicitly alters the overall dust PSD, as predicted by dust emission theories (Kok et al., 2012; Marticorena and Bergametti, 1995; Shao et al., 2011).

This inconsistency stems from the structure of GMINER in combination with Marticorena and Bergametti (1995)'s emission scheme, since GMINER provides mineralogical mass fractions only for the finest soil classes (silt and clay). These are assumed to represent the airborne dust range, given their capacity to remain suspended for several days. However, the emission scheme of Marticorena and Bergametti (1995) (Eqs. (~~4~~5)–(~~7~~6)) requires the full soil PSD to represent saltation and bombardment processes. Larger soil particles, although not staying airborne, are essential because their impacts release smaller fragments that otherwise could not overcome interparticle cohesion forces via wind induced friction velocity only (Marticorena and Bergametti, 1995; Iversen and White, 1982).

Consequently, a consistent application of the Marticorena and Bergametti (1995) scheme is not possible with GMINER alone, since the database lacks information on the coarser soil fractions. Figure 2 illustrates this limitation for a representative Saharan grid cell, highlighting the substantial portion of the soil PSD that is missing when mineral fractions are restricted to only the two finest classes.

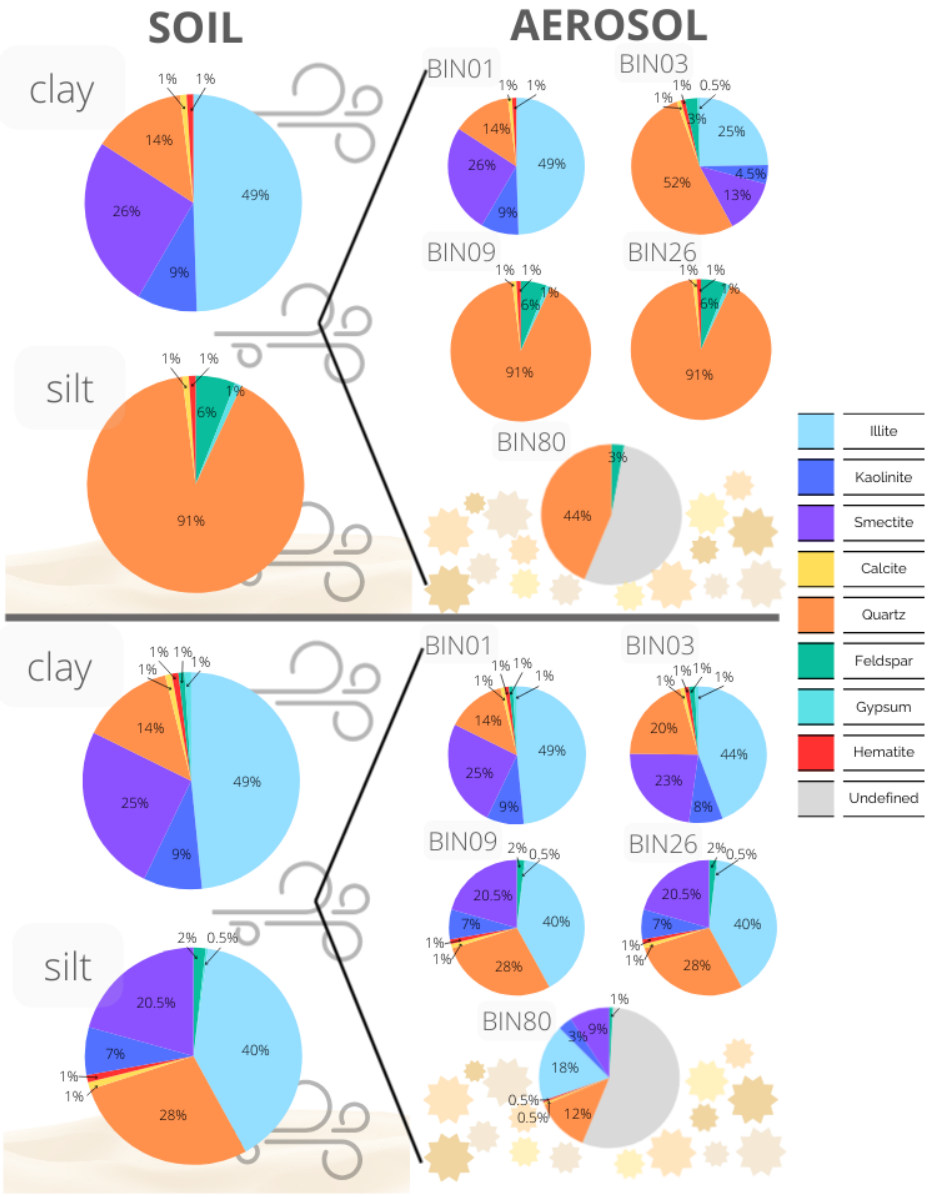

Figure 1. Mineralogical composition of soil and emitted dust particles. Larger pie charts represent the mineral fractions in the soil distribution, where clay is defined as particles with diameters below 2.5 µm and silt particles between 2.5 µm and 50 µm. Smaller pie charts represent the mineral fractions of aerosols per size bin as classified in MUSCAT (Table 1). Particles exceeding 50 µm diameter are not classified by mineral component and are labeled as "undefined". The upper panel shows the original mineral soil PSD as obtained by GMINER and the subsequent mineral fractions in the aerosol bins mimicking that distribution. The lower panel shows the modifications to the soil mineralogy distribution and resulting aerosol fractions following the parametrizations of Perlwitz et al. (2015a) and Gonçalves Ageitos et al. (2023).

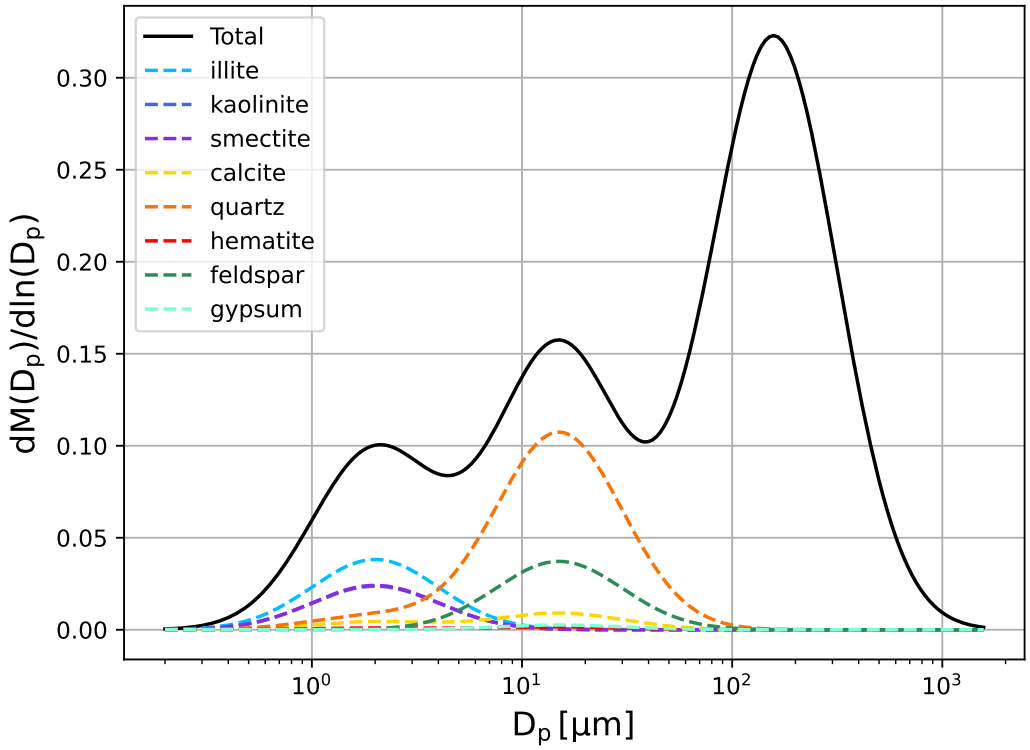

Figure 2. Mass size distribution of soil particles ~~in~~ at a ~~random~~ representative Saharan grid cell (22.45°N, 20.9°E)~~in the Saharan Desert~~. ~~In~~ The black ~~,~~ solid line represents the total ~~mass size~~ distribution ~~is shown~~obtained from the SoilGrids database (Poggio et al., 2021), exhibiting three distinct modes ~~can be observed for the different soil size classes~~ corresponding to clay, silt and sand fractions. ~~In dashed,~~ Dashed colored lines ~~,~~ indicate the mineral specific mass size distributions ~~per mineral~~ as ~~given in~~ described by the GMINER database~~are shown~~. Figure from Gómez Maqueo Anaya (2025)

The emission scheme inherently favors silt-sized particles, which require relatively low wind stress for entrainment and are small enough to remain airborne, as illustrated by the threshold friction velocity ~~curve~~ function (in Fig. 1 of Marticorena and Bergametti (1995)). This aerodynamic preference becomes problematic when GMINER assigns minerals exclusively to silt or clay size classes. Treating these mineral-resolved PSDs as representative of the full soil PSD within the Marticorena and Bergametti (1995) framework introduces systematic biases: clay-sized minerals experience artificially suppressed emissions due to high cohesion thresholds that rely on larger saltating particles to be broken, while silt-sized minerals are prone to overestimation in the absence of coarser, non-erodible grains. Accurate dust emission calculations therefore require a complete soil PSD, where larger particles mobilize finer fractions via saltation bombardment (Kok et al., 2012; Marticorena and Bergametti, 1995). This issue is compounded by the methodology used to construct GMINER: wet sieving mechanically disaggregates soil

samples, increasing the apparent fraction of clay-sized particles relative to undisturbed soils (Perlwitz et al., 2015a). While airborne clay-sized fractions generally match source soils and are preserved during transport (Caquineau et al., 1998; Lafon et al., 2004), silt-sized mineral distributions show poorer agreement, partly due to biases introduced by wet-sieving (Perlwitz et al., 2015a).

To address these issues, several modeling studies have incorporated mineral-specific transformations from soil to aerosol PSDs (e.g., Perlwitz et al., 2015a, b; Gonçalves Ageitos et al., 2023; Pérez García-Pando et al., 2016; Scanza et al., 2015; Li et al., 2021). These approaches build on the Brittle Fragmentation Theory (BFT) of Kok (2011), which posits that for the finest particles, the emitted size distribution is largely independent of soil properties and wind speed. BFT conceptualizes emission as a sequence of energetic collisions between saltating aggregates, producing fragments that predominantly fall below a characteristic size threshold. The resulting particle number concentration N is inversely proportional to the square of the particle diameter D_p, modulated by an exponential cutoff, as expressed in the following relation:

$$\frac{dN}{dlnD_\mathrm{p}} \propto \frac{1}{D_\mathrm{p}^2} exp\left[-\left(\frac{D_\mathrm{p}}{D_\mathrm{c}}\right)^3\right] \mathrm{for} D_\mathrm{p} > D_\mathrm{s}, \tag{8}$$

where D_s represents a scalar diameter within the "indivisible" size ~~, where particles~~ range. Particles at or below this scale are considered primary grains resistant to further fragmentation due to ~~their~~ inherent particle cohesion. ~~According to Kok (2011), this indivisible size corresponds to the wet-sieved PSD observed in soil samples, as wet sieving disperses soilaggregates until further breakdown becomes mechanically limited (Perlwitz et al., 2015a)~~Following Kok (2011), the probability of finding such indivisible grains at a specific size D_s is dictated by the PSD of the fully dispersed, wet-sieved soil. Incorporating this ~~concept~~distribution, the emitted number size distribution ~~can be~~ is formalized as:

$$\frac{dN}{dlnD_\mathrm{p}} = \frac{1}{c_\mathrm{N} D_\mathrm{p}^2} exp\left[-\left(\frac{D_\mathrm{p}}{D_\mathrm{c}}\right)^3\right] \int_0^{D_\mathrm{p}} p(D_\mathrm{s}) dD_\mathrm{s}, \tag{9}$$

where c_N is a normalization factor, and $p(D_\mathrm{s})$ represents the probability density function ~~of the indivisible soil particle diameters after wet sieving~~derived from the wet-sieved PSD. In this integral, D_s serves as the scalar integration variable representing the diameters of the constituent primary grains. This formulation captures the physical constraint that ~~emitted particles~~ an emitted aggregate of size D_p ~~cannot be formed from indivisible components larger than D_s~~can only be composed of indivisible components smaller than or equal to itself $D_\mathrm{s} \leq D_\mathrm{p}$. The integral term (the cumulative distribution function of the soil minerals) thus reduces the ~~number of small-sized emitted~~ emission of small particles if the soil ~~has a limited abundance of~~ lacks sufficient fine indivisible grains, while the exponential cutoff suppresses ~~emissions at larger~~ the emissions of very large diameters.

The BFT posits that the emitted number concentration of small dust particles is largely independent of the undispersed soil size distribution, with the ~~upper limit of aggregate diameters~~ characteristic aggregate diameter (D_c) estimated at 12 ± 1 µm (Kok, 2011). In this framework, the PSD of emitted aggregates is skewed toward larger diameters compared to wet-sieved soil, consistent with observations by Kandler et al. (2009) and Enete (2012), which indicate that saltation-driven fragmentation preserves a greater fraction of mass in the silt-size range than suggested by wet-sieved samples. Perlwitz et al. (2015a) further show that roughly 45% of the silt-sized emitted mass originates from aggregated indivisible particles that would be classified as

clay-sized in wet-sieved soils. To reconcile this discrepancy, they proposed an empirical correction that reallocates a fraction of clay-sized minerals from wet-sieved soils to the silt fraction, particularly phyllosilicates ~~such as~~ (illite, kaolinite, and smectite), which are categorized in GMINER exclusively in clay size classes but contribute to silt-sized emissions in reality.

This adjustment is quantified using Equation (9) to derive a generalized ratio of emitted clay- to silt-sized particles, assumed to be spatially invariant and independent of local soil conditions. This simplifying assumption has been adopted in several modeling studies (Albani et al., 2014; Perlwitz et al., 2015a, b; Scanza et al., 2015; Pérez García-Pando et al., 2016; Gonçalves Ageitos et al., 2023). However, it applies only to particles below 20 µm, as larger particles are more sensitive to site-specific emission factors such as wind speed, soil properties, and surface roughness. Since GMINER defines the silt class up to 50 µm, a further adjustment is needed for particles in the 20–50 µm range. Perlwitz et al. (2015a) addressed this by scaling the clay contribution using measurements from Kandler et al. (2009), which provided empirical data on the coarse-mode mineral distribution of freshly emitted dust. Using Equation (9), they estimated a clay-to-silt ratio of 0.05 for diameters below 20 µm~~, which was reduced to~~ . When integrated over the full 0-50 µm range and volume-normalized to account for the coarser fraction, this corresponds to approximately 1.3% of the total emitted mass ~~for the 0–50 µm range after volume-normalization for the coarser~~ being attributed to the clay mineral fraction.

This methodology rests on two critical assumptions. First, it assumes that the PSD measured at Tinfou by Kandler et al. (2009) is representative of other dust source regions. While this may not hold universally, the observed increase in silt fraction with particle diameter is consistent with the physical principle that the threshold friction velocity for emission decreases with particle size (Marticorena and Bergametti, 1995; Iversen and White, 1982). The approach also assumes that the emitted PSD is primarily determined by mineral-specific fragmentation, neglecting wind speed variations. This assumption is reasonable for particles below 20 µm, where Eq. (9) offers a reliable approximation, but becomes less reliable for coarser particles where emission dynamics are more sensitive to environmental conditions. Second, the model neglects modifications to the PSD caused by gravitational settling during transport to the Tinfou observation site. This simplification is justified by focusing only on measurements taken during high-concentration dust events, which are presumed to reflect recently emitted aerosols with minimal transport-induced size sorting.

~~Larger pie charts represents mineral fraction soil distribution, clay represents particles with diameters below 2.5 µm and silt represents particles above. Smaller pie charts represent the mineral fractions of aerosols per size bin as classified in MUSCAT (Table 1). Upper panel shows the original mineral soil particle size distribution as obtained by GMINER and the subsequent mineral fractions in the aerosol bins mimicking that distribution. Lower panel shows the modifications to that mineral soil particle size distribution by following the modifications suggested by Perlwitz et al. (2015a), and Gonçalves Ageitos et al. (2023)~~ .

This methodology is implemented here as the 'modified' approach, in which the dispersed soil size distribution from the GMINER SMA is adjusted to more realistically represent the aerosol size distribution observed in atmospheric dust. The formulation follows Perlwitz et al. (2015a), based on BFT. From GMINER, the mass fraction of each mineral ~~$k \in \mathcal{M}$ in the~~ k in the conceptual clay (0-2 µm) and silt (2-50 µm) size categories is denoted by $m_k^{\mathrm{c}}(s_{\mathrm{t}})$ and $m_k^{\mathrm{s}}(s_{\mathrm{t}})$, respectively~~, where s_{t} is the arid soil type provided by FAO74. These~~ . It should be noted that these two broad categories are used for

the mineralogical reallocation process and are distinct from the five discrete aerosol transport bins defined in Table 1. Thse fractions are normalized for each soil type s_t (arid soil type provided by FAO74) such that:

$$\sum_{k\in\mathcal{M}}^{8}{}_{k=1} m_k^c(s_t) = 1 \text{ and } \sum_{k\in\mathcal{M}}^{8}{}_{k=1} m_k^s(s_t) = 1, \tag{10}$$

with $|\mathcal{M}|$=8 minerals considered. To better reflect the emitted PSD, the BFT-based method distributes all minerals across both size categories, including those originally classified exclusively as clay- or silt-sized in GMINER.

To assign mineral fractions to the actual aerosol size categories, soil texture information from the SoilGrids database (Poggio et al., 2021) is incorporated. Let $m^c(s_x)$ and $m^s(s_x)$ denote the soil mass fractions of clay- and silt-sized particles, normalized such that:

$$m^c(s_x) + m^s(s_x) = 1. \tag{11}$$

The combined soil mineral mass fraction in each size category at each location is then computed by weighting the GMINER mineral fractions by the local soil texture proportions:

$$m_k^c(s_t, s_x) = m^c(s_x) m_k^c(s_t), \quad m_k^s(s_t, s_x) = m^s(s_x) m_k^s(s_t). \tag{12}$$

This ensures that the total soil mineral mass fraction across both reallocation size classes sums to unity:

$$\sum_{k\in\mathcal{M}}^{8}{}_{k=1} (m_k^c(s_t, s_x) + m_k^s(s_t, s_x)) = 1. \tag{13}$$

In this formulation, soil mineral mass fractions vary spatially according to two factors: the arid soil type (s_t), which governs mineralogical composition, and the soil texture class (s_x), which determines the relative abundance of clay- and silt-sized particles.

Once the soil mineral fractions are obtained from Eq. (12), the next step is to derive the emitted mass fraction of each mineral in the clay and silt size SMA categories. Denote by ϕ^c and ϕ^s the total emitted mass fractions of clay- and silt-sized aerosols, constrained by:

$$\phi^c + \phi^s = 1. \tag{14}$$

These totals are composed of contributions from all minerals $k \in \mathcal{M}k$. Let ϕ_k^c and ϕ_k^s represent the emitted clay- and silt-sized fractions attributable to mineral k. They satisfy:

$$\phi^c = \sum_{k\in\mathcal{M}}^{8}{}_{k=1} \phi_k^c \text{ and } \phi^s = \sum_{k\in\mathcal{M}}^{8}{}_{k=1} \phi_k^s, \tag{15}$$

and consequently:

$$\sum_{k\in\mathcal{M}}^{8}{}_{k=1} (\phi_k^c + \phi_k^s) = 1. \tag{16}$$

Thus, the emitted mineral mass fractions across all species and size classes sum to unity. Following the BFT-based formulation, the global clay-sized emission fraction is prescribed as ϕ^c=0.013, constant across all locations. The contribution of mineral k to

clay-size emissions is therefore~~given by~~:

$$\phi_k^{\mathrm{c}}(s_{\mathrm{t}}) = \phi^{\mathrm{c}} m_k^{\mathrm{c}}(s_{\mathrm{t}}), \quad \phi^{\mathrm{c}} = 0.013, \tag{17}$$

meaning that the proportion of emitted clay-sized dust mirrors the clay mineral fractions of the fully dispersed soil. In this context, the fully dispersed soil represents a theoretical, maximally dispersed state, a conceptual limit where all aggregates are broken down into their primary, indivisible constituents.

With ϕ^{c} prescribed, the total silt-sized fraction follows implicitly as:

$$\phi^{\mathrm{s}} = 1 - \phi^{\mathrm{c}} = 0.987. \tag{18}$$

For each mineral, the emitted silt-sized fraction $\phi_{\mathrm{k}}^{\mathrm{s}}$ has two sources: (1) particles originally present in the soil in the silt-size range, and (2) ~~fragments of clay-sized particles that are mobilized through the disaggregation of aggregates during saltation. The latter is approximated by~~ primary clay minerals that are emitted within larger silt-sized aggregates during the saltation-driven fragmentation of the parent soil. To account for this, the model performs an empirical reallocation ~~of clay mass into the silt fraction~~where a fraction of the soil's clay mineral mass is transferred into the silt-sized aerosol population. This is expressed as:

$$\phi_k^{\mathrm{s}} = \vartheta\left(\gamma_k m_k^{\mathrm{c}}(s_{\mathrm{t}}, s_{\mathrm{x}}) + m_k^{\mathrm{s}}(s_{\mathrm{t}}, s_{\mathrm{x}})\right). \tag{19}$$

where γ_{k} is a mineral-specific reaggregation coefficient quantifying the clay-to-silt transfer, and ϑ is a normalization constant ensuring that the sum of all $\phi_{\mathrm{k}}^{\mathrm{s}}$ equals ϕ^{s}.

For simplicity, γ_{k} is assumed constant across minerals, with the exception of feldspar, gypsum, and quartz. Feldspar is typically overrepresented in the silt fraction due to its fragmentation behavior, while gypsum is soluble and exhibits distinct disaggregation and spatial patterns (Perlwitz et al., 2015a). Quartz, which dominates the coarse end of the size spectrum and shows little evidence of disaggregation, is prescribed with γ_{quartz}=0. ~~Based on Eqs. (12) and (19), the emitted silt-sized fraction of mineral k is therefore expressed as:~~

$$\phi_k^{\mathrm{s}}(s_{\mathrm{t}}, s_{\mathrm{x}}) = \vartheta(s_{\mathrm{t}}, s_{\mathrm{x}}) \left[\gamma_k m^{\mathrm{c}}(s_{\mathrm{x}}) m_k^{\mathrm{c}}(s_{\mathrm{t}}) + m^{\mathrm{s}}(s_{\mathrm{x}}) m_k^{\mathrm{s}}(s_{\mathrm{t}})\right].$$

~~In this formulation, γ_{k} acts to suppress the silt-size emissions of minerals such as quartz, while extending the contribution of clay-rich species (e.g., phyllosilicates) into the silt range. This redistribution reflects the contrasting aggregation behaviors of different minerals: quartz remains largely intact during saltation, whereas clay-dominated aggregates disintegrate, contributing to larger size classes.~~

~~Feldspar~~ Notably, feldspar and gypsum require special treatment since they are present in both clay and silt fractions of atmospheric aerosols (e.g., Enete, 2012) but are absent from the clay fraction in the GMINER SMA. Consequently, Eq. (17) cannot be applied directly. Instead, their clay-size fractions are estimated following the approach of Gonçalves Ageitos et al. (2023), which uses proxy minerals and scaling ratios: for feldspar, the extension into the clay fraction is scaled according to the quartz clay-to-silt ratio:

$$m_{\mathrm{feldspar}}^{\mathrm{c}}(s_{\mathrm{t}}) = m_{\mathrm{feldspar}}^{\mathrm{s}}(s_{\mathrm{t}}) * \frac{m_{\mathrm{quartz}}^{\mathrm{c}}(s_{\mathrm{t}})}{m_{\mathrm{quartz}}^{\mathrm{s}}(s_{\mathrm{t}})}, \tag{20}$$

and for gypsum, the calcite clay-to-silt ratio is used:

$$m^{\mathrm{c}}_{\mathrm{gypsum}}(s_{\mathrm{t}}) = m^{\mathrm{s}}_{\mathrm{gypsum}}(s_{\mathrm{t}}) * \frac{m^{\mathrm{c}}_{\mathrm{calcite}}(s_{\mathrm{t}})}{m^{\mathrm{s}}_{\mathrm{calcite}}(s_{\mathrm{t}})}. \tag{21}$$

To conserve the total clay-size mass balance (Eq. 10), the phyllosilicate fractions in the clay category are proportionally reduced by soil type.

Once these database gaps are addressed, the emitted silt-sized fraction of mineral k is expressed based on Eqs. (12) and (19) as:

$$\phi^{\mathrm{s}}_k(s_{\mathrm{t}}, s_{\mathrm{x}}) = \vartheta(s_{\mathrm{t}}, s_{\mathrm{x}}) \left[\gamma_k m^{\mathrm{c}}(s_{\mathrm{x}}) m^{\mathrm{c}}_k(s_{\mathrm{t}}) + m^{\mathrm{s}}(s_{\mathrm{x}}) m^{\mathrm{s}}_k(s_{\mathrm{t}})\right]. \tag{22}$$

In this formulation, γ_{k} acts to suppress the silt-size emissions of minerals such as quartz, while extending the contribution of clay-rich species (e.g., phyllosilicates) into the silt range. This redistribution reflects the contrasting aggregation behaviors of different minerals: quartz remains largely intact during saltation, whereas clay-mineral constituents are emitted as part of larger silt-sized aggregates rather than as fully dispersed fine particles.

A schematic representation of the 'modified' approach is shown in the lower panel of Fig. 1. In this framework, a substantial reduction of the quartz fraction is introduced, along with a redistribution of minerals across size classes. Specifically, phyllosilicates are incorporated into the silt fraction, while feldspar and gypsum are extended into the clay fraction. The application of Eqs. (22)–(21) thereby entails a relative decrease of feldspar and gypsum within the silt-size range, resulting from the additional contribution of phyllosilicates.

After constructing the adjusted mineral soil PSD, which better represents the composition of mineral aerosols at larger sizes, it is incorporated into the COSMO5.05-MUSCAT emission scheme. The underlying emission algorithm remains unchanged from the implementation described by Gómez Maqueo Anaya et al. (2024): the vertical emission flux in each MUSCAT size bin is scaled by the corresponding soil mineral fraction, with each mineral assigned to its own bin within the respective size category (see Table 1). In the revised configuration, the mineralogical SMA is updated to reflect the modified PSD, and additional bins are introduced to represent minerals that now occur simultaneously in both clay and silt size ranges.

3 ~~In-situ dust sampling: dataset compilation and model comparison framework~~

2.1 ~~Compilation of North Africa mineralogical measurements~~

~~To assess the atmospheric relevance of the modeled modifications, we compared COSMO5.05-MUSCAT model outputs with in-situ mineralogical measurements, taking into account the pronounced seasonal variability that governs Saharan dust emissions and their transport pathways. Because these seasonal effects are closely linked to mesoscale weather patterns and source activation, only measurements representative of NH winter months were retained to match the DUSTRISK 2022 campaign period (January–February 2022) (Gómez Maqueo Anaya et al., 2024) for this compilation.~~

~~Schematic representation of the workflow used to select and compare in-situ mineral dust measurements with COSMO5.05-MUSCAT simulations. Primary datasets are displayed in yellow boxes with slanted corners and bold text. The analysis pathway for~~

simulated mineralogy is depicted by green lines and arrows, while the in-situ measurement selection process is indicated by gray lines and arrows. Decision points are represented by blue hexagons, procedural steps by blue octagons, supplementary datasets by yellow rectangular boxes, and final outcomes by lavender octagons.

The compilation builds on the dataset of Perlwitz et al. (2015b), augmented with additional North African measurements. The workflow for the selection of the measurements datasets is visualized in Figure 4. Long-term campaigns, here defined as sampling more than two dust events, were included only if their sampling period extended beyond NH summer months. The dataset was further expanded relative to the initial COSMO5.05-MUSCAT comparison with in-situ measurements (Fig. 5 in Gómez Maqueo Anaya et al. (2024)), and can be accessed through the zenodo repository . For long-term campaigns, we computed average mineral mass fractions over the DUSTRISK 2022 campaign simulation period and compared these against measurements. This approach was applied to the datasets of Adedokun et al. (1989); Enete (2012); Formenti et al. (2008); Kandler et al. (20 and Panta et al. (2023).

For shorter measurement campaigns covering up to two dust events, we employed a more detailed matching procedure (see the decision tree workflow from To verify the modified mineral approach, the scheme was compared against the MONARCH reference for Haplic Xerosols in the northwestern Sahara (Gonçalves Ageitos et al., 2023). Despite differences in bin resolution and emission parameterizations, both models demonstrate a consistent redistribution pattern, specifically, the "dust event analysis" box shifting of phyllosilicates toward silt-sized categories and a proportional reduction in quartz. The resulting mineralogical shift from soil to emitted aerosol for this soil type is illustrated in Fig. 4). This approach combined two complementary datasets: (i) HYSPLIT back trajectories (Stein et al., 2015) and (ii) dust emission records from the MSG-SEVIRI Dust RGB product (EUMETSAT). Following the methodology of Schepanski et al. (2007), recently applied in Souza et al. (2025) , we identified probable dust source regions by integrating these datasets. Simulated dust plumes were then selected to match the observed transport pathways. Backward trajectories for simulated dust events were computed using the LAGRANTO tool (Miltenberger et al., 2013) driven by COSMO5.05 meteorological fields. Comparison with measurements only proceeded when similar dust source regions were identified through these datasets, allowing direct matching of individual dust plume measurements with model outputs. B1.

Three campaigns required this detailed matching procedure: Alastuey et al. (2005), Jeong and Achterberg (2014), and Kandler et al. (200 . For the Alastuey et al. (2005) study, MSG-SEVIRI data were unavailable before 2004, so we used Meteosat-7 natural color imagery to identify a dust plume traveling from mid-southern Algeria to Tenerife on 29 July 2002. For the other two campaigns, observed plumes were individually matched to simulated events from corresponding source regions by combining HYSPLIT back trajectories (intersected with active MSG-SEVIRI dust emissions) with LAGRANTO back trajectories (intersected with the same emission areas). Several older measurements used by Perlwitz et al. (2015b), dating back to the 1970s, could not be reliably traced using this combined approach, and were therefore not compared with COSMO5.05-MUSCAT DUSTRISK outputs.

2.1 Input files and simulation setup

Although the selection criteria were appliedrigorously, some historical dust plumes may not have been accurately matched to those simulated by Mineralogical dust simulations were conducted using a consistent COSMO5.05-MUSCAT. Deviations from typical seasonal transport patterns cannot be ruled out, as meteorological anomalies could have produced unusually strong emissions from certain source regions during the measurement periods. Such events may not be captured in the model output, which represent only January–MUSCAT physical configuration. The experimental design varied across two primary dimensions: the simulation period and the mineralogical scheme. To match the observational campaigns, simulations were performed for January–February 2022, while the observations span a broader range of meteorological conditions. Furthermore, several measurement sites are located near major dust sources, where local emissions can dominate the observed mineral composition in ways that may not be fully resolved at the model's spatial resolution, as seen in the campaigns reported by Formenti et al. (2008); Kandler et al. (2009); Møberg et al. (1991) and Panta et al. (2023)2022 (DUSTRISK) and June–July 2022 (JATAC). For each of these periods, two distinct mineralogical composition approaches, the original and modified schemes, were applied. The simulation experiments are summarized in Table 2.

Additional uncertainty arises from inconsistencies in particle size classification across the measurement datasets. Some studies report only "bulk" mineral composition without specifying the particle size range; in these cases, the full The COSMO5.05-MUSCAT size range (0.2–80 μm) was used for comparison. Other measurements adopt 'clay' and 'silt' categories, which are generally better defined but vary in the clay–silt boundary, reported between <2 μm and 2.5 μm (i.e., Kandler et al., 2009; Møberg et al., 199 . For these, model bins were mapped accordingly, with clay represented by BIN01 + 0.5 BIN03 and silt by 0.5 BIN03 + BIN09 + BIN26 + BIN80. When specific diameter ranges were reported (i.e., Kandler et al., 2007, 2009; Panta et al., 2023), the model bins containing more than 50% of the stated range were selected, and the average mineral mass fractions of those bins were used for comparison. These classification inconsistencies underscore the need for high-resolution, well-characterized, and concurrent measurement datasets. Such datasets were obtained during both the DUSTRISK and JATAC 2022 campaigns.

2.2 DUSTRISK 2022 campaign elemental composition

The DUSTRISK 2022 campaign took place in the model domain is set up to cover the majority of the Sahara Desert and extend westward over the Atlantic Ocean to include the Cape Verde archipelagoduring January and February 2022. Particulate matter sampling was conducted at two sites (named inflow and outflow) on the Cape Verde island of Santiago, where the inflow site is positioned upwind of urban areas and exposed mainly to continental air masses from Africa, in contrast to the outflow site which is positioned outwind of the major urban area (Praia) (Bredeck et al., 2024; Souza et al., 2025). To ensure direct comparability with model simulations that represent only continental dust sources, the analysis presented here focuses exclusively on measurements from the inflow site. The inflow site in Santiago is located at 14°. The domain is bounded by 30.75°59'24" N, 23°W to 39.32°E and 38.49°N to 0.38°S as represented in Fig. 3. Simulations are conducted at a horizontal resolution of 0.25° (approximately 28'16" W , this site is characterized by strong prevailing northeast trade winds, with aerosol particles influenced by local marine emissions from the Atlantic Ocean and long-range transport of continental air masses from Africa, frequently carrying Saharan dust.

Table 2. ~~Mass percentage~~ Summary of ~~key elements found in the COSMO5.05-MUSCAT simulated minerals~~simulations used for measurement comparison. ~~The smectite group is represented by the end-member montmorillonite,~~ Domain and ~~feldspar is represented by~~ all input files remain consistent across model runs. For a ~~1:1 average~~ detailed description of ~~microcline (K-feldspar) and albite (Na-feldspar). This selection is based on common mineralogical assemblages observed in Saharan dust aerosols (Scheuvens et al., 2013; Formenti et al., 2011, 2014).~~the differences between mineralogy schemes, refer to Section 2.3

~~Mineral~~Simulation	~~Fe (%)~~ Time frame	~~Si~~
~~Hematite~~ DUST-CM-01	~~69.94~~ January-February 2022	~~-~~
~~Illite~~ DUST-CM-02	~~1.43~~ January-February 2022	~~25.~~
~~Kaolinite~~ JAT-CM-01	~~-~~ June-July 2022	~~21.~~
~~Smectite~~ JAT-CM-02	~~-~~ June-July 2022	~~20.~~

~~Quartz - 46.80 - - - - - Feldspar - 30.89 10.23 - 14.05 0.76 - Gypsum - - - - - 23.28 18.62 Calcite - - - - - 40.04 -~~

~~Particulate matter (PM) samples were collected during January and February 2022 using Digitel DHA-80 high-volume samplers (Walter Riemer Mess Technik, Germany) operating at an average flow rate of 500~~ Lkm), with a vertical discretization of 40 layers. The lowest, surface level, model layer has a thickness of 20 ~~min^{-1}. At each site, separate PM2.5 and PM10 samplers were deployed. Sampling typically occurred over 24-hour periods (noon to noon); however, during pronounced dust events, sampling duration was shortened to capture peak concentrations. All samples were collected on Ahlstrom micro-quartz fiber filters (MK 360) (Bredeck et al., 2024; Souza et al., 2025).~~ m.

~~Total reflection X-ray fluorescence (TXRF) spectroscopy was employed to determine elemental concentrations following the methodology previously described in detail (Fomba et al., 2020).Filter samples of 1.5 cm^2 area were prepared by digesting three 8 mm spots per filter in a HCl/HNO_3 mixture (0.375 mL and 1.125 mL, respectively)using a microwave digester (Mars 6, CEM, Germany). Internal standards (Sc/Co at 10 μL) were added to the digested solutions, which were then applied to siliconized quartz carriers, dried at 80°C, and analyzed using a Bruker S4 T-STAR instrument. This procedure determined concentrations of Al, Ti, Ca, K, Mg, S, Si, Cr, Mn, Fe, among other elements. Measurement precision was assessed by calculating relative errors from duplicate sample measurements.~~

~~Table ?? presents the mass percentages of selected elements within the simulated minerals. We focus on Fe, Si, Al, Mg, K, Ca, and S because these elements are commonly used for mineral identification in atmospheric dust studies (Kandler et al., 2018; Formenti et al. .~~

~~The comparison between simulated and measured elemental compositions follows a three-step procedure: (1) Filter samples from inflow sites are identified, and measured elemental masses are normalized by total mass concentration to obtain elemental mass fractions. (2) Simulated mineral mass concentrations are extracted from the corresponding grid cells, temporally averaged over the filter sampling periods (±30-minute tolerance),~~

Meteorological initial and boundary conditions for COSMO5.05-MUSCAT are provided by the DWD in the form of 3-hourly meteorological fields. To maintain realistic atmospheric conditions, the model is re-initialized every 48 hours using overlapping

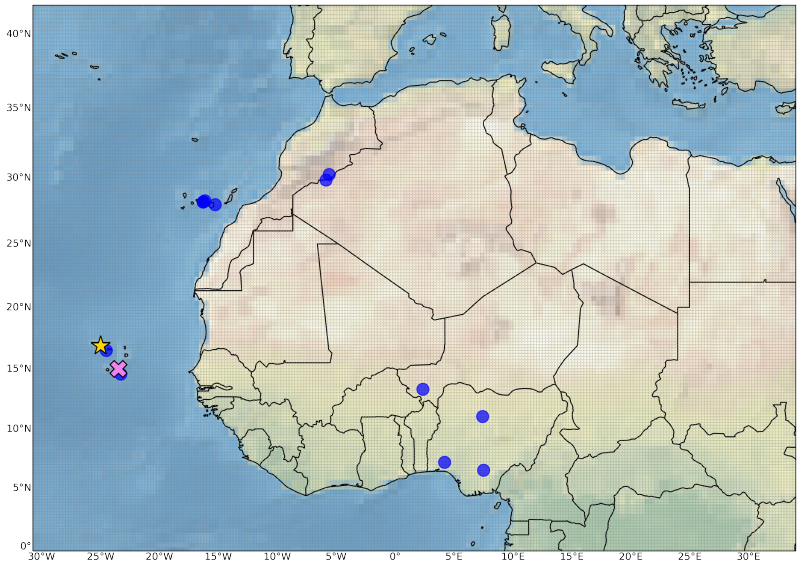

Figure 3. Simulation domain for COSMO5.05-MUSCAT, featuring a 0.25° resolution grid in gray dotted lines. The yellow star identifies São Vicente (Cabo Verde), the site of the JATAC 2022, while the violet X indicates Praia (Santiago, Cabo Verde), where the DUSTRISK 2022 measurements were conducted. Blue dots show the locations of a measurement compilation utilized for a broader model validation.

cycles. Each 48-hour cycle begins with a 24-hour spin-up phase, during which only the COSMO5.05 meteorological model is active. Following this spin-up, MUSCAT is coupled to COSMO5.05 for the remaining 24 hours to simulate aerosol transport and interactions. Only the output from these second-day simulations, when both COSMO5.05 and MUSCAT are fully coupled, is used for analysis. Continuity between cycles is ensured by starting each new COSMO5.05 run 24 hours prior to the end of the previous MUSCAT simulation, while MUSCAT continues using its own prognostic fields from the preceding cycle as initial conditions. The entire simulation period is preceded by a 15 day intial spin-up, and ~~aggregated by size fraction. For PM2.5, we use MUSCAT 's BIN01 + 0.5×BIN03; for PM10, we use BIN01 + BIN03 + BIN09 where available (e. g., the original scheme defines phyllosilicates only through BIN03). (3) Mineral mass concentrations are converted to elemental mass concentrations by multiplying by their respective elemental mass percentages (Table **??**), summing over minerals, and normalizing by total simulated mass concentration to yield elemental mass fractions~~results are outputted at 1 hour intervals.

~~In total reflection X-ray fluorescence (TXRF) analysis,~~ The MUSCAT dust emission scheme is controlled by external soil-related datasets. Vegetation cover is prescribed using the FCOVER product from the Copernicus Global Land Service (Fuster et al., 2020), which provides fractional green vegetation coverage. Soil moisture input is taken from ERA5-Land hourly reanalysis data (Muñoz Sabater and Copernicus Climate Change Service, 2019), specifically utilizing the volumetric soil water content of the ~~reproducibility of measurements on disk-shaped sample carriers is evaluated by performing multiple measurements on the same sample while rotating it. This approach helps account for any non-uniformity in the deposited residue. To assess measurement precision, each sample carrier was analyzed at 0° and 90° rotational positions, yielding replicate~~

~~intensity data. The measurements used for validation were quality screened to ensure that measurements corresponding in their majority to mineral dust aerosols. Only samples with dust concentrations $\geq$38 µg/m^3 were included in the comparison (dust concentrations are derived following Souza et al. (2025) procedure). This screening resulted in 33 PM2.5 filters and 47 PM10 filters for the final validation dataset.~~7 cm uppermost soil layer. Soil texture, expressed in terms of clay, silt, and sand fractions, is provided by the SoilGrids database (Poggio et al., 2021), while aerodynamic roughness lengths are provided through the dataset by Prigent et al. (2005).

2.2 ~~JATAC 2022 mineralogical composition~~

These datasets, combined with the model's spatial constraints, restrict dust activation exclusively to continental source regions. Furhtermore, the spatial distribution of active dust emission sources is constrained by the MSG-SEVIRI dust source activation frequency map by Schepanski et al. (2007). Finally, the mineralogical composition is represented by the GMINER SMA (Nickovic et al., 2012) implemented via the two distinct modeling approaches detailed in Sect. 2.3.

3 Cape Verde measurement campaigns: in-situ aerosol measurements

3.1 JATAC 2022

During the JATAC 2022 campaign, in-situ ~~measurements~~ recollection of mineral dust aerosols were performed using Unmanned Aerial Vehicles (UAVs) over São Vicente, Cape Verde, (indicated by the yellow star in Fig. 3) throughout June 2022. The ~~Cypurs~~ Cyprus Institute conducted 25 UAV flights, each equipped with Optical Particle Counters (OPCs) for fine- and coarse-mode height-resolved PSD observations. Dust particles were collected from the atmospheric layers using onboard impactor samples (Marinou et al., 2023), with a Giant Particle Collector (GPaC) capable of capturing particle diameters from nanometers up to tens of micrometers (Kezoudi et al., 2025, 2021). The GPaC's upper size limit depends on airspeed, pressure, and temperature; as a reference, during the SAMUM-2 campaign, particles up to 28.5 µm were successfully collected (Lieke et al., 2011).

Two OPCs were mounted on each UAV. The Universal Cloud and Aerosol Sounding System counted aerosols with diameters from 0.28 to 17.0 µm, while the Printed Optical Particle Spectrometer measured number concentrations in the 0.14–3 µm range (Kezoudi et al., 2021). OPC measurements were used to validate PSDs derived from collected dust samples, following the methodology of Panta et al. (2023).

Aerosol chemical composition and single-particle characteristics were analyzed using a scanning electron microscope coupled with Scanning Electron Microscope-Energy Dispersive X-ray spectrometry (SEM-EDX) to determine particle size, shape, and elemental composition. Back-scattered images were used to study particles with projected area diameters (PAD) >0.5 µm, where PAD ($D_\mathrm{p} = \sqrt{4A_\mathrm{p}/\pi}$, with A_p as the particle area) closely approximates aerodynamic diameter for dust (Aryasree et al., 2024; Kandler et al., 2018). SEM-EDX provides normalized atomic percentages for elements including: F, Na, Mg, Al, Si, P, S, Cl, K, Ca, Ti, V, Cr, Mn, Fe, Zn, and Pb. ~~Major dust components are classified primarily based on the Al/Si ratio, with additional constraints from variations in Ca, Fe, Mg, K, and Na within aluminosilicates~~

~~(Aryasree et al., 2024; Kandler et al., 2018, 2020; Panta et al., 2023).~~ This method allows detection of particles up to 30 µm, with measurement precision for major compounds within 2% relative standard deviation (RSD), while minor compounds range from 10–20% for particles >3 µm, and can exceed to 100% for the smallest particles. Diameter measurement uncertainty decreases with size, from ∼1.5% RSD at 2 µm to <1% for particle diameters >3 µm (Kandler et al., 2018).

~~Certain minerals have well-defined compositions, such as gypsum, quartz, and calcite, making them readily identifiable through elemental ratios. Others, notably clay minerals like illite and smectite, exhibit substantial compositional variability, complicating their identification (Panta et al., 2023; Kandler et al., 2007, 2018; Rieder et al., 1998). Additionally, dust particles frequently occur as internal mixtures or aggregates rather than pure mineral phases. Consequently, the approach adopted here identifies the dominant mineral type within each particle . For single-particle quantification, an elemental index for element X is defined as the atomic fraction of that element relative to the sum of all quantified elements (Aryasree et al., 2024; Kandler et al., 2007, 2018;~~

~~:~~

$$mineral-like = \frac{X}{(Na+Mg+Al+Si+P+S+Cl+K+Ca+Ti+Cr+Mn+Fe)}.$$

~~Here, the element symbols represent the relative atomic percentage measured in each particle. Classification uses predefined rules based on the elemental index and additional ratios, determined by the dominance of specific elements or their combinations (e. g., Al, Si, Ca, Fe, Al~~Impactor sampler collected 18 samples, and analyzed size, shape and elemental composition for 25000 single particles during the measurement period. Samples with a low number of particles (<500) were discarded to ensure reliable statistics while counting~~/Si). Particle classes are named after their most prevalent chemical component(s) , incorporating mineral phase terms where appropriate (e.g., gypsum, quartz), with labels assigned according to the best match to measured elemental concentrations.~~ grouping each particle group. This screening protocol resulted in a final validation dataset comprising 17 high-quality samples.

~~Particles are grouped into mineralogical classes using rule sets derived from elemental ratios, taking into account ideal mineral compositions as well as natural variability and measurement uncertainty. While not all minerals strictly conform to the atomic ratios in Eq. (??), the classification focuses on minerals most relevant to the simulated compositions~~In this study, one of the main objectives is to accurately represent the aerosol dust mineralogy in future modeling studies using measurement data. Hence, we adopt a classification scheme for mineral dust aerosols representative of the soil database as used in the model. Size-segregated (same as Table 1) chemical composition of major dust aerosols: illite, kaolinite, smectite, quartz, feldspar, calcite, gypsum and hematite were derived by defining ideal elemental compositions for the modeled minerals in the elemental space. The used composition in terms of mass compositions are shown in Table A. This classification scheme assigns the single particles to the closest ideal composition. Counting statistics for each particle group are used to estimate uncertainty by generating two-sided 95% confidence intervals under a binomial assumption. ~~Table ?? provides detailed definitions of the mineral classes used in this study, the corresponding element X, and the criteria for *mineral-like* classification.~~

~~Criteria for element-based identification of major minerals. Element symbols indicate atomic percent concentrations. When X corresponds to a single element or a sum of elements, it replaces X in Eq. (??). If X is not specified, the listed elemental ratio and its range are used directly to assign the mineral classification. **Class name** **Atomic range** **Value range** Quartz-like~~

~~*X*=Si 0.7 - 1.01 Al/Si 0 - 0.22 (Na+Mg+K+Ca+Al)/Si 0 - 0.2 F/(F+Si) 0 - 0.499 Kaolinite-like *X*=Al+Si 0.7 - 1.01 Al/Si 0.5 - 1.5 Fe/(Al+Si) 0 - 0.2 Mg/(Al+Si) 0 - 0.2 Ca/(Al+Si) 0 - 0.2 Na/(Al+Si) 0 - 0.15 K/(Si) 0 - 0.1 (Na+Cl+2*S)/(Al+Si) 0 - 0.25 Illite-like *X*=K+Al+Si 0.7 - 1.01 Al/Si 0.45 - 1.5Fe/(Al+Si) 0 - 0.2Mg/(Al+Si) 0 - 0.2 (Na+Ca)/(Al+Si) 0 - 0.2 K/(Si) 0.1 - 1.01(Na+Cl+2*S)/(Al+Si) 0 - 0.25Smectite-like *X*=Mg+Al+Si 0.7 - 1.01 Al/Si 0.5 - 1.5 Fe/(Al+Si) 0 - 0.2 Mg/(Al+Si) 0.2 - 1.01(Na+Ca)/(Al+Si) 0 - 0.2 K/Si 0 - 0.1 (Na+Cl+2*S)/(Al+Si) 0 - 0.25 **Class name** **Atomic range** **Value range** Calcite-like *X*=Ca 0.7 - 1.01 *X*=Ca+Mg 0.7 - 1.01 (Al+Si)/Ca 0 - 0.3 Mg/Ca 0.3 - 3.0 S/Ca 0 - 0.3 Cl/Ca 0 - 0.19 P/(Ca+P) 0 - 0.8 Gypsum-like *X*=(Ca+S) 0.7 - 1.01 Ca/(Ca+S) 0.2 - 0.8 Mg/Ca 0 - 0.3Cl/Ca 0 - 0.3 Iron oxides-like *X*=Fe 0.5 - 0.98999 *X*=(F+Si)/F 0 - 0.499 Cr/(Cr+Fe) 0 - 0.1 Cl/(Cl+Fe) 0 - 0.1 Ti/(Ti+Fe) 0 - 0.1 Feldspar-like *X*=K+Al+Si 0.7 - 1.01 *X*=Na+Al+Si 0.7 - 1.01 *X*=Ca+Al+Si 0.7 - 1.01 *X*=Na+Ca+Al+Si 0.7 - 1.01 Al/Si 0.22 - 0.45 (Na+K+Ca)/(Na+K+Ca+Al+Si) 0.15 - 0.25 Fe/(Fe+Al+Si) 0 - 0.15~~

For iron oxide minerals such as hematite, the ~~atomic~~ ratio reported in Table ~~??~~ A reflects the iron oxide content from a single-particle perspective. However, a significant fraction of iron in dust occurs within the crystal lattice of other minerals (Lafon et al., 2004; Zhang et al., 2015), necessitating an alternative approach to estimate total iron oxide content.

Following Aryasree et al. (2024), we use two parameters: (i) the total iron oxide percentage (Fe_{oxides}), which accounts for iron present either as pure oxy-hydroxides (e.g., hematite, goethite) or incorporated within mineral lattices, and (ii) the total Fe index, defined as the atomic ratio of Fe to the sum of all quantified elements~~, as in Eq. (??).~~. The total iron oxide percentage is calculated as:

$$Fe_{\text{oxides}} = \left(\frac{m_{\text{Feox\%}}}{m_{\text{Fe\%}}}\right) * \left(\frac{M_{\text{Fe}}}{M_{\text{dry}}}\right) * 100, \tag{23}$$

where $m_{\text{Feox\%}}$ and $m_{\text{Fe\%}}$ are the mass fractions of iron oxides and elemental iron relative to the total dust mass, respectively, obtained from Table 3 in Di Biagio et al. (2019) for different Saharan source regions. M_{Fe} is the estimated Fe mass within a single particle from SEM-EDX measurements, and M_{dry} is the particle's dry mass.

Using ~~Eq. (23),~~ this formulation, mass percentages for both total iron oxide and hematite ~~mass percentages are derivedfor each particle~~are derived. For hematite specifically, ~~the iron oxide mass fraction~~ hematite mass fraction from Di Biagio et al. (2019) is used to substitute $m_{\text{Feox\%}}$ in Eq. (23)~~is replaced by the hematite mass fraction reported in Table 3 of Di Biagio et al. (2019)~~ . The uncertainty arising from the representative ratio of iron oxide content from 19 desert dust types given by Table 3 in Di Biagio et al. (2019) which is generally less than 15%. For us, this is a systematic error, as we apply the same ratio to all samples.

Additionally, elemental mass concentrations are provided for the species most commonly associated with mineral dust, including Si, Al, Fe, Ca, K, Mg and S. Both mineralogical and elemental data are partitioned into the MUSCAT size bins up to BIN26.

~~The calculated mineral mass fractions are then compared against COSMO5.05-MUSCAT simulation outputs, where simulated mineral compositions are extracted from the corresponding grid cells and averaged over both the sampling periods and specified altitude ranges. In addition to the mineralogical composition comparison, elemental mass fractions are evaluated using the model validation methodology described in the previous section (Section 3.2)~~

3.2 DUSTRISK 2022 campaign

The DUSTRISK 2022 campaign took place in the Cape Verde archipelago during January and February 2022. Particulate matter was sampled at two distinct sites, referred to as inflow and outflow, on the island of Santiago (Cabo Verde). The inflow site (14°54'32" N, 23°30'54" W, indicated by the violet X in Fig. 3) was positioned in the city of Praia, on the northeastern coast, directly facing the ocean. ~~Filter measurements were quality screened to ensure sufficient particle counts for robust statistical analysis, where only filters containing 1000–2000 particles were included in the comparison. This~~

The sampling site was strategically positioned to intercept air masses dominated by the prevailing northeast trade winds, which transport Saharan mineral dust directly from the African continent. Located upwind of both the urban center of Praia and the island's interior, the site is well-situated to ensure that collected aerosols represent long-range continental transport with minimal interference from local island soils. Although minor anthropogenic contributions from nearby urban areas cannot be entirely discounted, the site's orientation ensures that local influences remain negligible, as corroborated by previous studies (Cardoso et al., 2018; Fomba et al., 2025). In contrast, the outflow site is positioned downwind of the major metropolitan area and is significantly more susceptible to local anthropogenic and local dust emissions (Bredeck et al., 2024; Souza et al., 2025) . To ensure direct comparability with model simulations that represent only continental dust sources, this analysis focuses exclusively on measurements from the inflow site.

Particulate matter (PM) samples were collected using Digitel DHA-80 high-volume samplers (Walter Riemer Mess Technik, Germany) operating at an average flow rate of 500 $\mathrm{L\,min^{-1}}$. At each site, separate PM2.5 and PM10 samplers were deployed. Sampling typically occurred over 24-hour periods (noon to noon); however, during pronounced dust events, sampling duration was shortened to capture peak concentrations. All samples were collected on Ahlstrom micro-quartz fiber filters (MK 360) (Bredeck et al., 2024; Souza et al., 2025).

Elemental concentrations were determined using Total reflection X-Ray Fluorescence (TXRF) spectroscopy, following the methodology described by Fomba et al. (2020). Filter samples of 1.5 $\mathrm{cm^2}$ area were prepared by digesting three 8 mm spots per filter in a $\mathrm{HCl/HNO_3}$ mixture (0.375 mL and 1.125 mL, respectively) using a microwave digester (Mars 6, CEM, Germany). Internal standards (Sc/Co at 10 μL) were added to the digested solutions, which were then applied to siliconized quartz carriers, dried at 80°C, and analyzed using a Bruker S4 T-STAR instrument. This procedure determined concentrations of Al, Ti, Ca, K, Mg, S, Si, Cr, Mn, and Fe. To ensure precision and account for potential sample heterogeneity, each carrier was analyzed at two rotational positions (0° and 90°). Measurement uncertainty was quantified by calculating the relative error between these replicates, revealing a dependency on mass loading: uncertainties reached up to 15% for samples with very high dust load (> 150 $\mu\mathrm{g/m^3}$) while remaining below 6% for samples with low dust concentrations typically below 38 $\mu\mathrm{g/m^3}$. These variations are attributed to instrumental limitations previously characterized in (Fomba et al., 2020).

Notably, blank silicon measurements for the filters and TXRF sample carriers showed significant, non-reproducible variations due to inconsistent filter densities and surface reflectance. The resulting uncertainties were too high for a meaningful comparison; therefore, silicon was excluded from the analysis. To isolate the mineral dust signal from the background aerosol, the total mineral dust mass concentration was reconstructed from the remaining elemental data following the procedure of Souza et al. (2025)

. In this approach, the concentrations of key crustal elements (Al, Fe, Ca, Ti) are adjusted for their common oxide forms to estimate the total mineral mass. The dust concentrations were quantified using the stoichiometric relationship for crustal elements following Deabji et al. (2021); Souza et al. (2025):

$$\mathrm{MD} = 1.16 \times ((1.90 \times \mathrm{Al}) + (23.3 \times \mathrm{Ca}) + (2.09 \times \mathrm{Fe}) + (1.67 \times \mathrm{Ti})) . \quad (24)$$

Following established classification for mineral dust events in the Cabo Verde region (Souza et al., 2025), a mineral dust mass concentration threshold of $\geq$38 $\mu g/m^3$ was applied. The threshold was chosen based on long-term analysis of PM10 concentrations at the CVAO sampling site, during which dust concentrations were consistently high. This threshold, combined with air mass back-trajectory analysis, serves to distinguish significant long-range transported dust events from maritime background or localized aerosols. This screening resulted in ~~measurements from 17 filters that were taken into account for the final validation dataset~~a final validation set consisting of 33 PM2.5 and 47 PM10 filter samples.

4 Model ~~validation~~comparison framework

4.1 ~~Northern Africa~~Evaluation methodology

To ~~assess the implementation of the modified mineral simulation approach in the~~ ensure a robust comparison between COSMO5.05~~-MUSCA emission scheme (Section 2.3), first we compare the results with the MONARCH reference shown in Fig.~~ -MUSCAT simulations and in-situ observations, the model output is spatio-temporally sampled to align with the specific characteristics of each measurement campaign. Spatially, model variables were extracted from the grid cells corresponding to the geographic coordinates of the sampling sites. Temporally, hourly model outputs were averaged over the specific integration times of the filter samples. This alignment accounts for varying sampling durations, ranging from the high-frequency UAV cycles during JATAC 2022 to the day-long ground-based periods of the DUSTRISK 2022 campaign. To ensure temporal concurrency, a rounding convention is applied: if a sampling interval began or ended within 30 minutes of a full hour, the nearest hourly model timestep is used to define the averaging window. For example, a sampling period from 10:00 to 12:15 is matched with the model average from 10:00 to 12:00, while a period from 10:10 to 12:36 is matched with the 10:00 to 13:00 simulated average.

For the compilation of North African mineralogical measurements, where exact temporal matching is often not possible due to the lack of concurrent simulated data, the time dimension is constrained by selecting observations from the same seasons as the simulation period. Furthermore, the comparison is restricted to sites and dust trajectories similar to those simulated, ensuring that the emission sites to measurement place pathways in the model are representative of the taken measurements, as detailed in the following section.

It is important to note that the original mineralogy scheme (Gómez Maqueo Anaya et al., 2024) possesses structural constraints regarding the simulation-to-measurements comparisons. Specifically, phyllosilicates are restricted to the clay and fine-silt fractions (BIN01 and 1/2 ~~1 of Gonçalves Ageitos et al. (2023). The comparison is performed for the same soil type, Xerosols Haplic, located in the northwestern Sahara. Figures B1a)~~ BIN03), while minerals such as feldspar and gypsum are defined with

no mass in the clay-sized fraction (BIN01). These inherent model configurations limit the scope of certain comparisons where observations report these minerals in size fractions not supported by the scheme's internal mapping.

The agreement between simulated (S) and observed (O) mineralogical and elemental concentrations is quantified using the Mean Bias (MB) and the Pearson correlation coefficient (r). In this framework, r is utilized as a measure of spatial correlation to evaluate the model's ability to replicate the geographical variability and regional distribution of mineral dust signatures across the study domain. The Pearson correlation coefficient is defined as:

$$r = \frac{\sum_{i=1}^{n}(S_i - \bar{S})(O_i - \bar{O})}{\sqrt{\sum_{i=1}^{n}(S_i - \bar{S})^2 \sum_{i=1}^{n}(O_i - \bar{O})^2}}, \tag{25}$$

where $\bar{S}$ and ~~A) show results obtained~~ $\bar{O}$ represent the mean values of the simulated and observed datasets, respectively, and n is the number of paired spatial samples. Complementary to this, the Mean Bias (MB) identifies systematic over- or underestimations and is calculated as:

$$MB = \frac{1}{n}\sum_{i=1}^{n}(S_i - O_i). \tag{26}$$

4.2 Compilation of North Africa mineralogical measurements

To evaluate the improvements introduced by the modified mineralogy scheme, we compared the DUST-CM-01 and DUST-CM-02 model outputs (see Table 2 for the list of the model experiments) against a compilation of in-situ aerosol mineralogical measurements. This simulated period (January-February 2022) was specifically selected to facilitate a direct comparison with the original ~~method~~ mineralogy scheme presented by Gómez Maqueo Anaya et al. (2024). By maintaining this temporal window, we ensure that differences in model performance are attributable to the updated mineralogical parametrization rather than variations in meteorological forcing across different years.

The core of this compilation is based on the ~~undisturbed mineralogical database PSD, whereas Figs. B1b) and B)depict the normalized PSD emission fluxes after modifying the mineralogical database.~~

~~The two models differ in how the mineral PSD changes are integrated into the emission calculation. MONARCH modifies the mineral PSD directly within its emission parameterization, computing mineral emissions up to 20 µm using the updated BFT formulation of Kok (2011) (Section 2.3). In contrast,~~ global dataset of Perlwitz et al. (2015b). As an initial step, the primary global datasets were subset to include only locations within the modeling domain. The subsequent systematic processing is illustrated in Figure 4, which delineates the pathways for both in-situ observations (gray arrows) and COSMO5.05-MUSCAT ~~adjusts the mineral soil PSD during pre-processing, prior to emission flux calculation. The modified soil PSD is then combined with the Marticorena and Bergametti (1995) emission scheme and distributed across MUSCAT's vertical bin structure.MONARCH also applies a finer size discretization and a narrower size range than~~ simulation results (green arrows). The datasets from both observations and modeling results are represented by yellow boxes with slanted corners. Following the observational pathway, the data undergoes a seasonal filter to retain only measurements representative of Northern Hemisphere (NH) winter months.

This step, represented by the first blue hexagon (decision point) in Figure 4, ensures the observational dataset closely matches the simulation period.

This seasonal constraint is critical, as Saharan dust emissions and transport pathways exhibit pronounced intra-annual variability (Barkan et al., 2004; Schepanski et al., 2009). Specifically, different dust source regions are active during NH winter versus summer, resulting in distinct mineralogical signatures at the receptor sites. By restricting the compilation to the NH winter season, we ensure that the dust sources activated within the model's simulation are representative for the measurement comparison.

The second decision point in Fig. 4 determines the specific simulation data utilized for the comparison based on the number of dust events captured. Measuring campaigns that sampled more than two distinct dust events are categorized as long-term campaigns. For these cases, average mineral mass fractions for the measurement locations grid cell are computed over the entire DUST-CM's simulation period and compared directly against the observed measurements. This approach was applied to the datasets of Adedokun et al. (1989); Enete (2012); Formenti et al. (2008); Kandler et al. (2009, 2011); Møberg et al. (1991) and Panta et al. (2023).

In contrast, shorter campaigns covering two or fewer dust events required a more detailed matching procedure, initiating the "dust event analysis" workflow illustrated in Fig. 4. This methodology integrates HYSPLIT back trajectories (Stein et al., 2015) with satellite-derived dust emission records from the MSG-SEVIRI Dust RGB product (EUMETSAT) to identify probable source regions, following the approach of Schepanski et al. (2007), recently applied in Souza et al. (2025).

To ensure a like-to-like comparison, simulated dust plumes were selected only when their transport pathways and source regions were consistent with the specific observed events. For these cases, the comparison was performed using model output extracted from the grid cell corresponding to the geographic coordinates of the measurement site. The "dust event analysis" workflow, illustrated in Figure 4, begins by identifying the probable source region of the observed sample using HYSPLIT back-trajectories (Stein et al., 2015) intersected with dust emission records from the MSG-SEVIRI Dust RGB product. Simultaneously, backward trajectories for simulated dust events were computed using the LAGRANTO tool (Miltenberger et al., 20 , driven by COSMO5.05 ~~-MUSCAT: it uses eight bins extending to 20~~meteorological fields. Comparison with measurements proceeded only when the simulated and observed plumes originated from the same dust source region, thereby allowing for the direct matching of individual plume signatures with high-resolution model outputs.

Three campaigns required this rigorous event-based matching procedure: Alastuey et al. (2005), Jeong and Achterberg (2014) , and Kandler et al. (2007). For Alastuey et al. (2005), which predates the MSG-SEVIRI record, Meteosat-7 natural color imagery was utilized to track the specific plume transported from southern Algeria to Tenerife on 29 July 2002. For the remaining campaigns, observed plumes were individually matched to simulated events by ensuring that both the HYSPLIT (observational) and LAGRANTO (model) back-trajectories intersected with the same active MSG-SEVIRI dust emission areas.

The final dataset was further expanded with additional North African measurements not considered in the original Perlwitz et al. (2015b) compilation. This expanded dataset is publicly available via the zenodo repository (https://doi.org/10.5281/zenodo.19731364), and the corresponding measurement locations are represented by blue dots in Fig. 3. It should be noted that several historical

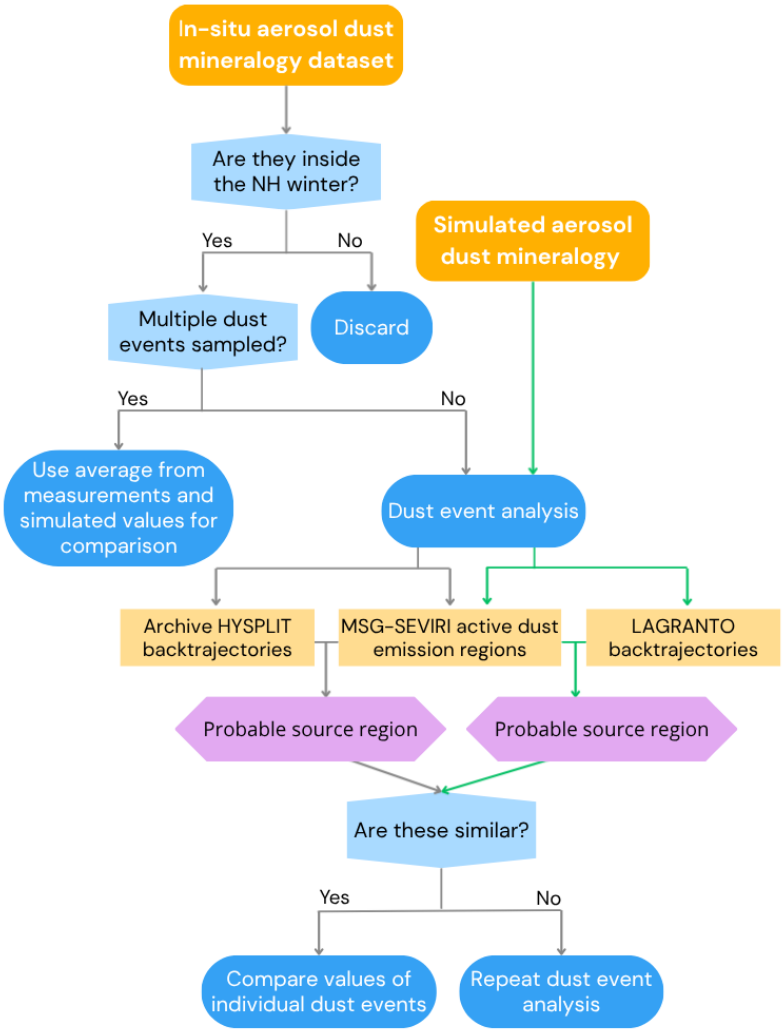

Figure 4. Schematic representation of the workflow used to select and compare in-situ mineral dust measurements with COSMO5.05-MUSCAT simulations. Primary datasets are displayed in yellow boxes with slanted corners and bold text. The analysis pathway for simulated mineralogy is depicted by green lines and arrows, while the in-situ measurement selection process is indicated by gray lines and arrows. Decision points are represented by blue hexagons, procedural steps by blue octagons, supplementary datasets by yellow rectangular boxes, and final outcomes by lavender octagons.

measurements from the 1970s included in the Perlwitz et al. (2015b) study could not be reliably traced using this meteorological and satellite-based framework; consequently, these samples were excluded from the comparison to maintain the integrity of the spatio-temporal matching.

To ensure a robust comparison between varying measurement techniques and model outputs, size-matching was performed based on the reported diameter ranges. For each comparison, the simulated mineral mass fraction was calculated by integrating the mass of a specific mineral across the relevant model bins and dividing this sum by the total simulated dust mass within those same bins. For campaigns reporting bulk measurements, model values were integrated across all available size bins (BIN01 through BIN80). For measurements classified as "clay," the mass fraction was derived from BIN01 + 1/2 ~~um, while COSMO5.05-MUSCAT employs five broader bins reaching 80~~BIN03, while "silt" classifications were compared to the average of 1/2 ~~um (Table 1). Despite these structural differences, both models show clayfractions largely unchanged and a consistent redistribution pattern, with phyllosilicates shifted toward silt-sized categories and a proportional reduction of quartz, as expected~~BIN03 + BIN09 + BIN26 + BIN80. For the campaign reporting high-resolution size distributions (Panta et al., 2023), model bins were matched to the closest reported diameter ranges: 0—1 µm is compared to BIN01; 1—2 µm to BIN03; 4—8 µm to BIN09; 8—16 µm to BIN26; and 32—64 µm to BIN80.

Following these spatio-temporal and size-matching constraints, the final mineral mass fraction comparison is performed using the model output from the specific grid cell corresponding to each measurement site. While measurement uncertainties were not consistently reported across all original studies, they have been included in the comparison with simulated data whenever available.

Despite these rigorous criteria, inherent uncertainties remain. Meteorological anomalies or atypical seasonal transport patterns in the historical data may not be fully captured by the January–February 2022 simulation period. Furthermore, several sites are located near major dust sources where local emissions may dominate the observed mineralogy in ways the model's spatial resolution cannot fully resolve (e.g., Formenti et al., 2008; Kandler et al., 2009; Møberg et al., 1991; Panta et al., 2023).

Finally, inconsistencies in particle size classification across datasets, such as varying definitions for "bulk," "clay," and "silt" fractions, introduce additional uncertainty. While model bins were mapped to these categories as previously described, the sensitivity of these boundaries (e.g., 2.0 vs 2.5 µm) highlights the necessity for high-resolution, well-characterized, and concurrent datasets, such as those obtained during the DUSTRISK 2022 and JATAC 2022 campaigns.

~~Nevertheless, notable differences appear. In the MONARCH reference, quartz fractions increase progressively with particle sizes above 2~~

4.3 Application to Cape Verde measurement campaigns

4.3.1 Mineralogy comparison

Within the Cape Verde campaigns, mineralogical measurements were exclusively available from the JATAC 2022 dataset. For this evaluation, simulated mineral mass fractions from the JAT-CM-01 and JAT-CM-02 experiments were compared against the in-situ observations by extracting model variables from the grid cells corresponding to São Vicente. To ensure temporal and

vertical alignment, the model output is averaged over the specific sampling intervals and the documented altitude ranges of the UAV flights.

In terms of particle size, the JATAC 2022 observations are inherently compatible with the MUSCAT bin definitions, requiring no additional size-matching adjustments. However, BIN80 (32–64 ~~µm, while COSMO5.05-MUSCAT shows only a slight rise between the third and fourth bins, with no further increase toward larger sizes. As a consequence, MONARCH exhibits a continuous decrease of phyllosilicates in the larger bins, a feature absent from~~ µm) is excluded from the assessment due to the analytical detection limits of the ~~COSMO5.05-MUSCAT modified PSD. These discrepancies reflect the coarser bin resolution and broader size range of COSMO5.05-MUSCAT, as well as differences in how the emission schemes interact with the SMA.~~ substrate composition methodology (see Sec. 3). Consequently, each specific mineral mass fractions measurements from the validated samples are directly matched to its corresponding simulated mass fraction to evaluate the model's mineralogical representation.

4.3.2 Elemental comparison

Elemental compositions were evaluated for both the DUSTRISK and JATAC 2022 campaigns. To facilitate a direct comparison with the filter-based measurements, simulated mineral mass concentrations were converted into elemental mass fractions using the stoichiometric percentages defined in Table 3. For each specific element, the total simulated mass is calculated by summing the contributions from all relevant minerals, which is then normalized by the total simulated dust mass to yield an elemental mass fraction. We focus our analysis on Fe, Si, Al, Mg, K, Ca, and S, as these elements serve as key tracers for mineral identification and source attribution in Saharan dust studies (Kandler et al., 2018; Formenti et al., 2011; Panta et al., 2023).

It should be noted that certain mineral groups, specifically feldspar and smectite, exhibit significant natural variability in their elemental ratios. For this study, the stoichiometric coefficients for these species were selected to reflect the chemical signatures most commonly observed in the North African and Saharan regions (e.g., Kandler et al., 2007; Formenti et al., 2014; Scheuvens et al., 2013 . The spatio-temporal extraction followed the protocols described in Section 4, with size-matching adjusted according to the specific sampling characteristics of each campaign:

- **DUSTRISK:** Observational elemental masses from inflow sites were normalized by the total measured mass. To match the reported size fractions, model outputs were aggregated into PM2.5 (~~a) &~~ BIN01 + 1/2 BIN03) and PM10 (~~A): soil mineral PSDs; (b) & (B): aerosol mineral PSDs. Upper panel: MONARCH results, copied from Gonçalves Ageitos et al. (2023) ; normalized mass size distribution~~ BIN01 + BIN03 + BIN09).
- **JATAC:** No size-matching adjustments were required, as the measurement characteristics align directly with the MUSCAT bin definitions.

~~To evaluate whether the modified approach improves the representation of dust mineral aerosol composition , a simulation for~~

Table 3. Mass percentage of ~~minerals for~~ key elements found in the ~~Xerosols Haplic soil type according to Claquin et al. (1999)'s database. Lower panel:~~ COSMO5.05-MUSCAT ~~results; normalized mass size for the Xerosols Haplic soil type according to GMINER~~simulated minerals. ~~(B) aerosol PSD~~ The smectite group is ~~a result of modifying~~ represented by the ~~mineralogical dataset~~ end-member montmorillonite, and feldspar is represented by ~~following~~ a ~~BFT-based approach (Perlwitz et al., 2015a; Gonçalves Ageitos et al., 2023). Quar~~1 ~~:quartz; calc: calcite; feld: feldspars; gyps: gypsum; illi: illite; kaol: kaolinite; smec: smectite; hema: hematite~~1 average of microcline (K-feldspar) and albite (Na-feldspar). This selection is based on common mineralogical assemblages observed in Saharan dust aerosols (Scheuvens et al., 2013; Formenti et al., 2011, 2014).

Mineral	Fe [%]	Si [%]	Al [%]	Mg [%]	K [%]	Ca [%]	S [%]
Hematite	69.94	-	-	-	-	-	-
Illite	1.43	25.25	9.01	1.87	6.03	-	-
Kaolinite	-	21.76	20.90	-	-	-	-
Smectite	-	20.46	9.83	-	-	0.73	-
Quartz	-	46.80	-	-	-	-	-
Feldspar	-	30.89	10.23	-	14.05	0.76	-
Gypsum	-	-	-	-	-	23.28	18.62
Calcite	-	-	-	-	-	40.04	-

5 Model validation

5.1 Mineralogy

To evaluate the performance of the modified mineralogical scheme, we compare the simulated dust composition against two distinct observational benchmarks. First, we assess the model's ability to capture the general characteristics of North African mineral dust using a comprehensive compilation of historical aerosol measurements from across the region. This provides a statistically robust baseline for regional performance. Second, we evaluate the scheme's precision during a specific transport event using high-resolution mineralogical data from the JATAC 2022 campaign. Together, these comparisons offer a multi-scale validation of the model's capacity to represent both climatological means and episodic variability in dust mineralogy.

5.1.1 Compilation of North Africa aerosol mineralogical measurements

Two simulations were performed for the DUSTRISK 2022 ~~campaign was conducted using the approach, shown in yellow solid stars in Fig. 5. A direct comparison is made with the original approach. Mineral mass percentages are compared then between the North Africa compilation of measured values and the simulation approaches. The results are summarized in~~ period to assess the original and modified schemes (DUST-CM-01 and DUST-CM-02, respectively). These runs are compared with historical North African observations from locations and seasons with consistent transport pathways (Section 4.2). Performance metrics, including mean bias and spatial correlations, are synthesized in Table 4 and Fig. 5 ~~, with uncertainties indicated by error bars~~

Table 4. Mean bias (MB) of the mineral mass fractions for the original (DUST-CM-01) and modified (DUST-CM-02) schemes. The MB is calculated against the North African measurement compilation. The number of observation points used for each comparison is indicated in the parentheses (n).

Mineral	MB [%] (n)	
	DUST-CM-01	**DUST-CM-02**
illite	4.3 (9)	9.4 (13)
kaolinite	-5 (12)	1.2 (17)
feldspar	-0.1 (11)	-5.3 (13)
calcite	-1.9 (16)	-2.4 (16)
hematite	-0.2 (9)	-0.2 (9)
quartz	27.4 (21)	1.8 (21)

~~when reported~~(where yellow stars denote the modified scheme). Error bars in Fig. 5 represent the observational uncertainties when reported in the original experimental studies.

The differences between the two simulations are consistent with ~~expectations. Bulk measurements indicate an increase in phyllosilicates (illite and kaolinite in Fig. 5) under the modified approach, accompanied by a decrease in quartz mass fractions. For the clay-only measurements, phyllosilicates are slightly reduced, most clearly reflected in the illite values exceeding 30% in Fig. 5. When averaged over the full simulation period, calcite content increases by 12%, hematite by 17%, and gypsum by 6% compared to the~~ the structural changes described for the modified approach. Comparing the two simulations directly, the transition from the original to the '~~original~~modified' ~~mineralogical scheme. The strongest changes occur for kaolinite and illite, which increase on average by 133% relative to their previous mass percentages, followed by smectite with a 128% increase. Conversely,~~ approach results in a fundamental redistribution of mass among the mineral species. Specifically, DUST-CM-02 produces higher mass fractions for illite and kaolinite and lower mass fractions for quartz and feldspar ~~fractions decrease substantially, by 53% and 49%, respectively~~compared to the DUST-CM-01 run.

~~Overall, kaolinite is the only mineral that shows~~ When evaluated against the North African measurement compilation (Fig. 5), the redistribution of mineral mass in DUST-CM-02 leads to varying impacts on model skill. The most significant improvements are observed for kaolinite, where increased simulated mass fractions reduce the systematic underestimation seen for the DUST-CM-01 run. As shown in Table 4, kaolinite shifts from an underestimation (-5%) to a slight overrepresentation (+1.2%), while also being the only mineral to show a clear improvement in ~~correlation with measurements when using the modified approach, as indicated by the Pearson correlation coefficients~~ spatial correlation (r_p)~~in Fig. 5. Illite also~~. While illite exhibits a marginal ~~improvement based on the change in correlation coefficients. The broad~~ correlation improvement, its overestimation is amplified in DUST-CM-02. This discrepancy is partly attributed to the broad mineralogical definition of illite ~~complicates its~~ groups, which complicates unique identification (Rieder et al., 1998, and references therein)~~, contributing to this ambiguity. Importantly, some measurements that could not previously be compared due to size limitations are now accessible.~~

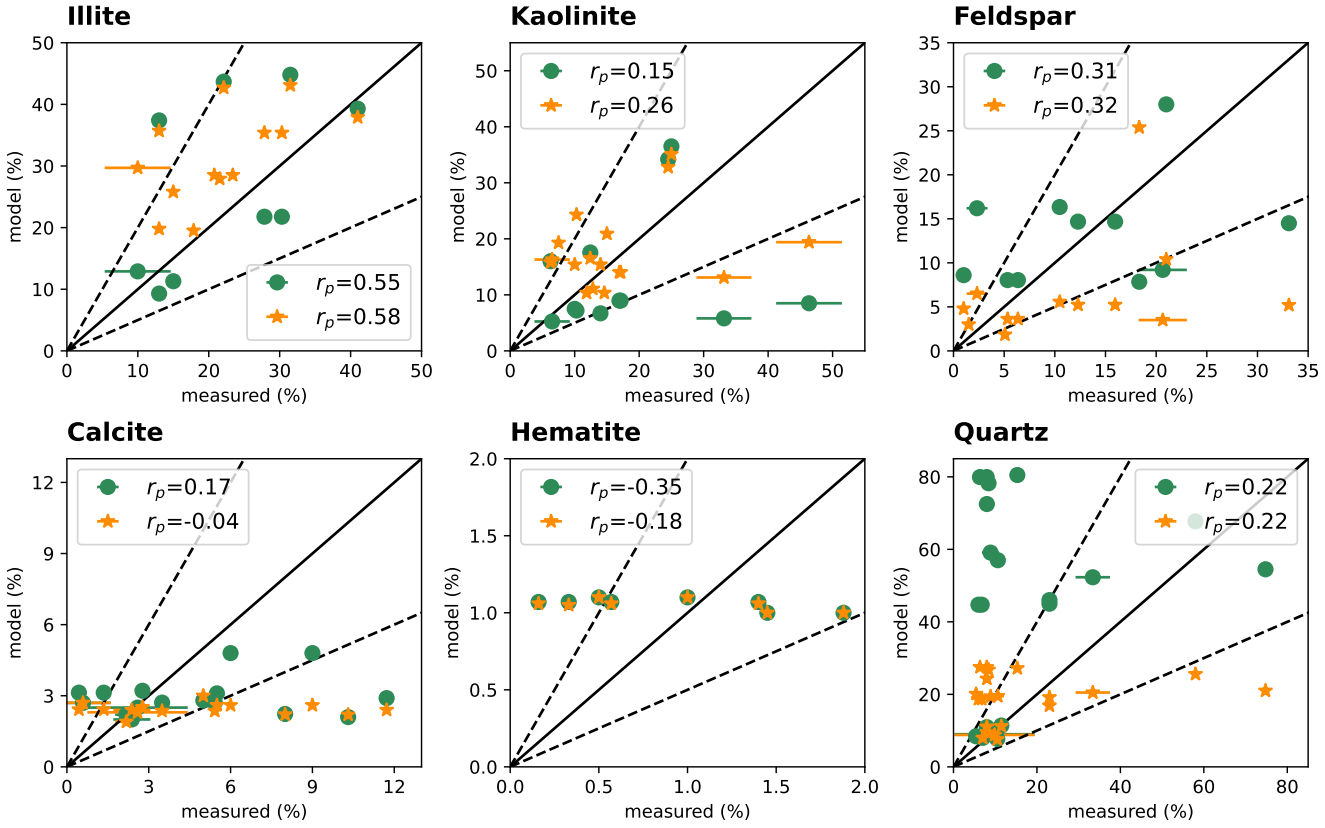

Figure 5. ~~Modified from Fig. 5 in Gómez Maqueo Anaya et al. (2024).~~ Scatterplots of mineral mass percentages of illite, kaolinite, feldspar, calcite, hematite and quartz measured vs. simulated ~~by COSMO5.05-MUSCAT,~~ values. Results from the 'original' ~~mineral emission scheme in~~ simulation (DUST-CM-01) are shown as green solid dots, while the 'modified' ~~version~~ approach (DUST-CM-02) is ~~shown in~~ illustrated by yellow solid stars. The dashed lines represent the ~~ratios of 2:1~~and 1:2 and 2:1 ratios between ~~the~~ simulated and observed ~~mineral percentages~~values. ~~The~~ Error bars indicate observational uncertainties as reported in the original studies; where no error bars are present~~when reported~~ , uncertainties were not provided in the source data. The comparison includes both bulk and size-segregated measurements, with model bins aggregated to match reported diameter ranges as detailed in Section 4.2. Pearson correlation coefficients (r_p.) for each approach are shown in the legend~~represented by r_p~~.

~~On average, both kaolinite and illite are slightly overrepresented in the modified simulation. For illite, the overestimation already present in the original approach is further amplified, whereas kaolinite shifts from underestimation~~ . Notably, however, illite remains the only mineral species among those compared to demonstrate a moderate spatial correlation.

Regarding the non-phyllosilicates minerals, quartz shows the most striking quantitative improvement; its MB is reduced from a ~30% overestimation in the 'original' scheme to ~~slight overestimation~~ only 1.8% in the 'modified' ~~one.~~

~~Feldspar shows little change in correlation between the two approaches, although its simulated mass fractions are substantially reduced in the modified scheme. Both schemes underestimate feldspar compared to observations, but the modified approach~~

~~now enables additional comparisons~~ version, significantly enhancing overall model-observation agreement. Conversely, while the DUST-CM-02 run improves the evaluation scope by including feldspar in the ~~lowest size bin (see~~ finest size fraction (Eq. 20), a 49% reduction in its simulated mass exacerbates the existing model-observation discrepancy, leading to a larger negative MB (Table 4).

Despite these shifts in mass loading, the spatial correlations (r_p) for both quartz and feldspar remain largely unaffected between the two modeling approaches. This stability suggest that for r_p, even though the underlying soil mineralogy distribution changed, the transport patterns remain similar enough to not enact changes on it. Moreover, the impact of the DUST-CM-02 scheme on correlation is evident when considering the expanded observational scope. For illite and kaolinite, the inclusion of previously unrepresented size fractions allowed for a more comprehensive validation against a larger pool of data points (Table 4), resulting in a notable and positive shift in r_p. While a similar size-range expansion was applied to feldspar, the addition of two observational points was insufficient to yield a statistically significant change in its correlation. ~~Quartz correlations likewise remain unchanged, but its content is strongly reduced. This reduction has a marked effect on the difference between model and measured percentages: the overestimation of quartz decreases from a residual average of ~30% with the original scheme to only 1% with the modified scheme.~~

~~Calcite representation worsens, remaining underestimated in both schemes. Hematite~~ The representation of calcite and hematite remains a challenge. Despite moderate increases in their simulated mass fractions (12% and 17%, respectively from DUST-CM-01 to DUST-CM-02), calcite remains underestimated ($MB \simeq$-2%) and hematite correlations remain poor ~~,~~ with negative r_p values~~in both cases. The quantification of hematite is subject to large uncertainties , as it~~ . Interestingly, for the same number of observation points, the two minerals showed diverging trends in spatial skill: hematite r_p improved from -0.35 to -0.18, while calcite correlation degraded from 0.17 to -0.04. The shift in hematite suggests that the mass redistribution in DUST-CM-02 partially corrected previous spatial mismatches, making the model "less wrong" regarding its distribution, even if a negative correlation persists. These discrepancies likely stem from inherent uncertainties in hematite quantification, which occurs both as ~~individual~~ discrete particles and within ~~the crystal lattice of other minerals (Lafon et al., 2004; Zhang et al., 2015). While the average hematite mass fraction increases by 17% across the simulation period (Sect. 2.3), this increase is not reflected in~~ other mineral lattices (Lafon et al., 2004; Zhang et al., 2015). Furthermore, the fact that these domain averaged mass increases are not strongly reflected in the site-specific comparisons of Fig. 5 ~~, where both mineralogical schemes yield similar values~~suggest that the modified mass allocation may have introduced new spatial biases by reducing calcite particles which could result in an incorrect emission calculation for this mineral.

Potential biases in the measurement dataset should also be considered. For instance, the inclusion of the FRAGMENT campaign added ~40% more data to the reference set (Fig. 5 in Gómez Maqueo Anaya et al. (2024)). These measurements, reported by Panta et al. (2023), were collected in the Drâa Valley, Morocco, near active dust source regions. Such localized influences may not be captured by the model, ~~whose~~ as its 28 km spatial resolution represents grid-cell averages and does not resolve small-scale convective events. Likewise, several other campaigns included in the comparison were conducted close to dust sources, reflecting local emissions rather than regional transport observations. ~~As a result, the~~ Consequentially, these point observations may not fully represent the broader mineral fraction distributions that the model is designed to simulate.

Seasonal coverage also plays a role: while some campaigns spanned transitional months with shifts in dominant source regions, the simulations are restricted to NH winter (January–February), potentially missing these seasonal variations ~~(?). Overall, the limited correlation improvements and the inability to draw definitive conclusions are driven by both the~~ (Gebauer et al., 2026) . Ultimately, while the scale mismatch between point ~~measurements~~ measurement and grid-cell ~~averages, as well as the temporal and spatial representativeness of the observations, which introduce multiple sources of uncertainty.~~ average persists, the DUST-CM-02 framework provides a more robust baseline for mineralogical validation. By identifying where temporal and spatial representativeness limit our correlations, this approach clarifies the specific observational constraints needed to further reduce uncertainty in mineral dust modeling.

5.2 ~~Cape Verde - DUSTRISK 2022 campaign~~

~~Scatterplots comparing observed elemental mass percentages of Si, Al, Fe, and Ca against simulated values from COSMO5.05-MUSCAT. Simulated values were derived by multiplying modeled mineral mass by their respective elemental compositions (detailed in Table ??). Green solid circles indicate the original mineral emission scheme, while yellow solid stars represent the modified version. Column headers denote size classifications based on in-situ filter measurements: PM2.5 and PM10. The error bars are represent the measurements' standard deviation. Dashed lines mark the 2:1 and 1:2 ratios between simulated and observed mineral percentages.~~

~~The regional analysis presented above evaluated mineral composition across multiple measurement campaigns spanning different years and locations, where temporal matching between observations and simulations was based on seasonal patterns rather than exact timing. While informative for assessing broad model performance, this approach lacks the precision needed for stringent validation. The DUSTRISK campaign (January–February 2022) addresses this limitation by providing high-resolution measurements of elemental composition and particle size distributions that coincide exactly with the simulation period. Cape Verde's role as a primary receptor site for Saharan dust transport makes these measurements particularly valuable for evaluating the modified mineralogical scheme. Additionally, validating the model through elemental mass fractions calculated from simulated mineral compositions via Table ?? provides a complementary approach for validation of simulated mineralogical content.~~

~~The scatterplots in Fig. 11 demonstrate marked differences in performance between the original and modified mineral emission schemes when evaluated across elemental composition and particle size categories. The modified approach shows improved representation of silicate content, largely attributable to decreased simulated quartz concentrations. In PM2.5, the overestimation by the model decreases from a mean residual of +18% to +4% when applying the modified scheme, while in PM10, the overestimation is reduced as reflected in the change of average residuals from +25% to +15%. However, these Si comparisons must be interpreted cautiously due to potential contamination from the quartz-based filter material used for sampling.~~

~~Measured aluminum content shows pronounced size fractionation, with PM10 exhibiting both elevated concentrations and increased variability relative to PM2.5. For clay-sized particles (PM2.5), the modest reduction in phyllosilicate mass under the modified scheme reduces model overestimation, with mean residuals improving from +7% to +5%. For the silt-size fraction~~

(PM10), an increase in phyllosilicate concentrations likewise strengthens model performance, diminishing the underestimation from a residual mean of -5% to -1%.

Both emission schemes substantially underestimate iron content, with negligible improvement in the modified version. This underestimation contrasts sharply with the mineral-level evaluation (Fig. 5), where hematite concentrations showed reasonable agreement with observations. Although Fe occurs in other simulated minerals, notably illite and certain smectite formulations, these secondary sources do not account for the simulated Fe under representation. This discrepancy between elemental Fe underestimation and adequate hematite simulation highlights a key feature of atmospheric iron. Fe, especially as iron oxides, occurs predominantly as coatings or inclusions on other mineral phases rather than as isolated hematite particles (e.g., Lafon et al., 2004; Kandler et al., 2007; Zhang et al., 2015). Such mineralogical complexity poses fundamental challenges for models that assume external mineral mixing, simulating each mineral as a single particle. Calcium shows comparable systematic underestimation in both schemes, but in this case, it mirrors the underrepresentation of calcite, the dominant Ca-bearing mineral in the model.

As in Fig. 11 but for K, Mg and S.

The potassium content shown in Figure **??** reveals an intriguing size-specific improvement under the modified scheme. For PM2.5, the modified approach yields substantially better agreement with observations, reducing the model's overestimation from a mean residual of +2% to +1%, while PM10 shows negligible change between schemes. The reduction of bias for the clay sized particles stems primarily from the addition of the feldspar fractions to this size category. The improvement is particularly noteworthy given that the preceding mineral-specific feldspar comparison (Fig. 5) revealed neither substantial differences between schemes nor strong correlations with measurements. This discrepancy highlights the value of elemental-level validation in assessing modifications to mineralogical emission schemes, as changes that appear modest in mineral-specific comparisons may produce clearer signals when evaluated through their elemental signatures.

Magnesium displays a size-dependent pattern analogous to that observed for aluminum. Although the earlier illite comparison did not strongly suggested improvements by the modified scheme, an enhancement on the representation emerges from the Mg elemental analysis. For PM2.5, the original scheme's overestimation transitions to a slight underestimation under the modified approach, with changes on the order of 0.05% in mean residuals. In PM10, the model's underestimation diminishes considerably, with mean residuals between simulated and measured values reduced by half.

Sulfur remains systematically and substantially underestimated by the model across both emission schemes, a deficiency directly attributable to the well-documented underrepresentation of gypsum content in SMAs (Gonçalves Ageitos et al., 2023; Song et al., 2
.

The elemental comparisons reveal that while the modified emission scheme successfully addresses several key biases on the mineralogical representation, particularly for Si, Al, and Mg, systematic underestimations persist for certain elements, notably Fe, Ca, and S. However, interpretation of these discrepancies must account for the likelihood that the measured aerosol samples contain contributions from non-mineral sources. The sampling campaign employed long integration periods during the NH winter season, a period characterized by intense biomass burning activity across the Sahel region (Tesche et al., 2011) . Biomass burning emissions are known to contribute substantial quantities of K (Dang et al., 2022), which can confound

~~interpretations of K derived from feldspars and clays in mineral dust (Formenti et al., 2011; Kandler et al., 2007). Additionally, biomass burning can produce fine-mode particles enriched in elements such as Al and Mg through the combustion of vegetation and soil dust entrained in fire plumes (Paris et al., 2010). Disentangling these source contributions would require either shorter sampling intervals, complementary measurements of biomass burning tracers (e.g., black carbon or levoglucosan), or selective sampling of the elevated Saharan Air Layer (SAL), which is more likely less contaminated by other aerosol types.~~

~~The JATAC 2022 campaign provides this latter advantage. Conducted during the NH summer when the SAL is characteristically elevated, JATAC measurements predominantly captured mineral dust with minimal biomass burning interference. This cleaner sampling environment enables a more direct evaluation of the model's mineral composition representation without the confounding factors present in the DUSTRISK NH winter measurements.~~

5.2 ~~Cape Verde - JATAC 2022~~

5.1.1 Comparison with JATAC 2022

5.1.2 ~~Mineral comparison~~

The comparison between ~~JATAC 2022~~ in-situ ~~mineral-like~~ mineral dust aerosol measurements from the JATAC 2022 campaign and COSMO5.05-MUSCAT ~~simulated minerals is presented in~~ simulations is illustrated across several figures: Fig. 6 ~~for clay minerals,~~ presents results for individual and grouped phyllosilicates (labeled as clay minerals), while Fig. 7 ~~for silt minerals, and~~ show the comparisons for quartz, calcite, feldspar and gypsum and Fig. 8 show the comparison for hematite. ~~Both the original scheme (Gómez Maqueo Anaya et al., 2024) and the modified scheme (Section~~For this evaluation, we contrast the original mineralogical scheme (JAT-CM-01; Gómez Maqueo Anaya et al., 2024) with the modified approach (JAT-CM-02; Sect. 2.3)~~are evaluated. Measurements were binned according to~~ . As detailed in the evaluation methodology (Sect. 4.3), measurements were binned to match the COSMO5.05-MUSCAT size categories (BIN01 ~~, BIN03, BIN09,~~ through BIN26)~~; BIN80 measurements are unavailable due to the 30 µm detection limit of SEM-EDX (Kandler et al., 2018)~~.

For ~~clay minerals (illite, kaolinite, and smectite~~ the grouped phyllosilicates in Fig. 6~~)~~, the model generally ~~overrepresents total phyllosilicates~~underestimating the total mass fraction across all size ranges. A key functional improvement of the modified scheme ~~is the inclusion of clay minerals in~~ (JAT-CM-02) is the redistribution of these minerals into coarser size bins, enabling a direct comparison beyond the sub-2.5 ~~µm fraction . In~~ µm fraction where the original scheme was restricted and therefore no direct comparison between schemes can be made. In the finest fraction (BIN01), both approaches show ~~similar overrepresentation. In~~ a similar underrepresentation with MB values of -4.2% for JAT-CM-01 and -6.7% for JAT-CM-02. However, in BIN03, JAT-CM-02 reduces the underestimation by half compared to JAT-CM-01, suggesting that the ~~original scheme underestimates phyllosilicates, while the~~ modified scheme ~~overestimates them by an average of 17%. The best agreement is found in BIN09 with an average residual of +9%, though overestimation increases again in BIN26 (+15%). Looking at individual clays~~more accurately captures the mass distribution in coarser fractions. Within the expanded comparison size range, the model underestimation remains consistent across both coarse size bins (Table 5). Notably, the highest spatial correlations

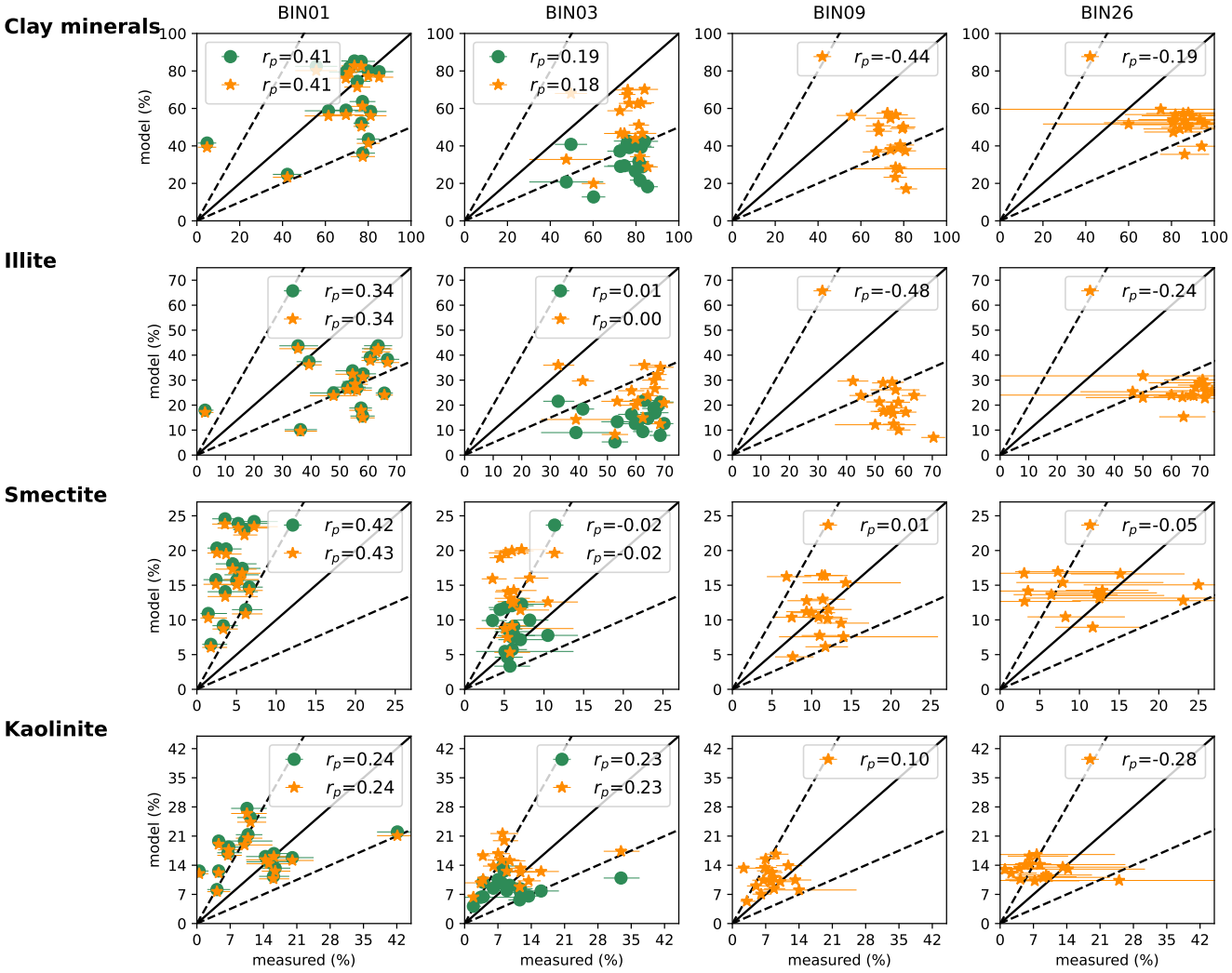

Figure 6. Scatterplots of minerals mass percentages of the grouped "clay minerals", ~~i.e.,~~ illite, smectite, and kaolinite ~~, grouped and individually~~ vs. simulated by COSMO5.05-MUSCAT. 'original' mineral emission scheme (JAT-CM-01) in green solid dots while the 'modified' version (JAT-CM-02) is shown in yellow solid stars. The titles of the columns are size classifications from COSMO5.05-MUSCAT, the diameter ranges they represent are described in Table 1. The dashed lines represent the ratios of 2:1 and 1:2 between the simulated and observed mineral percentages. The error bars represent the lower and upper limits of the confidence intervals (between 2.5% and 97.5%).

Table 5. Mean bias (MB) of the mineral mass fractions for the original (JAT-CM-01) and modified (JAT-CM-02) schemes. The MB is calculated against the JATAC 2022 mineral measurements. The number of observation points used for each comparison is indicated in the parentheses (n).

Mineral	MB [%] (n)							
	JAT-CM-01				JAT-CM-02			
	BIN01	BIN03	BIN09	BIN26	BIN01	BIN03	BIN09	BIN26
clay minerals	-4.2 (17)	-42.2 (17)	–	–	-6.7 (17)	-23 (17)	-32.4 (17)	-32.8 (17)
illite	-21.6 (17)	-43.7 (17)	–	–	-22.6 (17)	-34.5 (17)	-35.8 (17)	-42.2 (17)
smectite	12.5 (17)	2.3 (17)	–	–	11.8 (17)	7.5 (17)	0.3 (17)	2.9 (15)
kaolinite	4.9 (17)	-1.2 (17)	–	–	4.1 (17)	3.9 (17)	3 (17)	4.5 (16)
quartz	1.6 (17)	25.2 (17)	46.1 (17)	62.3 (14)	1.6 (17)	6.7 (17)	9.2 (17)	15.7 (14)
calcite	-1.6 (17)	-4 (17)	-4.2 (18)	1.1 (9)	-1.6 (17)	-4.3 (17)	-4.8 (17)	0.5 (9)
feldspar	–	2.5 (17)	9.9 (17)	14.3 (15)	-1.9 (17)	-1.3 (17)	0.3 (17)	2.2 (15)
gypsum	–	-6.3 (17)	-2.7 (17)	-3.2 (14)	-7.8 (17)	-6.2 (17)	-3.3 (17)	-4 (14)
hematite	-0.9 (17)	-0.5 (17)	-0.1 (17)	0.1 (17)	-0.9 (17)	-0.4 (17)	0.1 (17)	0.1 (17)

(r_p) for the phyllosilicates grouped comparison are moderate and found in BIN01, showing little sensitivity to the structural differences between the two schemes (Fig. 6).

Regarding individual species, measured illite ~~and smectite fractions are extremely low, falling outside the compiled dataset shown in~~ fractions during JATAC 2022 were notably high, falling above the typical ranges in the North African compilation (Fig. 5~~, leading to systematic overestimation in the model . This partly reflects~~). This localized observational trend leads to a systematic underestimation in both model versions. Such discrepancies partly reflects the known challenges in identifying these ~~minerals in measurements (e.g., Rieder et al., 1998), which introduce~~ specific mineral groups in SEM-EDX measurements (Rieder et al., 1998), introducing uncertainties in both ~~observations and~~ the observations and the reference mineralogical databases. ~~Kaolinite shows the opposite behavior, with modeled values underestimates its content overall. The modified scheme reduces the residual in~~ The Pearson correlation coefficient (r_p) remain insensitive to the choice of scheme, with the strongest correlations and lowest mean biases occurring in BIN01. While JAT-CM-02 reduces the bias for BIN03~~but maintains underrepresentation in larger bins.~~ , significant underestimation persists and scales with increasing particle size (Fig. 6 and Table 5).

~~As in Fig. 6 but for silt minerals, i.e., quartz, calcite, feldspar, and gypsum.~~ Conversely, smectite and kaolinite are generally overestimated across the simulations. Both minerals show a performance improvement under JAT-CM-02 in terms of reduced mean biases for BIN01. JAT-CM-02 further exacerbates the overestimation in the coarser BIN03: for kaolinite, it shifts a slight underestimation toward a more pronounced overestimation, while for smectite, the overestimation grows. Among the individual phyllosilicates, the strongest r_p values are consistently found in BIN01, regardless of the scheme employed. While kaolinite

exhibits weak but stable correlations across both BIN01 and BIN03, spatial correlations for the coarser sizes of both minerals remain weak or negative (Fig. 6 and Table 5).

~~A related study by Gonçalves Ageitos et al. (2023) found~~ As expected, the grouped phyllosilicate category exhibits r_p values similar to those of the individual species, as this metric is inherently tied to the mineral distribution within the parent soil. Notably, nearly all spatial correlations for the coarser size bins are negative. This suggests that shifts in the mineral PSD do not necessarily align with the composition of the parent soil. Such statistical decoupling is significant, given that illite and kaolinite distributions vary distinctly across the North African desert (Formenti et al., 2008, 2014; Scheuvens et al., 2013) . This discrepancy may stem from uncertainties in the source maps that define these regional signatures. Alternatively, it may arise from the methodological assumption that phyllosilicates identified in the clay-sized fraction via wet-sieving are similarly present in coarser fractions, despite being undetectable by those specific measurement techniques.

These findings build upon the work of Gonçalves Ageitos et al. (2023) who noted that the GMINER SMA (Nickovic et al., 2012) generally outperforms Journet et al. (2014) SMA in reproducing the spatial distribution of phyllosilicates, ~~although it tends~~ despite a tendency to overestimate kaolinite and smectite while underestimating illite across the Sahara~~region~~. Their analysis ~~also showed that ,~~ further showed that for fine clay-sized fractions, illite is often overestimated near ~~dust~~ sources but underestimated during long-range transport, whereas coarser silt-sized illite is typically underestimated. ~~In contrast, our~~ Our comparison with JATAC 2022 measurements ~~shows consistent overestimation~~ corroborates these trends, showing a persistent underestimation of illite across all simulated size bins. This suggests that while the JAT-CM-02 mass redistribution aims for greater accuracy, it may be amplifying existing uncertainties inherent in regional phyllosilicates source functions.

~~For silt-sized minerals (~~

For the non-phyllosilicates minerals shown in Fig. 7~~), the modified scheme strongly~~ , the JAT-CM-02 run significantly reduces quartz overestimation~~. Average residuals decrease from +23%, +41~~, particularly from BIN03 onward. Mean biases decrease from 25.2%, 46.1%, and ~~+60~~62.3% in the ~~original scheme~~ JAT-CM-01 run for BIN03, BIN09, and BIN26, respectively, to ~~just +5–11%, while calcite remains underestimated across all binswith little improvement under the modified scheme, consistent with earlier findings for 2–20 µm particles (Gonçalves Ageitos et al., 2023). Feldspar~~ 6.7%, 9.2% and 15.7% in JAT-CM-02 (Table 5). Despite these substantial quantitative improvements, overestimations remain high relative to measured values, and the spatial correlations (r_p) exhibit high variability across size bins. Similar to the phyllosilicate results, the two smallest size fractions show no difference between modeling schemes, maintaining weak but consistent correlations. In contrast, the correlation for BIN09 improves under JAT-CM-02, though it remains statistically insignificant, while the correlation for BIN26 worsens (Fig. 7). The sharp decline in quartz correlation for the coarsest fraction (BIN26), likely results from the significant reduction in simulated coarse-mode mass in the JAT-CM-02 scheme. While this reduction successfully corrects the previous mass overestimation, it simultaneously weakens the spatial signal of the quartz plume. As the absolute mass loading in the coarsest bins approaches more realistic, the correlation coefficient becomes increasingly sensitive to localized transport mismatches and the potential 'wash-out' of coarse particles before they reach distant observational sites.

Similarly, feldspar shifts from strong overestimation in ~~the original approach to nearly unbiased results in BIN03 and BIN09 (+~~JAT-CM-01, particularly in the coarser size bins, significantly less biased results across sizes (±1–2%) ~~and slight~~

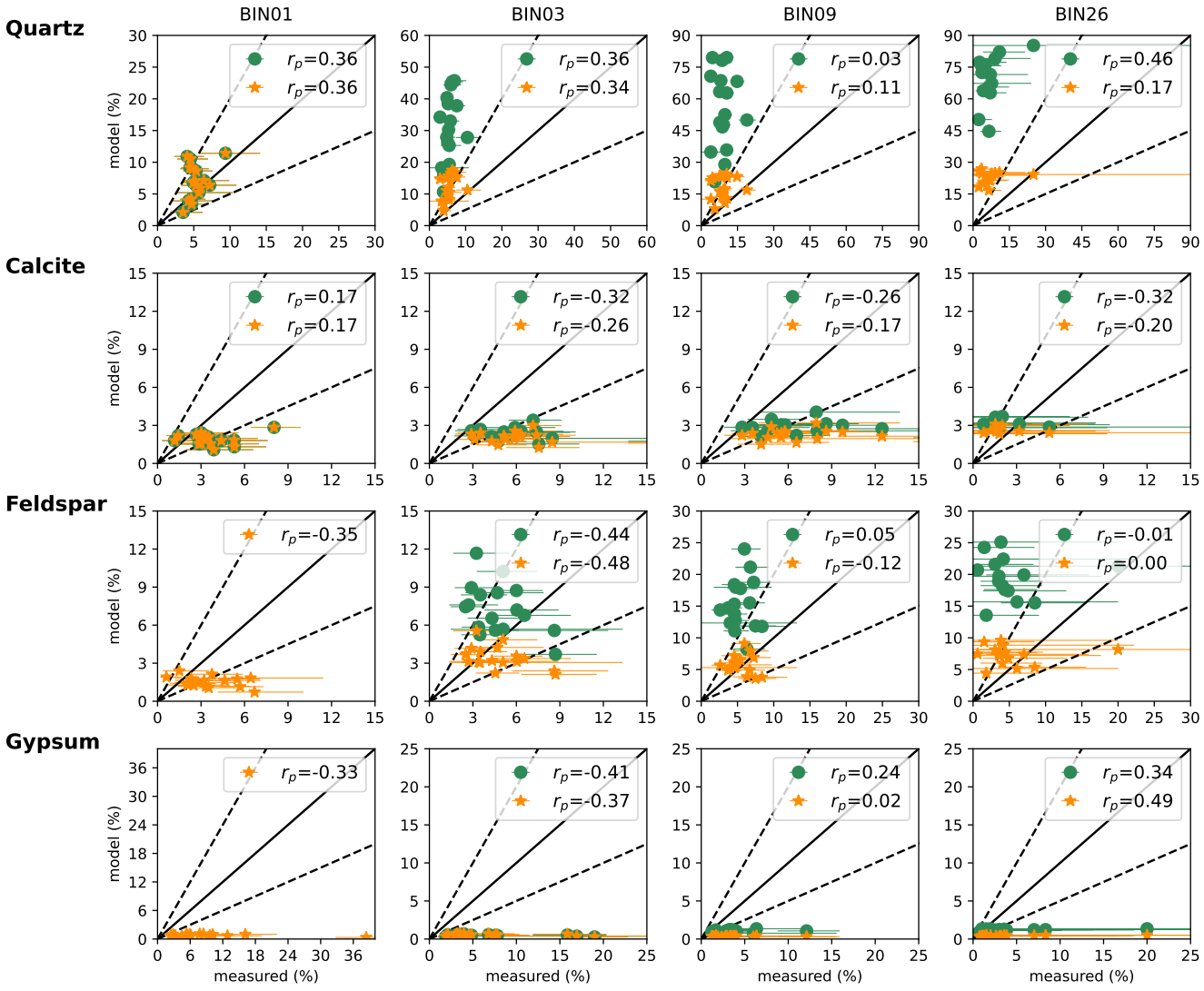

Figure 7. As in Fig. 6 but for quartz, calcite, feldspar, and gypsum. Note: Axis scales vary between panels to optimize the visibility of the fine fractions for quartz, feldspar and gypsum

~~underestimation in BIN01 and BIN26 (~~0.5%). Gypsum is consistently underestimated in both schemes, with higher average residuals resulting from the implementation of the modified scheme.~~ in JAT-CM-02 (Table 5). Interestingly, this localized success during the JATAC 2022 contrasts with the broader North African compilation, where the mass reduction exacerbated existing discrepancies (Table 4). Furthermore, these quantitative improvements in mass magnitude are not reflected in the spatial correlations, which show no improvement across any of the size ranges.

In contrast, calcite and gypsum remain consistently underestimated across all size fractions, with these tendencies generally worsening under the JAT-CM-02 scheme. For calcite, these results align with previous findings for 2–20 µm particles (Gonçalves Ageitos et and the broader North African measurement compilation comparison (Fig. 5). Correlation coefficients for calcite either remain stable or improve marginally under JAT-CM-02, yet they remain negative. Gypsum underestimation is further exacerbated in JAT-CM-02; notably, the r_p for BIN09 degrades despite moderate agreement for BIN26, where JAT-CM-02 shows a meaningful improvement.

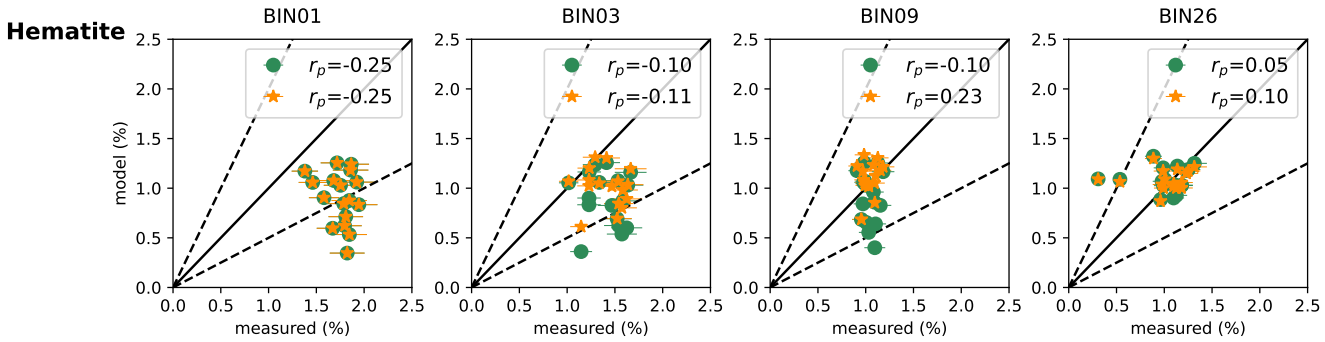

Figure 8. As in Figs.(6 & 7) but for hematite by following Eq. 23 replacing $w_{\mathrm{Feox\%}}$ by $w_{\mathrm{Hem\%}}$. Error bars represent 10% variation from the measurement.

Hematite (Fig. 8) is underestimated by an average of 0.9% in BIN01 under both modeling schemes, with ~~the average residuals decreasing at larger sizes~~mean biases decreasing in the larger size fractions. In BIN03, the ~~modified scheme~~ JAT-CM-02 run slightly reduces the bias~~slightly~~, while in BIN09 and BIN26, the two schemes diverge minimally, ~~yielding both~~ both yielding near-zero ~~average residuals~~ mean biases (0.1%). On average, hematite mass increases modestly by 5% in the modified scheme. While r_p values remain similar in the finer size fractions, the JAT-CM-02 framework shows a notable, albeit weak, improvement for the coarser bins (e.g., BIN09). This is the first instance in which the modified scheme demonstrates a clear advancement in the spatial representation of hematite. Despite persistent biases, hematite (Fig. 8) shows encouraging agreement with observations, supporting the scheme's robustness for applications sensitive to dust optical properties (e.g., Gómez Maqueo Anaya et al., 202 .

Averaged over the JATAC 2022 simulation period, the ~~modified scheme~~ JAT-CM-02 produces substantial increases in phyllosilicates~~(~~, illite, kaolinite, smectite~~; +~~, exhibiting 130% ~~relative to the original scheme) and~~ more mass relative to JAT-CM-01, alongside modest changes in hematite (+5%)~~and calcite (–14%)~~. Conversely, quartz (–61%), feldspar (–56%), and

calcite (–14%), and gypsum (–17%) ~~decline substantially. Comparison with measurements shows that the reductions in~~ mass loadings decline significantly.

Collectively, these results suggest that while mass redistribution effectively addresses systematic magnitude biases for quartz and feldspar ~~improve model-observation agreement, whereas gypsumagreement deteriorates. These inter-scheme differences exceed those observed during the DUSTRISK winter simulations, reflecting the seasonal shift in active dust source regions between NH winter and summer (Section ??; Schepanski et al., 2009)~~in this specific dataset, the underlying soil mineralogy maps remain a primary source of uncertainty. The persistent underrepresentation of calcite and gypsum, which seems to be independent of atmospheric model or dust emission parametrization (e.g., Gonçalves Ageitos et al., 2023), indicates that spatial correlation is limited more by source-map uncertainties than by the emission scheme itself.

5.2 Elemental composition

Cape Verde serves as a critical receptor site for Saharan dust, making its observational record uniquely suited for evaluating the modified mineralogical scheme. In this section, we supplement our mineral-specific analysis with a validation of elemental mass fractions. By converting simulated mineral compositions into elemental abundances (via the relationships defined in Table 3), we establish a secondary, independent metric for assessing model performance.

5.2.1 ~~Elemental comparison~~

While size-resolved elemental comparisons provide a broader perspective on dust composition, they also introduce complexities inherent to field data. Neither modeling approach fully accounts for the observed elemental variability, as measured compositions frequently include non-dust constituents or minerals not simulated in the current framework.

~~As in Fig. 11 but the titles of the columns are size classifications from COSMO5.05-MUSCAT. The error bars represent the lower and upper limits of the confidence intervals (between 2.5% and 97.5%).~~ This is particularly evident in the DUSTRISK 2022 dataset; because these measurements were conducted near the surface during the NH winter, they are more susceptible to interference from local emissions and/or biomass burning plumes from the Sahel (Tesche et al., 2011). In contrast, the JATAC 2022 observations were performed within Saharan Air Layer, typically considered as pure dust during NH summer. However, minor contamination during atmospheric transit remains possible.

~~Size-resolved elemental comparisons offer a complementary perspective to the mineral-specific evaluations, enabling accurate assessment of scheme performance.~~

5.2.1 JATAC 2022

Figure 9 ~~shows comparisons for~~ compares the observed and simulated concentrations of Si, Al, Fe, and Ca. ~~Silicone content~~ For silicon (Si), the differences between the two schemes are negligible in the finest ~~particles~~ fraction (BIN01~~) shows minimal differences between schemes. In intermediate sizes~~ ; Table 6). However, in the intermediate size ranges (BIN03 and BIN09), the ‘modified’ scheme ~~transforms model overestimation into underestimation.~~ (JAT-CM-02) shifts the model from an overestimation

Table 6. Mean bias (MB) of the elemental mass fractions for the original (JAT-CM-01) and modified (JAT-CM-02) schemes. The MB is calculated against the JATAC 2022 elemental measurements. The number of observation points used for each comparison is indicated in the parentheses (n).

Element	MB [%] (n)							
	JAT-CM-01				JAT-CM-02			
	BIN01	BIN03	BIN09	BIN26	BIN01	BIN03	BIN09	BIN26
Si	-3.6 (17)	0.4 (17)	4.4 (17)	14.1 (17)	-3.7 (17)	-4.5 (17)	-5.3 (17)	0.9 (17)
Al	-2.8 (17)	-6.5 (17)	-8.8 (17)	-9.4 (17)	-2.9 (17)	-4.6 (17)	-5 (17)	-4.4 (17)
Fe	-10.3 (17)	-7.6 (17)	-6 (17)	-5.2 (17)	-10.3 (17)	-7.4 (17)	-5.5 (17)	-4.8 (17)
Ca	-2.8 (17)	-2.3 (17)	-2.3 (17)	-1.2(17)	-2.6 (17)	-2.4 (17)	-2.7 (17)	-1.7 (17)
K	-0.2 (17)	-0.4 (17)	0.1 (17)	0.1 (17)	-0.1 (17)	-0.3 (17)	-0.1 (17)	-0.1 (17)
Mg	-1.2 (17)	-1.6 (17)	–	–	-1.2 (17)	-1.5 (17)	-1.5 (17)	-1.3 (17)
S	–	-1.1 (17)	-0.4 (17)	-0.4 (17)	-1.3 (17)	-1.1 (17)	-0.5 (17)	-0.5 (17)

to an underestimation. Notably, the magnitude of this underestimation exceeds the previous overestimation, result that initially seems to contradict the substantial quartz overestimation identified for these size categories (Table 5).

Since quartz is not the only contributor to Si mass (Table 3), this underestimation likely stems from the compounded effect of stark reductions in feldspar and quartz that are not fully compensated for by the increase in phyllosilicates. This supports a hypothesis that non-simulated, high-Si minerals, such as those in the mica (e.g., muscovite) or chlorite groups, may be missing from the model (Scheuvens et al., 2013), while adding to the measured Si mass. In the coarsest bin (BIN26), ~~silicone overestimation persists in both schemes but is substantially reduced under the modified approach, with mean residuals improving from +14% to approximately 0% . The silicone improvements trace directly to reduced~~ while both schemes overestimate Si, JAT-CM-02 significantly mitigates this bias, reducing the mean bias from 14.1% to 0.9% (Table 6). This improvement is directly attributable to the substantial reduction of quartz content in ~~the modified scheme (Fig. 7), confirming that , for some elements, corrections to mineral abundances effectively translate to improved elemental representation.~~ JAT-CM-02 for this size category (Table 5). Ultimately, this demonstrates that refining mineral abundances can effectively improve elemental mass representation even when spatial correlations remain stagnant or degrade, a trend consistent with quartz comparisons across both the North African compilation (Fig. 5) and the JATAC 2022 dataset (Fig. 7).

Aluminum exhibits a clear size-dependent improvement ~~pattern~~ across the bin-resolved ~~analysis. BIN01 shows~~ mean biases (Table 6). While no significant changes ~~between schemes, while BIN03 reduces underestimation from -7% to -5%, BIN09 improves from -9% to -5%, and BIN26 improves from -10% to -5% in average residuals. This~~ occur in BIN01, all other size bins show a progressive reduction in ~~aluminum underestimationwith increasing particle size~~ underestimation. This improvement directly reflects the redistribution of clay minerals into larger size fractions ~~in~~ within the 'modified' scheme, a ~~change that better reflects the aggregated nature~~ shift that better captures the aggregated state of phyllosilicates during emis-

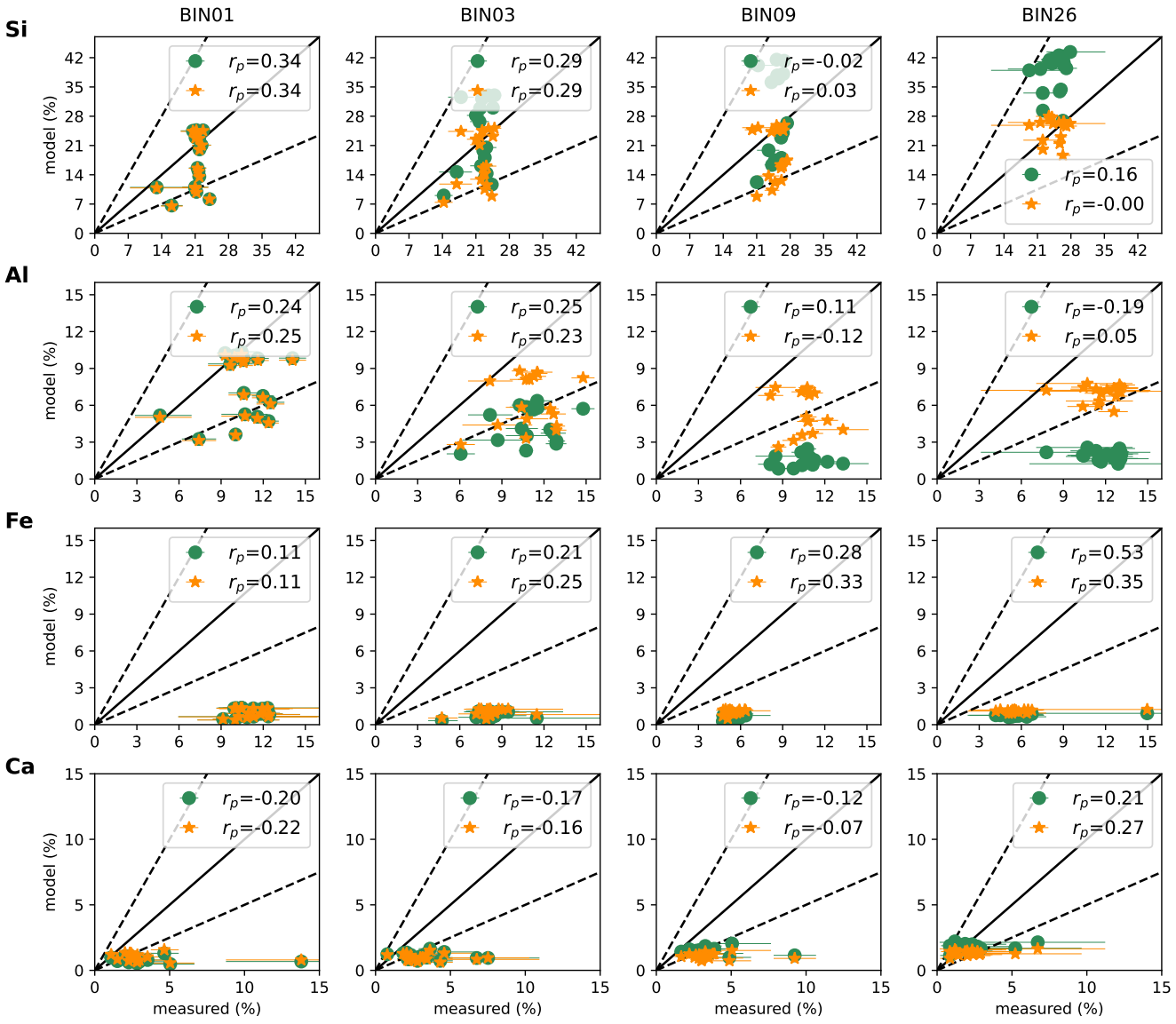

Figure 9. Scatterplots of observed elemental mass percentages of Si, Al, Fe, and Ca against simulated by COSMO5.05-MUSCAT. Simulated values were derived by multiplying modeled mineral mass by their respective elemental compositions (detailed in Table 3). Green solid circles indicate the original mineral emission scheme (JAT-CM-01), while yellow solid stars represent the modified version (JAT-CM-02). The titles of the columns are size classifications from COSMO5.05-MUSCAT (Table 1). The dashed lines represent the ratios of 2:1 and 1:2 between the simulated and observed mineral percentages. The error bars represent the lower and upper limits of the confidence intervals (between 2.5% and 97.5%).

sion and ~~transport~~atmospheric transport. Persistent underestimation, however, may be attributed to the presence of high-Al, non-simulated minerals such as chlorite (Scheuvens et al., 2013). This mass redistribution is particularly encouraging, as the resulting Al concentrations align more closely with observations than the individual mineral comparisons might suggest (Table 5). Nonetheless, these improvements in mass bias do not extend to the spatial correlation coefficients (r_p), which show a slight degradation in the JAT-CM-02 scheme (Fig. 9). This suggests that while the mass balance is improved, the inherently weak correlation, likely driven by the influence of non-simulated minerals, is further exacerbated by the proposed mass redistribution. ~~This feature is also observed in the DUSTRISK elemental comparison for coarser sizes (Fig. 11). Notably, however, the PM2.5 overestimation observed in the DUSTRISK campaign does not appear in this size-resolved analysis, suggesting either biomass burning contamination in the DUSTRISK samples, which would predominantly affect the fine particle fraction, or methodological differences in fine particle measurement between campaigns.~~

Iron (Fe) content shows negligible sensitivity to the choice of emission scheme choice across all size bins, ~~with severe underestimation in both approaches—a pattern consistent with DUSTRISK (~~as evidence by the persistent and severe underestimation exhibited by the mean bias for both approaches (Table 6). From JAT-CM-02 results, spatial correlations increase for BIN03 and BIN09 but deteriorate further for BIN26 (Fig. ~~11~~9). Notably, the mineral-specific hematite comparison (~~Fig~~Figs. 8~~) also shows no~~ & 5) does not show a comparable underestimation, ~~exposing a critical discrepancy between mineral~~ and while not all Fe is found in hematite, it is still a major carrier from which this level of discrepancy is unexpected. Therefore this discrepancy exposes a critical difference between mineralogical and elemental validation metrics. Given iron oxide's pivotal role in dust-atmosphere interactions (Li et al., 2024, 2021; Song et al., 2024; Zhang et al., 2024), this distinction carries significant implications for radiative and bio-geochemical modeling. This inconsistency reveals an inherent limitation of modeling frameworks that treat minerals as discrete particles with uniform composition. ~~Natural atmospheric dust contains iron primarily as nanoscale oxide coatings or inclusions within clay minerals and quartz rather as well as discrete hematite grains (Kandler et al., 2009; Lafon et al., 2004). Neither current model formulations nor available SMAs capture this heterogeneous iron distribution, resulting in systematic biases detectable only through element-resolved evaluations.~~

~~Calcium~~ The calcium (Ca) comparison in Fig. 9 ~~exhibits minimal differences between emission schemes~~ reveals an increased underestimation in the JAT-CM-02 scheme across all size ~~bins,~~ fractions. This result is consistent with the ~~DUSTRISK results~~ JATAC 2022 mineralogical analysis, where both schemes ~~substantially underestimate Ca content.Interestingly, for calcium in the bin-resolved comparison, the modified scheme worsens this underestimation, suggesting that the modifications proposed to the mineral size distributions, reduced~~ significantly underestimate the concentrations of calcite and gypsum, the primary Ca-bearing ~~minerals beyond what observations support. This systematic Ca deficit aligns with~~ minerals currently simulated (Fig. 7). This bias is further exacerbated by the exclusion of dolomite, a major Ca-rich mineral (Formenti et al., 2014), not accounted for in the ~~mineral-specific evaluation, which identified clear underestimation of calcite and gypsum, the dominant Ca-bearing phases in the simulations~~model simulations. Interestingly, while the spatial correlation increases for the coarsest fraction (BIN26), this may be an artifact of the sampling distribution; the remaining size bins show low or even negative correlations, with no discernible trend of improvement under the modified scheme.

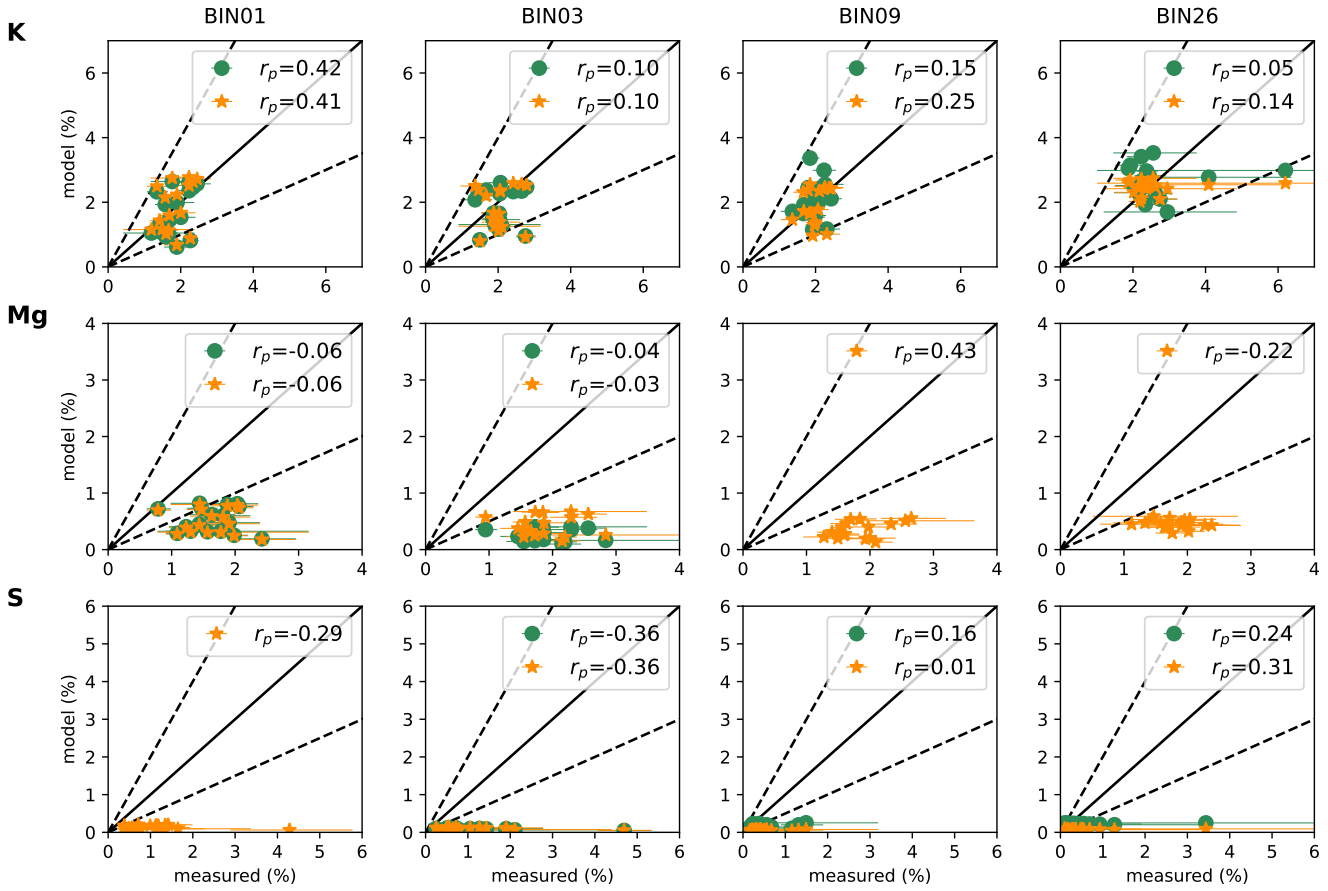

Figure 10. As in Fig. 9 but for K, Mg, and S.

Figure 10 ~~shows the scatterplots for the comparisons between~~ presents the scatterplots comparing the simulated and measured content of K, Mg, and S. ~~Potassium content reveals a complex, size-dependent response to the modifications that varies inconsistently across measurement campaigns.~~ In the bin-resolved analysis ~~,~~ for potassium (K), modified scheme (JAT-CM-02) shows an improvement in both BIN01 ~~shows dramatic improvement under the modified scheme , producing extremely low average mean residuals and substantially reducing the previous underestimations. BIN03 exhibits no significant changes between schemes, while~~ and BIN03, resulting in lower mean biases. In contrast, BIN09 ~~transitions from overestimation to underestimation with comparable magnitudes. However,~~ and BIN26 ~~demonstrates increased underestimation in the modified scheme. This heterogeneous size-dependent behavior contrasts with the DUSTRISK comparison, where the modified approach yielded improved PM2.5 representation (reducing underestimation from -2% to -1% in mean residuals)but negligible PM10 changes. The~~ transition from an overestimation in JAT-CM-01 to an underestimation of comparable magnitude in JAT-CM-02 (Table 6).

Interestingly, while the mineral-specific feldspar comparison (Fig. 7) ~~, meanwhile, showed overall~~ also showed a uniform improvement across all sizes for ~~the modified scheme without the pronounced size-dependent variability observed in the elemental Kanalysis. These inconsistencies across size fractions and measurement campaigns complicate interpretation of the feldspar modifications. K sources and partitioning may be~~ JAT-CM-02, the reduction in bias between schemes was more striking for feldspar than for elemental K. This suggests that potassium partitioning is influenced by factors beyond feldspar size distribution ~~adjustments since~~ alone; specifically, both illite and feldspar contribute ~~K, making it difficult to isolate their individual influences on elemental K budgets. Furthermore, K contributions from biomass burning or other non-mineral aerosol sources cannot be entirely excluded.~~ to the K budget, alongside non-simulated minerals such as white mica. Nevertheless, the mean biases indicate a reasonable agreement between simulated and observed K mass. The increase in r_p values for the two largest size categories in JAT-CM-02 is encouraging, suggesting that the explicit inclusion of illite in these fractions provides a more representative spatial and mass distribution. This stands in contrast to the spatial correlation coefficients for feldspar and illite, which oscillate between weak and negative, (Fig. 7). These discrepancies highlight the value of elemental-level validation in assessing modifications to mineralogical emission schemes, as changes that appear modest in mineral-specific comparisons may produce clearer signals when evaluated through their elemental signatures.

Both emission schemes underestimate magnesium (Mg) in the size-resolved analysis, with no significant differences between the ~~original and modified approaches. particularly intriguing given that the mineral-specific illite comparison described previously showed dramatic over-representation~~ measured mean bias for JAT-CM-01 and JAT-CM-02 (Table 6). This persistent underestimation mirrors the the results for illite, the sole Mg-bearing mineral currently simulated, which exhibits a dramatic underrepresentation by the model (Fig. 6). Interestingly, while the underestimation for illite intensifies in coarser size categories, this trend is not observed for Mg. This divergence suggests two possibilities: either the illite is being misclassified, a common hurdle in complex mineralogical assemblages (e.g., Rieder et al., 1998), or the Mg content assigned to illite in Table 3 is insufficient. Notably, the moderate r_p values found for BIN09 supports the conclusion that the inclusion of illite in larger size fractions is a more physically representative approach to simulating this mineral's distribution. However, the low correlation values in the remaining bins likely reflect the absence of additional Mg sources in the model such as the high-Mg mineral dolomite (Formenti et al., 2014). ~~This disconnect highlights both the challenges in accurately identifying and quantifying illite in complex mineral assemblages and the prevalence of Mg in silicate aggregates and mixed-mineral phases (Kandler et al., 2018) absent from the model simulation capabilities. DUSTRISK exhibited less severe Mg underestimation, highlighting campaign-dependent model performance variability. Despite this difference, both datasets reveal size-dependent improvements under the modified scheme.~~

Sulfur is consistently and substantially underestimated by the model across both emission schemes in the bin-resolved comparison ~~, mirroring the systematic underestimation observed in the DUSTRISK dataset.~~(Fig. 10 and Table 6). This deficiency directly reflects the earlier gypsum-specific mineral comparison ~~and~~ (Fig. 7 and Table 5) and is attributable to the well-documented underrepresentation of gypsum content in SMAs (Gonçalves Ageitos et al., 2023). ~~The persistent S bias across both measurement campaigns and all size fractions highlights a fundamental limitation in current simulation setups regarding sulfate mineral representation.~~

Table 7. Mean bias (MB) of the elemental mass fractions for the original (DUST-CM-01) and modified (DUST-CM-02) schemes. The MB is calculated against the DUSTRISK 2022 elemental measurements. The number of observation points used for each comparison is indicated in the parentheses (n).

Element	MB [%] (n)			
	DUST-CM-01		DUST-CM-02	
	PM2.5	PM10	PM2.5	PM10
Al	6.6 (34)	-4.6 (45)	4.7 (34)	-1.2 (45)
Fe	-2 (34)	-1.7 (45)	-2.1 (34)	-1.4 (45)
Ca	-2.2 (34)	-4.8 (45)	-2.3 (34)	-4.8 (45)
K	2.3 (34)	0.9 (45)	1 (34)	1.1 (45)
Mg	0.1 (33)	-0.6 (40)	-0.1 (33)	-0.3 (40)
S	-0.7 (34)	-0.8 (45)	-0.7 (34)	-0.8 (45)

~~In summary, the JATAC~~ Overall, the transition to the modified scheme demonstrates that refining mineralogical size distributions, specifically the aggregation of phyllosilicates and the reduction of coarse-mode quartz, significantly improves the model's ability to replicate observed elemental mass balances for Si, Al, and K. However, these improvements are not uniformly reflected in the spatial correlation coefficients (r_p), which remain sensitive to the inherent limitations of the current modeling framework.

A notable discrepancy persists for iron; while simulated hematite shows reasonable agreement with observations, total elemental Fe remains severely underestimated across both schemes. This inconsistency underscores a critical disconnect between discrete mineral modeling and the chemical complexity of natural dust. These discrepancies point to a compounded effect of missing mineral phases (e.g., dolomite, muscovite, and chlorite) and the presence of "hidden" elements within nanoscale oxide coatings and silicate aggregates (Kandler et al., 2009; Lafon et al., 2004; Scheuvens et al., 2013). Consequently, while the mass redistribution in JAT-CM-02 moves toward a more physically representative simulation of dust chemistry, a complete elemental closure will likely require the inclusion of these non-simulated minerals and, for Fe, a shift away from assuming uniform mineral compositions across all size fractions.

5.2.2 DUSTRISK 2022 campaign

The scatterplots in Fig. 11 demonstrate marked differences in performance between the original (DUST-CM-01) and modified (DUST-CM-02) mineral emission schemes when evaluated across elemental composition and particle size categories (mean biases detailed in Table 7).

The DUST-CM-02 approach shows a better representation for aluminum, resulting in higher concentrations and greater variability in PM10 compared to PM2.5. For the PM2.5, the modest reduction in phyllosilicate mass under DUST-CM-02 mitigates model overestimation, with mean biases improving from 6.6% to 4.7%. Conversely, increased phyllosilicate concentrations

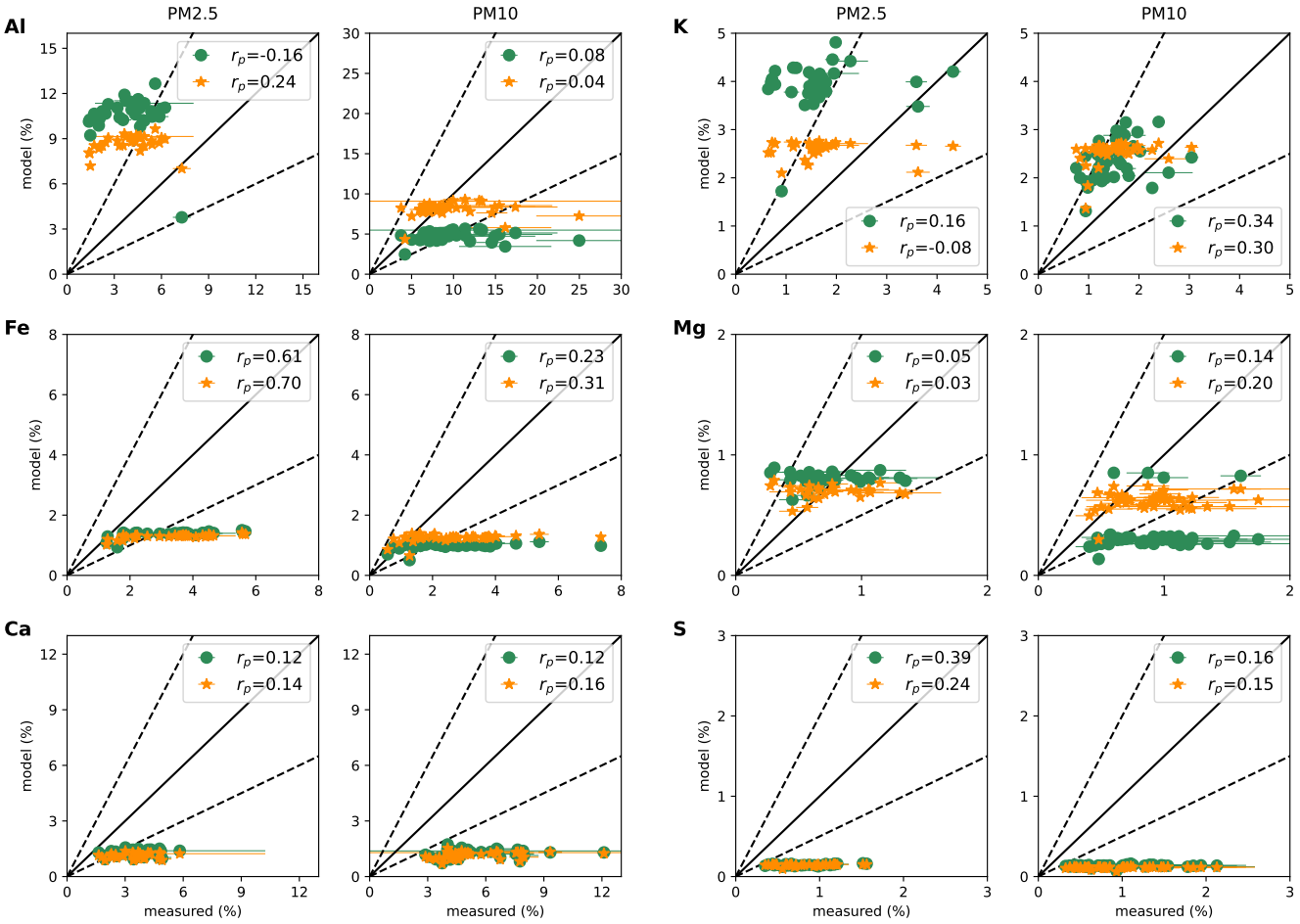

Figure 11. Scatterplots comparing observed elemental mass percentages of Al, Fe, Ca, K, Mg, and S against simulated values from COSMO5.05-MUSCAT. Simulated values were derived by multiplying modeled mineral mass by their respective elemental compositions (detailed in Table 3). Green solid circles indicate the original mineral emission scheme (DUST-CM-01), while yellow solid stars represent the modified version (DUST-CM-02). Column headers denote size classifications based on in-situ filter measurements: PM2.5 and PM10. The error bars represent the measurements' standard deviation. Dashed lines mark the 2:1 and 1:2 ratios between simulated and observed mineral percentages. Note: Axis scales vary between PM2.5 and PM10 panels for Al to optimize the visibility.

in the PM10 fraction, reduces the previous underestimation from -4.6% to -1.2% (Table 7). While these improvements in the coarse fraction align with the JATAC 2022 ~~comparison demonstrates that the modified mineralogical scheme improves the representation of quartz, feldspar, and phyllosilicate distributions in COSMO5.05-MUSCAT, while also extending the size range for meaningful model–measurement evaluation. Persistent biases remain for illite, smectite, calcite, and gypsum, reflecting both measurement challenges and uncertainties in source SMAs. Hematite~~ elemental comparison (Fig. ~~8)shows encouraging agreement in terms of the mineral composition, supporting its robustness for applications sensitive to dust optical properties (e.g., Gómez Maqueo Anaya et al., 2025).However,~~ 9), the PM2.5 overestimation persists in the ~~systematic elemental Fe underestimation~~DUSTRISK 2022 samples but not in JATAC 2022. This discrepancy might be due to methodological differences in fine particle measurement between campaigns. Notably, DUST-CM-02 shows improved spatial correlations for the fine fraction, but not for the coarser fraction (Fig. 11), mirroring the JATAC 2022 comparison results (Fig. 9). This divergence and the consistent underestimation of aluminum in coarser sizes suggests that the model may be missing a specific Al-rich coarse mineral phase, such as muscovite (Scheuvens et al., 2013).

Both emission schemes substantially underestimate iron content, with DUST-CM-02 offering negligible improvement. This systematic underestimation, consistent with the JATAC 2022 elemental comparison (Fig. 9 ~~) reveals that~~ & Table 6), stands in contrast with the mineral-level ~~validation alone provides an incomplete picture of iron representation, underscoring the importance of complementary elemental constraints.~~ evaluation, where simulated hematite concentrations align comparatively better with observations (Figs. 5 & 8). While Fe is present in some forms of smectite, our current framework uses montmorillonite as the proxy for the smectite group due to its dominance in Saharan dust pathways toward Cape Verde (Moreno et al., 2006) . Substituting montmorillonite with an Fe-rich smectite like nontronite would contribute approximately 22% of the smectite mass to the iron budget; however, this adjustment remains insufficient to bridge the substantial gap between the model and measurements (Tables 6 & 7). Regarding the spatial correlation coefficients, r_p for PM2.5 is the highest among all comparisons and further improves with DUST-CM-02. Conversely, correlations for the PM10 are only moderate, though they also show improvement with DUST-CM-02. Interestingly, the model exhibits an inverse relationship between size fraction and correlation strength, with the finest particles yielding the most robust spatial agreement, and simultaneously exhibit a worse mean bias (Fig. 11 & Table 7).

~~The comparison between~~ Calcium shows a consistent systematic underestimation across both schemes (Table 7), directly mirroring the underrepresentation of calcite and gypsum (Figs. 5 & 7). While DUST-CM-02 provides a marginal improvement in r_p, the correlation coefficients for both size categories remain notably similar (Fig. 11). This consistency between size fractions stands in contrast to the JATAC 2022 results (Fig. 9), where positive, albeit weak, correlations were restricted exclusively to the coarsest size category.

The potassium content illustrated in Figure 11 reveals an intriguing, size-specific improvement under the DUST-CM-02 scheme. For the PM2.5 fraction, the modified approach yields better agreement with observations, reducing the mean bias from 2.3% to 1%, while PM10 remains largely unchanged (Table 7). This bias reduction stems primarily from the reallocation of feldspar fractions into the finer size category. Such an improvement is particularly noteworthy because the preceding mineral evaluation of feldspar (Figs. 5 & 7) showed inconsistent performance. These results partially mirror the JATAC 2022 elemental

comparison (Fig. 10), where potassium showed the most significant improvements. However, the discrepancies between campaigns, such as the PM2.5 overestimation which contrasts with JATAC ~~and DUSTRISK results further reveals~~ 2022 results (Table 6), likely reflect seasonal shift in active dust source regions between the ~~value of multi-campaign evaluation . The JATAC NH summer measurements, conducted within the elevated SAL with minimal biomass burning interference, provide cleaner constraints on mineral dust composition than the~~ NH winter ~~DUSTRISK campaign. Key differences emerge: silicon overestimation in fine particles appears only in DUSTRISK, likely reflecting either the presence of other aerosols or methodological differences; potassium shows campaign-dependent size patterns that highlight the difficulty of attributing elemental K to specific mineral sources; and magnesium underestimationis more pronounced in JATAC despite illiteoverestimation, exposing limitations in both SMAs, which inadequately represent Mgspeciation in mixed silicates,~~ and summer (Schepanski et al., 2009) .

For the fine potassium fraction specifically, the consistently low r_p values in both schemes suggest that the simulated spatial distribution does not align with observations. This decoupling points toward an additional, non-simulated K source; given that the observations coincide with the NH winter, this discrepancy could be attributable to Sahelian biomass burning (Tesche et al., 2011), a well-documented regional contributor of fine-mode potassium (Dang et al., 2022; Jahn et al., 2021). Although the current model overestimation in both DUST-CM-01 and ~~modeling frameworks that assume single, compositionally uniform mineral particles~~DUST-CM-02 (Table 7) would superficially argue against the need for additional K mass, the poor spatial correlation suggests that the total observed K is governed by a combination of dust and possible biomass burning patterns that the dust-only schemes cannot reconcile.

Magnesium displays a size-dependent performance pattern analogous to that of aluminum (Fig. 11). Although the earlier illite comparison showed a clear underestimation under the modified scheme (Fig. 6), this Mg elemental analysis reveals a clear enhancement in model representation. In the PM2.5 fraction, DUST-CM-02 shifts the model from a slight overestimation to a slight underestimation, while for PM10, the underestimation is significantly reduced, with mean biases effectively halved (Table 7). In comparison, the JATAC 2022 dataset exhibits a more severe Mg underestimation, highlighting the variability across campaigns. Despite these differences in magnitude, both datasets demonstrate consistent size-dependent improvements and strengthened correlation coefficients under the modified scheme, particularly within the PM10 and BIN09 size categories (Figs. 11 & 10). This cross-campaign consistency reinforces the conclusion that the redistribution of minerals into coarser fractions, specifically Mg-bearing illite, yields a more robust representation of the dust plume's mineralogy.

In contrast, sulfur remains systematically and substantially underestimated across both emission schemes. This persistent bias is accompanied by a deterioration in r_p values (Fig. 11 & Table 7) mirroring the poor performance observed in the JATAC 2022 dataset (Fig. 10).

The elemental comparisons reveal that while the modified emission scheme successfully addresses several key biases on the mineralogical representation, particularly for Si, Al, and Mg, systematic underestimations persist for certain elements, notably Fe, Ca, and S. Interpretation of these discrepancies must consider potential contributions from non-mineral sources, given that the sampling campaign employed long integration periods during the NH winter, a season characterized by intense Sahelian biomass burning activity (Tesche et al., 2011). While biomass burning emissions typically contribute K, Mg, Fe, and Al to

the fine aerosol fraction (Dang et al., 2022; Jahn et al., 2021; Paris et al., 2010), the model continues to overestimate Al and K content despite the improvements in DUST-CM-02. Furthermore, the high accuracy of the Mg simulation suggests that biomass burning may not be the primary driver of the observed mass concentrations in these samples. However, while a minor fraction of the missing Fe could be attributed to biomass burning, the persistence of this underestimation across multiple campaigns (Tables 7 & 6) points more definitively toward a fundamental modeling oversight by omitting Fe-rich minerals and by the simplified assumption of external mineral mixing (discrete particles).

Together, these results highlight both the progress achieved with the 'modified' scheme and the persistent challenges facing mineral dust modeling frameworks. The ~~improvements in~~ improved representation of quartz and feldspar ~~representation in the model demonstrate that refinements to emission size distributions~~ demonstrates that refined emission PSDs and mineral abundances can effectively propagate ~~to both mineral and elemental composition~~through the model to enhance both mineralogical and elemental fidelity. However, ~~the~~ persistent discrepancies in elemental composition~~for Fe and Mg, combined~~, compounded with campaign-specific variability~~in model performance~~, underscore fundamental ~~limitations: current approaches cannot adequately~~ structural limitations. Specifically, current frameworks struggle to represent the heterogeneous internal mixing of iron ~~and iron oxides ,~~ oxides and the complex speciation of magnesium ~~in~~ within silicate aggregates. Furthermore, omissions within the soil mineralogy database remain a significant bottleneck. Addressing these limitations will require not only continued refinement of soil mineral assemblage databases and emission parameterizations, but also expanded observational constraints spanning multiple seasons, source regions, and atmospheric conditions to capture the full complexity of mineral dust composition.

6 Conclusions

The implementation of the 'modified' mineral simulation approach in COSMO5.05-MUSCAT ~~leads to a more accurate~~ significantly enhances the representation of dust aerosol composition~~by~~, as demonstrated by the DUST-CM-02 and JAT-CM-02 simulation periods. By adjusting the soil mineralogical database PSD prior to emission flux calculations~~. Applied to the DUSTRISK 2022 campaign simulation results in comparison with a North African compilation of measurements, the modified scheme substantially improved the representation of phyllosilicates , with kaolinite showing a markedly stronger correlation with observations and illite a slight improvement, though still overestimated.Quartz and feldspar mass fractions decreased significantly, reducing the average quartz residual from 30% to just 1%. Although correlation coefficients for these minerals changed little, ,~~ the ~~redistribution produced size-resolved fractions that more closely matched observations. Calcite decreased modestly and remained underestimated, while hematite correlations stayed weak, consistent with persistent uncertainties in both its measurement and modeling~~model provides a substantially more accurate depiction of phyllosilicates and quartz when compared against North African aerosol measurements (Fig. 5). It effectively resolves the systematic quartz overestimation (Table 4), which validates the redistribution logic. The persistent underestimation of calcite and weak hematite correlations suggest that aerodynamic repartitioning alone cannot compensate for fundamental uncertainties in source soil mineralogy.

Validation with in-situ ~~*mineral-like*~~ elemental concentration-based, mineral phases measurements from JATAC 2022 further confirmed these improvements ~~. By redistributing phyllosilicates into larger size bins ,~~ (Figs. 6 & 7). Validation across discrete size bins confirms that the 'modified' scheme ~~improved agreement with measurements in mid-size ranges (BIN03 and BIN09). Quartz residuals dropped substantially across all bins, with overestimation in BIN26 decreasing from 60% to just 11%. Feldspar representation also improved in mid-size bins, while calcite and gypsum remained underestimated in both approaches. Hematite showed similar results across schemes.~~ successfully extends the model's predictive skill into a broader size spectrum, particularly for silicon- and potassium-bearing minerals. However, the occasional decoupling of improved mean bias from stable or weakened spatial correlations indicates that while the total mass balance is now more realistic, the model's sensitivity to specific source-region variability remains a challenge that purely structural scheme changes cannot yet overcome.

The complementary elemental validation for DUSTRISK and JATAC 2022 ~~revealed~~ campaigns highlights both the strengths and ~~fundamental~~ the inherent limitations of current modeling ~~approaches. In the DUSTRISK 2022 campaign comparisons, several elemental results aligned with their mineral-specific counterparts. For silicon , the modified scheme's substantial reduction in quartz content produced consistent improvements at both scales, with PM2.5 residuals decreasing from +18% to +4% and PM10 from +25% to +15%. Aluminum performance similarly improved in both size fractions, reflecting more accurate~~ frameworks. Across both campaigns, elemental concentrations largely mirrored their mineralogical counterparts. Specifically the correction of silicon and potassium biases demonstrates the consistency and improvement of the modified scheme. The successful refinement of aluminum concentrations across all size fractions further confirms that a more representative size-dependent ~~phyllosilicate distributions. However, systematic iron underestimation persisted in both schemes~~ distribution of phyllosilicates is key to bridging the gap between simulated mineralogy and in-situ observations (Figs. 10 & 11 and Tables 6 & 7).

While the model achieved a more representative size-dependent distribution of phyllosilicates, important discrepancies remain regarding spatial correlation. The differentiated spatial correlations suggest that model benefits are primarily concentrated in the finer size ranges; the persistent mismatch in coarser fractions likely stems from the omission of specific Al-rich coarse minerals, such as muscovite (Scheuvens et al., 2013).

This mineralogical gap is further reflected by the magnesium results. Across both the JATAC and DUSTRISK 2022 datasets, the underestimation of Mg is notably less severe than the pronounced underrepresentation of illite. Given that illite is the sole Mg-bearing mineral in the current model configuration, this discrepancy suggests that the elemental Mg budget is influenced by factors beyond the simulated illite mass alone. This relative "success" in Mg representation compared to the illite mass bias could be due to natural Saharan illite posing a higher degree of Mg-substitution than is currently assumed in the model's static stoichiometry. The persistence of these biases indicates that current soil mineral assemblages fail to accurately capture Mg speciation within mixed silicate aggregates (Kandler et al., 2018). Collectively, these findings underscore that future improvements in model fidelity will require a more comprehensive and complex mineralogical inventory that spans the full particle size spectrum.

Furthermore, significant inter-campaign discrepancies reveal that model validation is inherently sensitive to external factors beyond emission parameterization. For instance, the shift from aluminum underestimation in JATAC 2022 to overestimation in the finest fraction of DUSTRISK 2022 suggests underlying methodological differences in campaign sampling. Furthermore, the more severe Mg deficit noted in JATAC 2022 could reflect reduced biomass burning interference during the NH summer SAL sampling rather than a shift in model performance (Figs. 10 & 11).

The persistent underestimation of elemental iron (Figs. 9 & 11), despite adequate hematite ~~representation at the mineral level.~~mass fractions (Figs. 5 & 8), highlights a fundamental limitation in treating minerals as internally homogeneous. This mineral-element discrepancy exposes a critical modeling limitation: iron exists predominantly as nanoscale oxide coatings or inclusions within other mineral phases (Lafon et al., 2004; Kandler et al., 2007) rather than as discrete particles~~, a complexity that frameworks treating minerals as single,~~. This structural complexity is intrinsically difficult to capture for frameworks that treat minerals as internally homogeneous particles~~cannot capture.~~

~~The JATAC~~. However, the high correlation coefficients observed for the DUSTRISK 2022 ~~size-resolved elemental analysis reinforced these patterns while revealing important inter-campaign differences. Aluminum improvements remained consistent across all size bins but without the fine particle overestimation observed in DUSTRISK , potentially reflecting methodological differences between campaigns. Potassium exhibited campaign-dependent size patterns, underscoring the difficulty of attributing K to specific mineral sources when both feldspar and illite contribute, and the presence of~~ finest fractions indicate that while the total mass is shifted, the model effectively simulates the transport dynamics of iron-bearing clays. Beyond structural complexities, the ~~additional aerosols cannot be completley ruled out. Magnesium underestimation was more pronounced in JATAC despite concurrent illite overestimation, indicating that current soil mineral assemblages cannot adequately represent Mg speciation within mixed silicate aggregates(Kandler et al., 2018). The more severe Mg deficit in JATAC relative to DUSTRISK likely reflects reduced biomass burning interference during NH summer SAL sampling rather than improved model performance. These campaign-specific variations demonstrate that model fidelity depends not only on emission parameterizations but also on sampling methodologies and the presence of non-dust aerosol components~~observed underestimation may also stem from the selection of a non-iron-bearing smectite for this analysis, as well as the exclusion of other iron-contributing minerals from the model.

The persistent underestimation of calcite and gypsum further underscores the limitations of traditional, dispersive soil analysis methods, such as wet-sieving, for constraining dust emission schemes. These methodologies likely dissolve or redistribute soluble minerals as these two, failing to represent the natural state of soil aggregates. Given that shifting initial soil assumptions can alter mineral mass fractions by over 130%, the high sensitivity of the model demonstrates that achieving mineralogical fidelity requires a transition toward non-dispersive soil sampling techniques that preserve the physical and chemical integrity of the parent soil.

The ~~persistent underestimation of calcite and gypsum additionally highlights ongoing limitations in SMAs and the coarse spatial resolution of regional models, which limits the ability to resolve fine-scale dust source variability. The redistribution of mineral mass fractions, such as >130%increases in phyllosilicates and >50% decreases in quartzand feldspar, illustrates the strong sensitivity of modeled composition to SMA assumptions. These shifts are not only relevant for mineralogical accuracy~~

but also for the radiative, optical, and health-related impacts of dust, emphasizing the importance of continued refinement of mineralogy-specific emission schemes and observational constraints at multiple validation scalesseasonal comparison between DUSTRISK (NH winter) and JATAC (NH summer) 2022 further underlines the influence of source region activity. While phyllosilicate increases were consistent across seasons, calcite decreased more strongly during summer (–14%), together with further declines in quartz, feldspar, and gypsum content. These differences reflect shifts in dominant dust-emitting regions and associated meteorology, underscoring the need to account for temporal variability when evaluating mineral fractions in transport models.

Taken together, these results demonstrate both progress and remaining challenges in modeling dust mineralogy. The 'modified' scheme clearly improves the size-resolved representation of phyllosilicates, quartz, and feldspar at across both mineral and elemental scales, but persistent biases for . However, persistent biases in iron, calcium, and magnesium reveal fundamental highlight the inherent limitations in representing the heterogeneous internal mixing and complex speciation characteristic of natural mineral dust. Critically, the elemental validation approach employed here provides a complementary and previously underutilized pathway for model evaluation. By converting simulated mineral compositions to elemental mass fractions and comparing them against measured elemental abundances, this methodology offers several distinct advantages. First, it enables validation against the extensive body of published elemental composition measurements from techniques such as X-ray fluorescence and electron microscopy. Second, it exposes discrepancies between mineral-level and element-level performance that would remain hidden in mineral-only comparisons. Third, it provides independent constraints on mineralogical simulations that can reveal limitations in both emission parameterizations and fundamental assumptions about particle internal structure. The mineral-element discrepancies identified for Fe and Mg exemplify how this dual validation framework diagnoses complexities in dust composition that direct mineral measurements alone cannot adequately capture, underscoring its value for advancing mineralogical representation in atmospheric models.

The seasonal comparison between DUSTRISK (NH winter) and JATAC (NH summer) 2022 further underlines the influence of source region activity. While phyllosilicate increases were consistent across seasons, calcite decreased more strongly in summer (–14%), together with further declines in quartz, feldspar, and gypsum content. These differences reflect shifts in dominant dust-emitting regions and associated meteorology, underscoring the need to account for temporal variability when evaluating mineral fractions in transport models.

Future progress will depend on improved mineralogical datasets, better integration of observations into models, and advances in representing the internal complexity of mineral dust particles. The emergence of hyperspectral measurements from NASA's EMIT mission (Green et al., 2020), alongside field campaigns providing detailed size-resolved composition at both mineral and elemental levels, offers a pathway to reduce current uncertainties. Incorporating such multi-scale observations, particularly for iron oxides and mixed silicate phases, will help resolve biases in key radiatively active minerals and improve constraints on dust–climate interactions. Additionally, developing modeling frameworks that can represent minerals as internally mixed aggregates rather than discrete particles may be necessary to bridge the persistent mineral-element discrepancies identified here. Recent studies (Li et al., 2021, 2024; Obiso et al., 2024) reinforce that refining soil mineral maps and dust size distributions is critical for advancing our understanding of dust's climatic and biogeochemical roles.

Table A1. Ideal normalized mass compositions for the modeled mineral classes. Elements not shown are zero. Value ranges are derived from data by Journet et al. (2008) and https://webmineral.com/.

Class name	Atomic range	Value range
Kaolinite	Si	0.486
	Al	0.483
	Fe	0.01
	Ti	0.02
Illite	Mg	0.027
	K	0.09
	Al	0.218
	Si	0.538
	Ca	0.03
	Fe	0.07
	Ti	0.01
Smectite	Mg	0.029
	Al	0.211
	Si	0.673
	Ca	0.022
	Fe	0.06
Quartz	Si	1.0
Calcite	Ca	1.0
Gypsum	Ca	0.554
	S	0.445
Feldspar	Na	0.02
	Al	0.238
	Si	0.538
	K	0.1
	Ca	0.08
	Fe	0.01
Hematite	Fe	0.9
	Si	0.04
	Al	0.06

Data availability. The dataset for reproducing the graphs presented here are available at https://doi.org/10.5281/zenodo.19731364

.

A JATAC in-situ aerosol measurements: mineral phase criteria

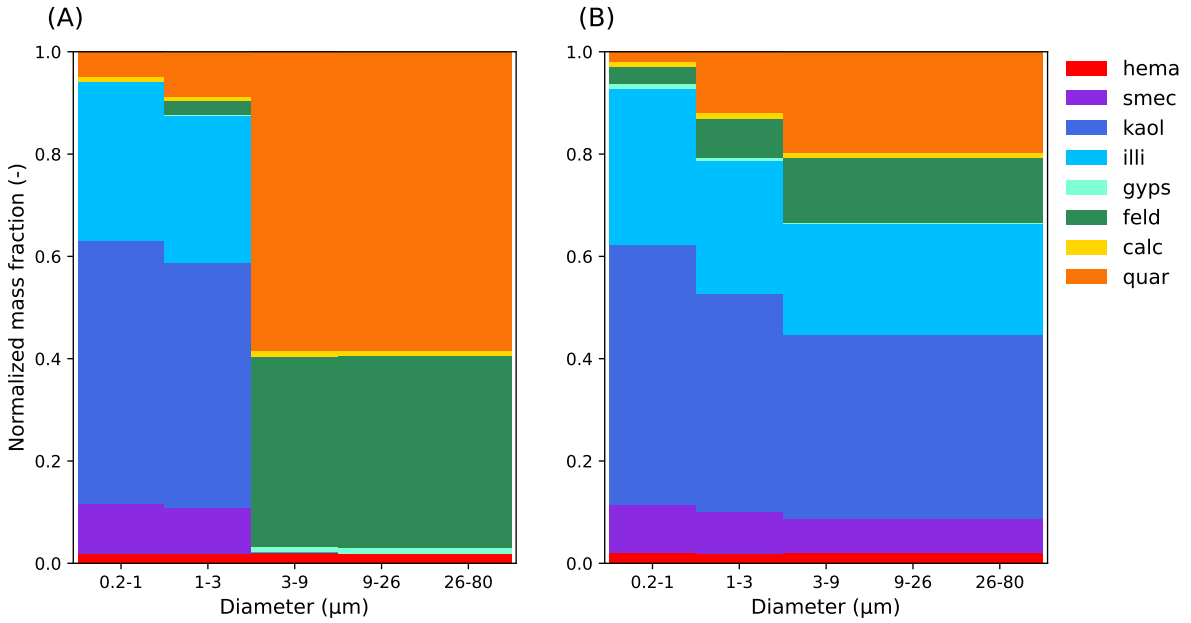

Figure B1. Comparison of normalized mineral mass size distributions for the Haplic Xerosol soil type located in the northwestern Sahara (22.75°N, 6.5°W). Panel (A) illustrates the soil mineral physical size distributions (PSDs) according to the GMINER database. Panel (B) depicts the resulting emitted aerosol mineral PSDs, representing the initial state of the dust plume immediately following emission. The aerosol PSD is derived by applying the BFT-based modification approach (Perlwitz et al., 2015a; Gonçalves Ageitos et al., 2023) to the underlying soil data. Quar: quartz; calc: calcite; feld: feldspars; gyps: gypsum; illi: illite; kaol: kaolinite; smec: smectite; hema: hematite.

B COSMO5.05-MUSCAT Haplic Xerosols

Author contributions. SGMA drafted the manuscript. SA, KK, DA, MK, MH, IT, and KS reviewed and edited the manuscript. SGMA, HB, DA, BH, MH, and KS contributed to the conceptualization of the study. SGMA prepared the figures and organized the datasets. EJSS and KWF were responsible for the elemental analysis of samples collected during the DUSTRISK 2022 campaign. SA and KK conducted the elemental analysis and mineral characterization of the samples collected by MK during the JATAC 2022 campaign. MF led the software development by restructuring the code associated with the MUSCAT dust emission scheme. SGMA, MF, BH, KS, and IT contributed to code development related to the inclusion of mineralogy. SGMA, SA, KK, and KS performed the formal data analysis.

Competing interests. The authors declare that they have no conflict of interest

Acknowledgements. This study is done in the framework of the DUSTRISK (a risk index for health effects of mineral dust and associated microbes) project, funded by the Leibniz Collaborative Excellence Programme Project (grant number K255/2019).

This research has been supported by the German Federal Ministry for Economic Affairs and Energy (BMWi) (grant no. 50EE1721C). Furthermore, we also acknowledge the support through ACTRIS-2 under grant agreement no. 654109 from the European Union's Horizon 2020 research and innovation programme and ACTRIS PPP under the Horizon 2020 – Research and Innovation Framework Programme, H2020-INFRADEV- 2016-2017, Grant Agreement number: 7395302.

We acknowledge and thank the team of OSCM / INMG for their crucial and ongoing support. We further thank ESA and the ASKOS/JATAC teams for the organization of the JATAC(s) campaign(s) and their continuous support.

Further thanks are due to the Deutscher Wetterdienst (DWD) for cooperation and support. We also gratefully acknowledge the Darmstadt Institute for their thorough analysis of the samples, for sharing the results, and for tailoring the analyses to the specific needs of this study. We further thank the National Observatory of Athens for collecting the samples.

Furthermore, ChatGPT ~~was~~ and Gemini were utilized to rephrase and shorten sentences, as well to identify the appropriate prepositions.

References

Adedokun, J. A., Emofurieta, W. O., and Adedeji, O. A.: Physical, mineralogical and chemical properties of harmattan dust at Ile-Ife, Nigeria, Theoretical and Applied Climatology, 40, 161–169, https://doi.org/10.1007/BF00866179, 1989.

Alastuey, A., Querol, X., Castillo, S., Escudero, M., Avila, A., Cuevas, E., Torres, C., Romero, P.-M., Exposito, F., García, O., Pedro Diaz, J., Dingenen, R. V., and Putaud, J. P.: Characterisation of TSP and PM2.5 at Izaña and Sta. Cruz de Tenerife (Canary Islands, Spain) during a Saharan Dust Episode (July 2002), Atmospheric Environment, 39, 4715–4728, https://doi.org/10.1016/j.atmosenv.2005.04.018, 2005.

Albani, S., Mahowald, N. M., Perry, A. T., Scanza, R. A., Zender, C. S., Heavens, N. G., Maggi, V., Kok, J. F., and Otto-Bliesner, B. L.: Improved dust representation in the Community Atmosphere Model, Journal of Advances in Modeling Earth Systems, 6, 541–570, https://doi.org/10.1002/2013MS000279, 2014.

Aryasree, S., Kandler, K., Benker, N., Walser, A., Tipka, A., Dollner, M., Seibert, P., and Weinzierl, B.: Vertical Variability in morphology, chemistry and optical properties of the transported Saharan air layer measured from Cape Verde and the Caribbean, Royal Society Open Science, 11, 231 433, https://doi.org/10.1098/rsos.231433, 2024.

Baldauf, M., Seifert, A., Förstner, J., Majewski, D., Raschendorfer, M., and Reinhardt, T.: Operational Convective-Scale Numerical Weather Prediction with the COSMO Model: Description and Sensitivities, Monthly Weather Review, 139, 3887–3905, https://doi.org/10.1175/MWR-D-10-05013.1, 2011.

Balkanski, Y., Schulz, M., Claquin, T., and Guibert, S.: Reevaluation of Mineral aerosol radiative forcings suggests a better agreement with satellite and AERONET data, Atmospheric Chemistry and Physics, 7, 81–95, https://doi.org/10.5194/acp-7-81-2007, 2007.

Barkan, J., Kutiel, H., Alpert, P., and Kishcha, P.: Synoptics of dust intrusion days from the African continent into the Atlantic Ocean, Journal of Geophysical Research: Atmospheres, 109, 2003JD004 416, https://doi.org/10.1029/2003JD004416, 2004.

Berge, E.: Transboundary air pollution in Europe. Part 2: Numerical addendum to emissions, dispersion and trends of acidifying and eutrophying agents, https://www.osti.gov/etdeweb/biblio/646220, 1997.

Bredeck, G., Dos S. Souza, E. J., Wigmann, C., Fomba, K. W., Herrmann, H., and Schins, R. P.: The influence of long-range transported Saharan dust on the inflammatory potency of ambient PM2.5 and PM10, Environmental Research, 252, 119 008, https://doi.org/10.1016/j.envres.2024.119008, 2024.

Caquineau, S., Gaudichet, A., Gomes, L., Magonthier, M.-C., and Chatenet, B.: Saharan dust: Clay ratio as a relevant tracer to assess the origin of soil-derived aerosols, Geophysical Research Letters, 25, 983–986, https://doi.org/10.1029/98GL00569, 1998.

Cardoso, J., Almeida, S. M., Nunes, T., Almeida-Silva, M., Cerqueira, M., Alves, C., Rocha, F., Chaves, P., Reis, M., Salvador, P., Artiñano, B., and Pio, C.: Source apportionment of atmospheric aerosol in a marine dusty environment by ionic/composition mass balance (IMB), Atmospheric Chemistry and Physics, 18, 13 215–13 230, https://doi.org/10.5194/acp-18-13215-2018, 2018.

Chatziparaschos, M., Daskalakis, N., Myriokefalitakis, S., Kalivitis, N., Nenes, A., Gonçalves Ageitos, M., Costa-Surós, M., Pérez García-Pando, C., Zanoli, M., Vrekoussis, M., and Kanakidou, M.: Role of K-feldspar and quartz in global ice nucleation by mineral dust in mixed-phase clouds, Atmospheric Chemistry and Physics, 23, 1785–1801, https://doi.org/10.5194/acp-23-1785-2023, 2023.

Chiapello, I., Bergametti, G., Chatenet, B., Bousquet, P., Dulac, F., and Soares, E. S.: Origins of African dust transported over the northeastern tropical Atlantic, Journal of Geophysical Research: Atmospheres, 102, 13 701–13 709, https://doi.org/10.1029/97JD00259, 1997.

Claquin, T., Schulz, M., and Balkanski, Y.: Modeling the mineralogy of atmospheric dust sources, Journal of Geophysical Research: Atmospheres, 104, 22 243–22 256, https://doi.org/10.1029/1999JD900416, 1999.

Dang, C., Segal-Rozenhaimer, M., Che, H., Zhang, L., Formenti, P., Taylor, J., Dobracki, A., Purdue, S., Wong, P.-S., Nenes, A., Sedlacek III, A., Coe, H., Redemann, J., Zuidema, P., Howell, S., and Haywood, J.: Biomass burning and marine aerosol processing over the southeast Atlantic Ocean: a TEM single-particle analysis, Atmospheric Chemistry and Physics, 22, 9389–9412, https://doi.org/10.5194/acp-22-9389-2022, 2022.

Darmenova, K., Sokolik, I. N., Shao, Y., Marticorena, B., and Bergametti, G.: Development of a physically based dust emission module within the Weather Research and Forecasting (WRF) model: Assessment of dust emission parameterizations and input parameters for source regions in Central and East Asia, Journal of Geophysical Research: Atmospheres, 114, https://doi.org/10.1029/2008JD011236, 2009.

Deabji, N., Fomba, K. W., El Hajjaji, S., Mellouki, A., Poulain, L., Zeppenfeld, S., and Herrmann, H.: First insights into northern Africa high-altitude background aerosol chemical composition and source influences, Atmospheric Chemistry and Physics, 21, 18 147–18 174, https://doi.org/10.5194/acp-21-18147-2021, 2021.

Di Biagio, C., Formenti, P., Balkanski, Y., Caponi, L., Cazaunau, M., Pangui, E., Journet, E., Nowak, S., Andreae, M. O., Kandler, K., Saeed, T., Piketh, S., Seibert, D., Williams, E., and Doussin, J.-F.: Complex refractive indices and single-scattering albedo of global dust aerosols in the shortwave spectrum and relationship to size and iron content, Atmospheric Chemistry and Physics, 19, 15 503–15 531, https://doi.org/10.5194/acp-19-15503-2019, 2019.

Di Biagio, C., Balkanski, Y., Albani, S., Boucher, O., and Formenti, P.: Direct Radiative Effect by Mineral Dust Aerosols Constrained by New Microphysical and Spectral Optical Data, Geophysical Research Letters, 47, e2019GL086 186, https://doi.org/10.1029/2019GL086186, 2020.

Enete, I.: Harmattan Dust: Composition, Characteristics and Effects on Soil Fertility in Enugu, Nigeria, British Journal of Applied Science & Technology, 2, 72–81, https://doi.org/10.9734/BJAST/2012/950, 2012.

Engelstaedter, S., Tegen, I., and Washington, R.: North African dust emissions and transport, Earth-Science Reviews, 79, 73–100, https://doi.org/10.1016/j.earscirev.2006.06.004, 2006.

Fomba, K. W., Deabji, N., Barcha, S. E. I., Ouchen, I., Elbaramoussi, E. M., El Moursli, R. C., Harnafi, M., El Hajjaji, S., Mellouki, A., and Herrmann, H.: Application of TXRF in monitoring trace metals in particulate matter and cloud water, Atmospheric Measurement Techniques, 13, 4773–4790, https://doi.org/10.5194/amt-13-4773-2020, 2020.

Fomba, K. W., Quaye, D. T., Achterberg, E. P., Marais, E., and Herrmann, H.: Saharan and Namib Dust Phosphorus Fluxes in the North and South Atlantic Regions, ACS Earth and Space Chemistry, 9, 1465–1478, https://doi.org/10.1021/acsearthspacechem.4c00411, 2025.

Formenti, P., Rajot, J. L., Desboeufs, K., Caquineau, S., Chevaillier, S., Nava, S., Gaudichet, A., Journet, E., Triquet, S., Alfaro, S., Chiari, M., Haywood, J., Coe, H., and Highwood, E.: Regional variability of the composition of mineral dust from western Africa: Results from the AMMA SOP0/DABEX and DODO field campaigns, Journal of Geophysical Research: Atmospheres, 113, https://doi.org/10.1029/2008JD009903, _eprint: https://onlinelibrary.wiley.com/doi/pdf/10.1029/2008JD009903, 2008.

Formenti, P., Schütz, L., Balkanski, Y., Desboeufs, K., Ebert, M., Kandler, K., Petzold, A., Scheuvens, D., Weinbruch, S., and Zhang, D.: Recent progress in understanding physical and chemical properties of African and Asian mineral dust, Atmospheric Chemistry and Physics, 11, 8231–8256, https://doi.org/10.5194/acp-11-8231-2011, 2011.

Formenti, P., Caquineau, S., Desboeufs, K., Klaver, A., Chevaillier, S., Journet, E., and Rajot, J. L.: Mapping the physico-chemical properties of mineral dust in western Africa: mineralogical composition, Atmospheric Chemistry and Physics, 14, 10 663–10 686, https://doi.org/10.5194/acp-14-10663-2014, 2014.

Fuster, B., Sánchez-Zapero, J., Camacho, F., García-Santos, V., Verger, A., Lacaze, R., Weiss, M., Baret, F., and Smets, B.: Quality Assessment of PROBA-V LAI, fAPAR and fCOVER Collection 300 m Products of Copernicus Global Land Service, Remote Sensing, 12, 1017, https://doi.org/10.3390/rs12061017, 2020.

Fécan, F., Marticorena, B., and Bergametti, G.: Parametrization of the increase of the aeolian erosion threshold wind friction velocity due to soil moisture for arid and semi-arid areas, Annales Geophysicae, 17, 149–157, https://doi.org/10.1007/s00585-999-0149-7, 1999.

Gebauer, H., Floutsi, A. A., Hofer, J., Haarig, M., Skupin, A., Engelmann, R., Jimenez, C., Wagner, R., and Baars, H.: Characterization of the annual cycle of atmospheric aerosol over Mindelo, Cabo Verde, by means of continuous multiwavelength lidar observations, Atmospheric Chemistry and Physics, 26, 3439–3465, https://doi.org/10.5194/acp-26-3439-2026, 2026.

Gonçalves Ageitos, M., Obiso, V., Miller, R. L., Jorba, O., Klose, M., Dawson, M., Balkanski, Y., Perlwitz, J., Basart, S., Di Tomaso, E., Escribano, J., Macchia, F., Montané, G., Mahowald, N. M., Green, R. O., Thompson, D. R., and Pérez García-Pando, C.: Modeling dust mineralogical composition: sensitivity to soil mineralogy atlases and their expected climate impacts, Atmospheric Chemistry and Physics, 23, 8623–8657, https://doi.org/10.5194/acp-23-8623-2023, 2023.

Green, R. O., Mahowald, N., Ung, C., Thompson, D. R., Bator, L., Bennet, M., Bernas, M., Blackway, N., Bradley, C., Cha, J., Clark, P., Clark, R., Cloud, D., Diaz, E., Ben Dor, E., Duren, R., Eastwood, M., Ehlmann, B. L., Fuentes, L., Ginoux, P., Gross, J., He, Y., Kalashnikova, O., Kert, W., Keymeulen, D., Klimesh, M., Ku, D., Kwong-Fu, H., Liggett, E., Li, L., Lundeen, S., Makowski, M. D., Mazer, A., Miller, R., Mouroulis, P., Oaida, B., Okin, G. S., Ortega, A., Oyake, A., Nguyen, H., Pace, T., Painter, T. H., Pempejian, J., Garcia-Pando, C. P., Pham, T., Phillips, B., Pollock, R., Purcell, R., Realmuto, V., Schoolcraft, J., Sen, A., Shin, S., Shaw, L., Soriano, M., Swayze, G., Thingvold, E., Vaid, A., and Zan, J.: The Earth Surface Mineral Dust Source Investigation: An Earth Science Imaging Spectroscopy Mission, in: 2020 IEEE Aerospace Conference, pp. 1–15, https://doi.org/10.1109/AERO47225.2020.9172731, 2020.

Gómez Maqueo Anaya, S.: Implementation of mineralogical composition of dust aerosol into COSMO-MUSCAT and application to interpret lidar data, Doctoral dissertation, University of Leipzig, 2025.

Gómez Maqueo Anaya, S., Althausen, D., Faust, M., Baars, H., Heinold, B., Hofer, J., Tegen, I., Ansmann, A., Engelmann, R., Skupin, A., Heese, B., and Schepanski, K.: The implementation of dust mineralogy in COSMO5.05-MUSCAT, Geoscientific Model Development, 17, 1271–1295, https://doi.org/10.5194/gmd-17-1271-2024, 2024.

Gómez Maqueo Anaya, S., Althausen, D., Hofer, J., Haarig, M., Wandinger, U., Heinold, B., Tegen, I., Faust, M., Baars, H., Ansmann, A., Engelmann, R., Skupin, A., Heese, B., and Schepanski, K.: Investigating the link between mineral dust hematite content and intensive optical properties by means of lidar measurements and aerosol modeling, Atmospheric Chemistry and Physics, 25, 9737–9764, https://doi.org/10.5194/acp-25-9737-2025, 2025.

Harr, B., Pu, B., and Jin, Q.: The emission, transport, and impacts of the extreme Saharan dust storm of 2015, Atmospheric Chemistry and Physics, 24, 8625–8651, https://doi.org/10.5194/acp-24-8625-2024, 2024.

Harrison, A. D., Lever, K., Sanchez-Marroquin, A., Holden, M. A., Whale, T. F., Tarn, M. D., McQuaid, J. B., and Murray, B. J.: The ice-nucleating ability of quartz immersed in water and its atmospheric importance compared to K-feldspar, Atmospheric Chemistry and Physics, 19, 11 343–11 361, https://doi.org/10.5194/acp-19-11343-2019, 2019.

Heinold, B., Helmert, J., Hellmuth, O., Wolke, R., Ansmann, A., Marticorena, B., Laurent, B., and Tegen, I.: Regional modeling of Saharan dust events using LM-MUSCAT: Model description and case studies, Journal of Geophysical Research: Atmospheres, 112, https://doi.org/10.1029/2006JD007443, _eprint: https://agupubs.onlinelibrary.wiley.com/doi/pdf/10.1029/2006JD007443, 2007.

Heinold, B., Tegen, I., Schepanski, K., Tesche, M., Esselborn, M., Freudenthaler, V., Gross, S., Kandler, K., Knippertz, P., Müller, D., Schladitz, A., Toledano, C., Weinzierl, B., Ansmann, A., Althausen, D., Müller, T., Petzold, A., and Wiedensohler, A.: Regional modelling of Saharan

dust and biomass-burning smoke: Part 1: Model description and evaluation, Tellus B: Chemical and Physical Meteorology, 63, 781–799, https://doi.org/10.1111/j.1600-0889.2011.00570.x, 2011.

Huneeus, N., Schulz, M., Balkanski, Y., Griesfeller, J., Prospero, J., Kinne, S., Bauer, S., Boucher, O., Chin, M., Dentener, F., Diehl, T., Easter, R., Fillmore, D., Ghan, S., Ginoux, P., Grini, A., Horowitz, L., Koch, D., Krol, M. C., Landing, W., Liu, X., Mahowald, N., Miller, R., Morcrette, J.-J., Myhre, G., Penner, J., Perlwitz, J., Stier, P., Takemura, T., and Zender, C. S.: Global dust model intercomparison in AeroCom phase I, Atmospheric Chemistry and Physics, 11, 7781–7816, https://doi.org/10.5194/acp-11-7781-2011, 2011.

Iversen, J. D. and White, B. R.: Saltation threshold on Earth, Mars and Venus, Sedimentology, 29, 111–119, https://doi.org/10.1111/j.1365-3091.1982.tb01713.x, 1982.

Jahn, L. G., Jahl, L. G., Bland, G. D., Bowers, B. B., Monroe, L. W., and Sullivan, R. C.: Metallic and Crustal Elements in Biomass-Burning Aerosol and Ash: Prevalence, Significance, and Similarity to Soil Particles, ACS Earth and Space Chemistry, 5, 136–148, https://doi.org/10.1021/acsearthspacechem.0c00191, 2021.

Jakobsen, H. A., Berge, E., and Jonson, J. E.: The Multi-layer Eulerian Model: Model Description and Evaluation of Transboundary Fluxes of Sulphur and Nitrogen for One Year, DNMI Research Report 49, Meteorological Synthesizing Centre-West, https://books.google.de/books?id=Lu8ivwEACAAJ, eCE Co-Operative Programme for and Europe, Evaluation of the Long Range Transmission of Air Pollutants in and Meteorological Synthesizing Centre–West (Oslo, Norway), 1997.

Jeong, G. Y. and Achterberg, E. P.: Chemistry and mineralogy of clay minerals in Asian and Saharan dusts and the implications for iron supply to the oceans, Atmospheric Chemistry and Physics, 14, 12 415–12 428, https://doi.org/10.5194/acp-14-12415-2014, 2014.

Journet, E., Desboeufs, K. V., Caquineau, S., and Colin, J.-L.: Mineralogy as a critical factor of dust iron solubility, Geophysical Research Letters, 35, https://doi.org/10.1029/2007GL031589, _eprint: https://agupubs.onlinelibrary.wiley.com/doi/pdf/10.1029/2007GL031589, 2008.

Journet, E., Balkanski, Y., and Harrison, S. P.: A new data set of soil mineralogy for dust-cycle modeling, Atmospheric Chemistry and Physics, 14, 3801–3816, https://doi.org/10.5194/acp-14-3801-2014, 2014.

Kalu, A.: Saharan Dust Mobilization, Transport, Deposition, chap. The African Dust Plume: Its Characteristics and Propagation across West Africa in Winter, pp. 95–118, John Wiley and Sons, https://scope.dge.carnegiescience.edu/SCOPE_14/SCOPE_14.html, 1979.

Kandler, K., Benker, N., Bundke, U., Cuevas, E., Ebert, M., Knippertz, P., Rodríguez, S., Schütz, L., and Weinbruch, S.: Chemical composition and complex refractive index of Saharan Mineral Dust at Izaña, Tenerife (Spain) derived by electron microscopy, Atmospheric Environment, 41, 8058–8074, https://doi.org/10.1016/j.atmosenv.2007.06.047, 2007.

Kandler, K., Schütz, L., Deutscher, C., Ebert, M., Hofmann, H., Jäckel, S., Jaenicke, R., Knippertz, P., Lieke, K., Massling, A., Petzold, A., Schladitz, A., Weinzierl, B., Wiedensohler, A., Zorn, S., and Weinbruch, S.: Size distribution, mass concentration, chemical and mineralogical composition and derived optical parameters of the boundary layer aerosol at Tinfou, Morocco, during SAMUM 2006, Tellus B: Chemical and Physical Meteorology, 61, 32, https://doi.org/10.1111/j.1600-0889.2008.00385.x, 2009.

Kandler, K., Schütz, L., Jäckel, S., Lieke, K., Emmel, C., Müller-Ebert, D., Ebert, M., Scheuvens, D., Schladitz, A., Šegvić, B., Wiedensohler, A., and Weinbruch, S.: Ground-based off-line aerosol measurements at Praia, Cape Verde, during the Saharan Mineral Dust Experiment: microphysical properties and mineralogy, Tellus B, 63, 459–474, https://doi.org/10.1111/j.1600-0889.2011.00546.x, 2011.

Kandler, K., Schneiders, K., Ebert, M., Hartmann, M., Weinbruch, S., Prass, M., and Pöhlker, C.: Composition and mixing state of atmospheric aerosols determined by electron microscopy: method development and application to aged Saharan dust deposition in the Caribbean boundary layer, Atmospheric Chemistry and Physics, 18, 13 429–13 455, https://doi.org/10.5194/acp-18-13429-2018, 2018.

Kandler, K., Schneiders, K., Heuser, J., Waza, A., Aryasree, S., Althausen, D., Hofer, J., Abdullaev, S. F., and Makhmudov, A. N.: Differences and Similarities of Central Asian, African, and Arctic Dust Composition from a Single Particle Perspective, Atmosphere, 11, 269, https://doi.org/10.3390/atmos11030269, 2020.

Kelly, J. T., Chuang, C. C., and Wexler, A. S.: Influence of dust composition on cloud droplet formation, Atmospheric Environment, 41, 2904–2916, https://doi.org/10.1016/j.atmosenv.2006.12.008, 2007.

Kezoudi, M., Keleshis, C., Antoniou, P., Biskos, G., Bronz, M., Constantinides, C., Desservettaz, M., Gao, R.-S., Girdwood, J., Harnetiaux, J., Kandler, K., Leonidou, A., Liu, Y., Lelieveld, J., Marenco, F., Mihalopoulos, N., Močnik, G., Neitola, K., Paris, J.-D., Pikridas, M., Sarda-Esteve, R., Stopford, C., Unga, F., Vrekoussis, M., and Sciare, J.: The Unmanned Systems Research Laboratory (USRL): A New Facility for UAV-Based Atmospheric Observations, Atmosphere, 12, 1042, https://doi.org/10.3390/atmos12081042, 2021.

Kezoudi, M., Papetta, A., Kandler, K., Ryder, C. L., Leonidou, A., Keleshis, C., Stopford, C., Thornberry, T., Mamouri, R.-E., Sciare, J., and Marenco, F.: Microphysical and Compositional Differences Between Saharan and Middle Eastern Dust Revealed by UAS Observations, https://doi.org/10.5194/egusphere-2025-5234, 2025.

Kinne, S., Schulz, M., Textor, C., Guibert, S., Balkanski, Y., Bauer, S. E., Berntsen, T., Berglen, T. F., Boucher, O., Chin, M., Collins, W., Dentener, F., Diehl, T., Easter, R., Feichter, J., Fillmore, D., Ghan, S., Ginoux, P., Gong, S., Grini, A., Hendricks, J., Herzog, M., Horowitz, L., Isaksen, I., Iversen, T., Kirkevåg, A., Kloster, S., Koch, D., Kristjansson, J. E., Krol, M., Lauer, A., Lamarque, J. F., Lesins, G., Liu, X., Lohmann, U., Montanaro, V., Myhre, G., Penner, J., Pitari, G., Reddy, S., Seland, O., Stier, P., Takemura, T., and Tie, X.: An AeroCom initial assessment – optical properties in aerosol component modules of global models, Atmospheric Chemistry and Physics, 6, 1815–1834, https://doi.org/10.5194/acp-6-1815-2006, 2006.

Kok, J. F.: A scaling theory for the size distribution of emitted dust aerosols suggests climate models underestimate the size of the global dust cycle, Proceedings of the National Academy of Sciences, 108, 1016–1021, https://doi.org/10.1073/pnas.1014798108, 2011.

Kok, J. F., Parteli, E. J. R., Michaels, T. I., and Karam, D. B.: The physics of wind-blown sand and dust, Reports on Progress in Physics, 75, 106 901, https://doi.org/10.1088/0034-4885/75/10/106901, 2012.

Kok, J. F., Storelvmo, T., Karydis, V. A., Adebiyi, A. A., Mahowald, N. M., Evan, A. T., He, C., and Leung, D. M.: Mineral dust aerosol impacts on global climate and climate change, Nature Reviews Earth & Environment, 4, 71–86, https://doi.org/10.1038/s43017-022-00379-5, 2023.

Kumar, A., Abouchami, W., Galer, S. J. G., Singh, S. P., Fomba, K. W., Prospero, J. M., and Andreae, M. O.: Seasonal radiogenic isotopic variability of the African dust outflow to the tropical Atlantic Ocean and across to the Caribbean, Earth and Planetary Science Letters, 487, 94–105, https://doi.org/10.1016/j.epsl.2018.01.025, 2018.

Lafon, S., Rajot, J.-L., Alfaro, S. C., and Gaudichet, A.: Quantification of iron oxides in desert aerosol, Atmospheric Environment, 38, 1211–1218, https://doi.org/10.1016/j.atmosenv.2003.11.006, 2004.

Lawrence, C. R. and Neff, J. C.: The contemporary physical and chemical flux of aeolian dust: A synthesis of direct measurements of dust deposition, Chemical Geology, 267, 46–63, https://doi.org/10.1016/j.chemgeo.2009.02.005, 2009.

Li, L., Mahowald, N. M., Miller, R. L., Pérez García-Pando, C., Klose, M., Hamilton, D. S., Gonçalves Ageitos, M., Ginoux, P., Balkanski, Y., Green, R. O., Kalashnikova, O., Kok, J. F., Obiso, V., Paynter, D., and Thompson, D. R.: Quantifying the range of the dust direct radiative effect due to source mineralogy uncertainty, Atmospheric Chemistry and Physics, 21, 3973–4005, https://doi.org/10.5194/acp-21-3973-2021, 2021.

Li, L., Mahowald, N. M., Gonçalves Ageitos, M., Obiso, V., Miller, R. L., Pérez García-Pando, C., Di Biagio, C., Formenti, P., Brodrick, P. G., Clark, R. N., Green, R. O., Kokaly, R., Swayze, G., and Thompson, D. R.: Improved constraints on hematite refractive index for estimating climatic effects of dust aerosols, Communications Earth & Environment, 5, 295, https://doi.org/10.1038/s43247-024-01441-4, 2024.

Lieke, K., Kandler, K., Scheuvens, D., Emmel, C., Von Glahn, C., Petzold, A., Weinzierl, B., Veira, A., Ebert, M., Weinbruch, S., and Schütz, L.: Particle chemical properties in the vertical column based on aircraft observations in the vicinity of Cape Verde Islands, Tellus B: Chemical and Physical Meteorology, 63, 497, https://doi.org/10.1111/j.1600-0889.2011.00553.x, 2011.

Mahowald, N., Albani, S., Kok, J. F., Engelstaeder, S., Scanza, R., Ward, D. S., and Flanner, M. G.: The size distribution of desert dust aerosols and its impact on the Earth system, Aeolian Research, 15, 53–71, https://doi.org/10.1016/j.aeolia.2013.09.002, 2014.

Marinou, E., Paschou, P., Tsikoudi, I., Tsekeri, A., Daskalopoulou, V., Kouklaki, D., Siomos, N., Spanakis-Misirlis, V., Voudouri, K. A., Georgiou, T., Drakaki, E., Kampouri, A., Papachristopoulou, K., Mavropoulou, I., Mallios, S., Proestakis, E., Gkikas, A., Koutsoupi, I., Raptis, I. P., Kazadzis, S., Baars, H., Floutsi, A., Pirloaga, R., Nemuc, A., Marenco, F., Kezoudi, M., Papetta, A., Močnik, G., Díez, J. Y., Ryder, C. L., Ratcliffe, N., Kandler, K., Sudharaj, A., and Amiridis, V.: An Overview of the ASKOS Campaign in Cabo Verde, in: 16th International Conference on Meteorology, Climatology and Atmospheric Physics—COMECAP 2023, p. 200, MDPI, https://doi.org/10.3390/environsciproc2023026200, 2023.

Marticorena, B. and Bergametti, G.: Modeling the atmospheric dust cycle: 1. Design of a soil-derived dust emission scheme, Journal of Geophysical Research: Atmospheres, 100, 16 415–16 430, https://doi.org/10.1029/95JD00690, 1995.

Miffre, A., Cholleton, D., Noël, C., and Rairoux, P.: Investigating the dependence of mineral dust depolarization on complex refractive index and size with a laboratory polarimeter at 180.0° lidar backscattering angle, Atmospheric Measurement Techniques, 16, 403–417, https://doi.org/10.5194/amt-16-403-2023, 2023.

Miltenberger, A. K., Pfahl, S., and Wernli, H.: An online trajectory module (version 1.0) for the nonhydrostatic numerical weather prediction model COSMO, Geoscientific Model Development, 6, 1989–2004, https://doi.org/10.5194/gmd-6-1989-2013, 2013.

Moreno, T., Querol, X., Castillo, S., Alastuey, A., Cuevas, E., Herrmann, L., Mounkaila, M., Elvira, J., and Gibbons, W.: Geochemical variations in aeolian mineral particles from the Sahara–Sahel Dust Corridor, Chemosphere, 65, 261–270, https://doi.org/10.1016/j.chemosphere.2006.02.052, 2006.

Murray, B. J., O'Sullivan, D., Atkinson, J. D., and Webb, M. E.: Ice nucleation by particles immersed in supercooled cloud droplets, Chemical Society Reviews, 41, 6519, https://doi.org/10.1039/c2cs35200a, 2012.

Muñoz Sabater, J. and Copernicus Climate Change Service, S.: ERA5-Land hourly data from 2001 to present, https://doi.org/10.24381/CDS.E2161BAC, type: dataset, 2019.

Møberg, J., Esu, I., and Malgwi, W.: Characteristics and constituent composition of Harmattan dust falling in Northern Nigeria, Geoderma, 48, 73–81, https://doi.org/10.1016/0016-7061(91)90007-G, 1991.

Nickovic, S., Vukovic, A., Vujadinovic, M., Djurdjevic, V., and Pejanovic, G.: Technical Note: High-resolution mineralogical database of dust-productive soils for atmospheric dust modeling, Atmospheric Chemistry and Physics, 12, 845–855, https://doi.org/10.5194/acp-12-845-2012, 2012.

Obiso, V., Gonçalves Ageitos, M., Pérez García-Pando, C., Perlwitz, J. P., Schuster, G. L., Bauer, S. E., Di Biagio, C., Formenti, P., Tsigaridis, K., and Miller, R. L.: Observationally constrained regional variations of shortwave absorption by iron oxides emphasize the cooling effect of dust, Atmospheric Chemistry and Physics, 24, 5337–5367, https://doi.org/10.5194/acp-24-5337-2024, 2024.

Panta, A., Kandler, K., Alastuey, A., González-Flórez, C., González-Romero, A., Klose, M., Querol, X., Reche, C., Yus-Díez, J., and Pérez García-Pando, C.: Insights into the single-particle composition, size, mixing state, and aspect ratio of freshly emitted mineral dust from field measurements in the Moroccan Sahara using electron microscopy, Atmospheric Chemistry and Physics, 23, 3861–3885, https://doi.org/10.5194/acp-23-3861-2023, 2023.

Paris, R., Desboeufs, K. V., Formenti, P., Nava, S., and Chou, C.: Chemical characterisation of iron in dust and biomass burning aerosols during AMMA-SOP0/DABEX: implication for iron solubility, Atmospheric Chemistry and Physics, 10, 4273–4282, https://doi.org/10.5194/acp-10-4273-2010, 2010.

Parker, D. J., Burton, R. R., Diongue-Niang, A., Ellis, R. J., Felton, M., Taylor, C. M., Thorncroft, C. D., Bessemoulin, P., and Tompkins, A. M.: The diurnal cycle of the West African monsoon circulation, Quarterly Journal of the Royal Meteorological Society, 131, 2839–2860, https://doi.org/10.1256/qj.04.52, 2005.

Perlwitz, J. P., Pérez García-Pando, C., and Miller, R. L.: Predicting the mineral composition of dust aerosols – Part 1: Representing key processes, Atmospheric Chemistry and Physics, 15, 11 593–11 627, https://doi.org/10.5194/acp-15-11593-2015, 2015a.

Perlwitz, J. P., Pérez García-Pando, C., and Miller, R. L.: Predicting the mineral composition of dust aerosols – Part 2: Model evaluation and identification of key processes with observations, Atmospheric Chemistry and Physics, 15, 11 629–11 652, https://doi.org/10.5194/acp-15-11629-2015, 2015b.

Poggio, L., de Sousa, L. M., Batjes, N. H., Heuvelink, G. B. M., Kempen, B., Ribeiro, E., and Rossiter, D.: SoilGrids 2.0: producing soil information for the globe with quantified spatial uncertainty, SOIL, 7, 217–240, https://doi.org/10.5194/soil-7-217-2021, 2021.

Prigent, C., Aires, F., Rossow, W. B., and Robock, A.: Sensitivity of satellite microwave and infrared observations to soil moisture at a global scale: Relationship of satellite observations to in situ soil moisture measurements, Journal of Geophysical Research: Atmospheres, 110, https://doi.org/10.1029/2004JD005087, 2005.

Pérez García-Pando, C., Miller, R. L., Perlwitz, J. P., Rodríguez, S., and Prospero, J. M.: Predicting the mineral composition of dust aerosols: Insights from elemental composition measured at the Izaña Observatory, Geophysical Research Letters, 43, https://doi.org/10.1002/2016GL069873, 2016.

Rieder, M., Cavazzini, G., D'yakonov, Y. S., Frank-Kamenetskii, V. A., Gottardi, G., Guggenheim, S., Koval', P. W., Müller, G., Neiva, A. M. R., Radoslovich, E. W., Robert, J.-L., Sassi, F. P., Takeda, H., Weiss, Z., and Wones, D. R.: Nomenclature of the Micas, Clays and Clay Minerals, 46, 586–595, https://doi.org/10.1346/CCMN.1998.0460513, 1998.

Rodríguez, S., Calzolai, G., Chiari, M., Nava, S., García, M. I., López-Solano, J., Marrero, C., López-Darias, J., Cuevas, E., Alonso-Pérez, S., Prats, N., Amato, F., Lucarelli, F., and Querol, X.: Rapid changes of dust geochemistry in the Saharan Air Layer linked to sources and meteorology, Atmospheric Environment, 223, 117 186, https://doi.org/10.1016/j.atmosenv.2019.117186, 2020.

Scanza, R. A., Mahowald, N., Ghan, S., Zender, C. S., Kok, J. F., Liu, X., Zhang, Y., and Albani, S.: Modeling dust as component minerals in the Community Atmosphere Model: development of framework and impact on radiative forcing, Atmospheric Chemistry and Physics, 15, 537–561, https://doi.org/10.5194/acp-15-537-2015, 2015.

Schepanski, K., Tegen, I., Laurent, B., Heinold, B., and Macke, A.: A new Saharan dust source activation frequency map derived from MSG-SEVIRI IR-channels, Geophysical Research Letters, 34, https://doi.org/10.1029/2007GL030168, 2007.

Schepanski, K., Tegen, I., and Macke, A.: Saharan dust transport and deposition towards the tropical northern Atlantic, Atmospheric Chemistry and Physics, 9, 1173–1189, https://doi.org/10.5194/acp-9-1173-2009, 2009.

Schepanski, K., Mallet, M., Heinold, B., and Ulrich, M.: North African dust transport toward the western Mediterranean basin: atmospheric controls on dust source activation and transport pathways during June–July 2013, Atmospheric Chemistry and Physics, 16, 14 147–14 168, https://doi.org/10.5194/acp-16-14147-2016, 2016.

Schepanski, K., Heinold, B., and Tegen, I.: Harmattan, Saharan heat low, and West African monsoon circulation: modulations on the Saharan dust outflow towards the North Atlantic, Atmospheric Chemistry and Physics, 17, 10 223–10 243, https://doi.org/10.5194/acp-17-10223-2017, 2017.

Scheuvens, D., Schütz, L., Kandler, K., Ebert, M., and Weinbruch, S.: Bulk composition of northern African dust and its source sediments — A compilation, Earth-Science Reviews, 116, 170–194, https://doi.org/10.1016/j.earscirev.2012.08.005, 2013.

Seinfeld, J. H. and Pandis, S. N.: Atmospheric Chemistry and Physics: From Air Pollution to Climate Change, 3rd Edition \textbar Wiley, John Wiley & Sons, Hoboken, 3 edn., https://www.wiley.com/en-us/Atmospheric+Chemistry+and+Physics%3A+From+Air+Pollution+to+Climate+Change%2C+3rd+Edition-p-9781118947401, 2016.

Shao, Y., Wyrwoll, K.-H., Chappell, A., Huang, J., Lin, Z., McTainsh, G. H., Mikami, M., Tanaka, T. Y., Wang, X., and Yoon, S.: Dust cycle: An emerging core theme in Earth system science, Aeolian Research, 2, 181–204, https://doi.org/10.1016/j.aeolia.2011.02.001, 2011.

Sokolik, I. N. and Toon, O. B.: Incorporation of mineralogical composition into models of the radiative properties of mineral aerosol from UV to IR wavelengths, Journal of Geophysical Research: Atmospheres, 104, 9423–9444, https://doi.org/10.1029/1998JD200048, 1999.

Song, Q., Ginoux, P., Gonçalves Ageitos, M., Miller, R. L., Obiso, V., and Pérez García-Pando, C.: Modeling impacts of dust mineralogy on fast climate response, Atmospheric Chemistry and Physics, 24, 7421–7446, https://doi.org/10.5194/acp-24-7421-2024, 2024.

Souza, E. J. D. S., Fomba, K. W., Anaya, S. G. M., Schepanski, K., Freire, S. M., Materić, D., Reemtsma, T., and Herrmann, H.: Particle-bound mercury in Saharan dust-loaded particulate matter in Cabo Verde, Journal of Hazardous Materials, 487, 137 053, https://doi.org/10.1016/j.jhazmat.2024.137053, 2025.

Stein, A. F., Draxler, R. R., Rolph, G. D., Stunder, B. J. B., Cohen, M. D., and Ngan, F.: NOAA's HYSPLIT Atmospheric Transport and Dispersion Modeling System, Bulletin of the American Meteorological Society, 96, 2059–2077, https://doi.org/10.1175/BAMS-D-14-00110.1, 2015.

Stocker, T. F., Qin, D., Plattner, G.-K., Tignor, M., Allen, S. K., Boschung, J., Nauels, A., Xia, Y., Bex, V., and Midgley, P. M.: Climate Change 2013: The Physical Science Basis, Tech. rep., Intergovernmental Panel on Climate Change, Working Group I Contribution to the IPCC Fifth Assessment Report (AR5)(Cambridge University Press, Cambridge, United Kingdom and New York, NY, USA.), 1535 pp., 2013.

Tegen, I., Harrison, S. P., Kohfeld, K., Prentice, I. C., Coe, M., and Heimann, M.: Impact of vegetation and preferential source areas on global dust aerosol: Results from a model study, Journal of Geophysical Research: Atmospheres, 107, AAC 14–1–AAC 14–27, https://doi.org/10.1029/2001JD000963, 2002.

Tegen, I., Schepanski, K., and Heinold, B.: Comparing two years of Saharan dust source activation obtained by regional modelling and satellite observations, Atmospheric Chemistry and Physics, 13, 2381–2390, https://doi.org/10.5194/acp-13-2381-2013, 2013.

Tesche, M., Gross, S., Ansmann, A., Müller, D., Althausen, D., Freudenthaler, V., and Esselborn, M.: Profiling of Saharan dust and biomass-burning smoke with multiwavelength polarization Raman lidar at Cape Verde, Tellus B: Chemical and Physical Meteorology, 63, 649–676, https://doi.org/10.1111/j.1600-0889.2011.00548.x, 2011.

Wolke, R. and Knoth, O.: Implicit–explicit Runge–Kutta methods applied to atmospheric chemistry-transport modelling, Environmental Modelling & Software, 15, 711–719, https://doi.org/10.1016/S1364-8152(00)00034-7, 2000.

Wolke, R., Schröder, W., Schrödner, R., and Renner, E.: Influence of grid resolution and meteorological forcing on simulated European air quality: A sensitivity study with the modeling system COSMO–MUSCAT, Atmospheric Environment, 53, 110–130, https://doi.org/10.1016/j.atmosenv.2012.02.085, 2012.

Zhang, L., Gong, S., Padro, J., and Barrie, L.: A size-segregated particle dry deposition scheme for an atmospheric aerosol module, Atmospheric Environment, 35, 549–560, https://doi.org/10.1016/S1352-2310(00)00326-5, 2001.

Zhang, X. L., Wu, G. J., Zhang, C. L., Xu, T. L., and Zhou, Q. Q.: What is the real role of iron oxides in the optical properties of dust aerosols?, Atmospheric Chemistry and Physics, 15, 12 159–12 177, https://doi.org/10.5194/acp-15-12159-2015, 2015.

Zhang, Y., Saito, M., Yang, P., Schuster, G., and Trepte, C.: Sensitivities of Spectral Optical Properties of Dust Aerosols to Their Mineralogical and Microphysical Properties, Journal of Geophysical Research: Atmospheres, 129, e2023JD040 181, https://doi.org/10.1029/2023JD040181, 2024.